

AD-A155 139

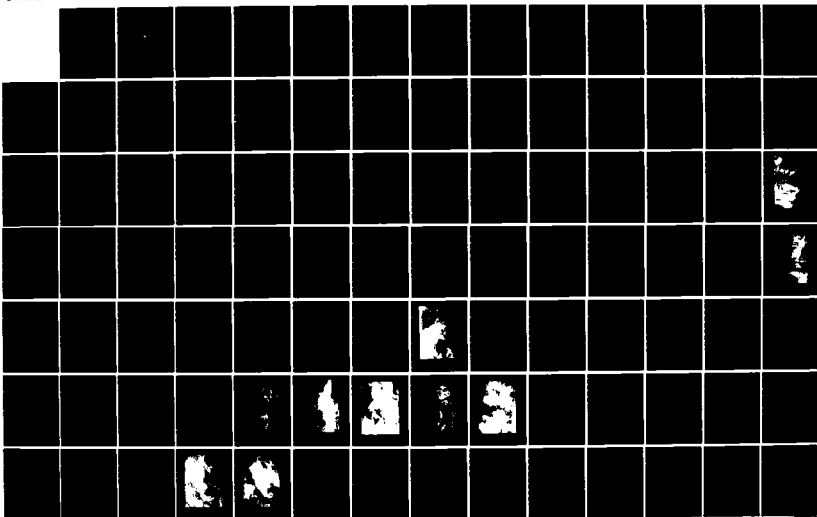
MESOSCALE FEATURES AND ATMOSPHERIC REFRACTION
CONDITIONS OF THE ARCTIC MARGINAL ICE ZONE(U) NAVAL
POSTGRADUATE SCHOOL MONTEREY CA J A MCNITT DEC 84

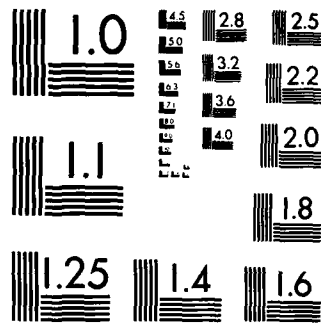
1/2

UNCLASSIFIED

F/G 4/1

NL





MICROCOPY RESOLUTION TEST CHART
NATIONAL BUREAU OF STANDARDS-1963-A

2
M

AD-A155 139

NAVAL POSTGRADUATE SCHOOL

Monterey, California



DTIC
ELECTE
JUN 18 1985
S B

THESIS

MESOSCALE FEATURES AND ATMOSPHERIC
REFRACTION CONDITIONS OF THE
ARCTIC MARGINAL ICE ZONE

by

James A. McNitt

December 1984

Thesis Advisor:

Kenneth L. Davidson

Approved for public release; distribution unlimited

DTIC FILE COPY

85 5 22 019

UNCLASSIFIED

SECURITY CLASSIFICATION OF THIS PAGE (When Data Entered)

REPORT DOCUMENTATION PAGE		READ INSTRUCTIONS BEFORE COMPLETING FORM
1. REPORT NUMBER	2. GOVT ACCESSION NO. AD-A155139	3. RECIPIENT'S CATALOG NUMBER
4. TITLE (and Subtitle) Mesoscale Features and Atmospheric Refraction Conditions of the Arctic Marginal Ice Zone		5. TYPE OF REPORT & PERIOD COVERED Master's Thesis December 1984
		6. PERFORMING ORG. REPORT NUMBER
7. AUTHOR(s) James A. McNitt		8. CONTRACT OR GRANT NUMBER(s)
9. PERFORMING ORGANIZATION NAME AND ADDRESS Naval Postgraduate School Monterey, California 93943		10. PROGRAM ELEMENT, PROJECT, TASK AREA & WORK UNIT NUMBERS
11. CONTROLLING OFFICE NAME AND ADDRESS Naval Postgraduate School Monterey, California 93943		12. REPORT DATE December 1984
		13. NUMBER OF PAGES 128
14. MONITORING AGENCY NAME & ADDRESS (if different from Controlling Office)		15. SECURITY CLASS. (of this report) Unclassified
		15a. DECLASSIFICATION/DOWNGRADING SCHEDULE
16. DISTRIBUTION STATEMENT (of this Report) Approved for public release; distribution unlimited		
17. DISTRIBUTION STATEMENT (of the abstract entered in Block 20, if different from Report)		
18. SUPPLEMENTARY NOTES		
19. KEY WORDS (Continue on reverse side if necessary and identify by block number) Atmospheric Refraction Conditions Arctic Marginal Ice Zone Fram Strait, East Greenland Sea		
20. ABSTRACT (Continue on reverse side if necessary and identify by block number) The Marginal Ice Zone Experiment (MIZEX-83) conducted in the Arctic during the summer of 1983 is summarized and the mesoscale features and atmospheric refraction conditions described. The three case studies examined are: warm air advection over dense pack ice causing strong elevated ducting and subrefraction, cold air advection over relatively open water causing shallow convection and normal refraction conditions, large scale		

DD FORM 1473
1 JAN 73EDITION OF 1 NOV 65 IS OBSOLETE
S/N 0102-LF-014-6601

1

UNCLASSIFIED

SECURITY CLASSIFICATION OF THIS PAGE (When Data Entered)

#20 - ABSTRACT - (CONTINUED)

subsidence in the western quadrants of an anticyclone leading to super-refraction and weak ducting.

Developing synoptic scale cyclones adjacent to the MIZEX-83 area often determined the airflow over the region. The observed large horizontal SST gradients were the dominant forcing mechanisms on surface layer stability. Trapping layers associated with subsidence inversions can be located on satellite imagery by assuming that stratiform clouds form immediately below the inversion. Uniform cloud and refraction layers were not common during MIZEX-83 due to strong mesoscale variability. Factors affecting inversion height include subsidence and entrainment mixing. Bulk Richardson number values for locations over the open water and pack ice show significant variability in stability conditions across the MIZ.

Accession For	
NOIS SPA&I	<input checked="" type="checkbox"/>
NOIS CAP	<input type="checkbox"/>
Unannounced	<input type="checkbox"/>
Justification	
By	
Distribution/	
Availability Codes	
Dist	Avail and/or Special
A-1	

Approved for public release; distribution unlimited.

Mesoscale Features and Atmospheric Refraction
Conditions of the
Arctic Marginal Ice Zone

by

James A. McNitt
Lieutenant, United States Navy
B.S., University of Idaho, 1978

Submitted in partial fulfillment of the
requirements for the degree of

MASTER OF SCIENCE IN METEOROLOGY AND OCEANOGRAPHY

from the
NAVAL POSTGRADUATE SCHOOL
December 1984

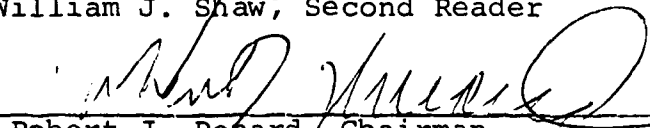
Author:

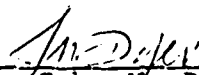

James A. McNitt

Approved by:


Kenneth L. Davidson, Thesis Advisor


William J. Shaw, Second Reader


Robert J. Renard, Chairman,
Department of Meteorology


John N. Dyer
Dean of Science and Engineering

ABSTRACT

The Marginal Ice Zone Experiment (MIZEX-83) conducted in the Arctic during the summer of 1983 is summarized and the mesoscale features and atmospheric refraction conditions described. The three case studies examined are: warm air advection over dense pack ice causing strong elevated ducting and subrefraction; cold air advection over relatively open water causing shallow convection and normal refraction conditions; large scale subsidence in the western quadrants of an anticyclone leading to super-refraction and weak ducting.

Developing synoptic scale cyclones adjacent to the MIZEX-83 area often determined the airflow over the region. The observed large horizontal SST gradients were the dominant forcing mechanisms on surface layer stability. Trapping layers associated with subsidence inversions can be located on satellite imagery by assuming that stratiform clouds form immediately below the inversion. Uniform cloud and refraction layers were not common during MIZEX-83 due to strong mesoscale variability. Factors affecting inversion height include subsidence and entrainment mixing. Bulk Richardson number values for locations over the open water and pack ice show significant variability in stability conditions across the MIZ.

TABLE OF CONTENTS

I.	INTRODUCTION -----	14
	A. GENERAL DESCRIPTION OF MIZEX -----	14
	B. PURPOSE OF THESIS -----	15
	C. ATMOSPHERIC REFRACTION CONCEPTS -----	16
	D. MIZEX-83 DATA ACQUISITION -----	18
	1. Observation and Measurements -----	18
	2. Radiosondes -----	20
	3. Aircraft Measurements -----	21
	4. Ice Edge Characteristics -----	21
	5. Remote Sensing -----	22
II.	METEOROLOGY IN THE MARGINAL ICE ZONE -----	23
	A. GENERAL -----	23
	B. SYNOPTIC CLIMATOLOGY -----	23
	C. SURFACE WINDS -----	24
	D. AIR AND OCEAN TEMPERATURES -----	25
	E. VISIBILITY--CLOUDS--PRECIPITATION -----	26
	F. BOUNDARY LAYER CLIMATE -----	27
	G. HEAT BUDGET CLIMATOLOGIES -----	29
III.	CASE STUDIES -----	31
	A. GENERAL -----	31
	B. CASE STUDIES -----	33
	1. Case 1: 1-4 July 1983 -----	33
	a. Synoptic and Mesoscale Features -----	33
	b. Refraction Conditions -----	34

2.	Case 2: 14-17 July 1983 -----	54
	a. Synoptic and Mesoscale Features -----	54
	b. Refraction Conditions -----	56
3.	Case 3: 27-29 July 1983 -----	77
	a. Synoptic and Mesoscale Features -----	77
	b. Refraction Conditions -----	78
IV.	SUMMARIES OF CONDITIONS -----	101
	A. SUMMARY OF SYNOPTIC FEATURES -----	101
	B. SUMMARY OF MESOSCALE FEATURES -----	102
	1. Baroclinity and Stability -----	102
	C. OCCURRENCE OF ELEVATED DUCTING -----	105
	1. Factors Affecting the Inversion	
	Base Height -----	105
	a. Subsidence and Entrainment -----	105
	b. Role of Atmospheric Boundary	
	Layer Mixing (Turbulence) -----	106
	D. MOISTURE CONTENT -----	114
	E. RADIOSONE HUMIDITY SENSOR WETTING -----	117
V.	CONCLUSIONS AND RECOMMENDATIONS -----	120
	LIST OF REFERENCES -----	124
	INITIAL DISTRIBUTION LIST -----	126

LIST OF TABLES

I.	IREPS Classification of Refraction Conditions ---	19
II.	Estimates of the Terms in the Surface Heat Budget (after Vowinckel and Orvig, 1970) -----	30

LIST OF FIGURES

1.	R/V POLARBJORN's Radisonde Launch Positions for Three Case Studies: 1-4 July 1983, 14-17 July 1983, 27-29 July 1983 -----	37
2.	(a) R/V POLARBJORN's Radiosonde Launch Positions During 1-4 July 1983. (b) Ice Morphology on 1 July 1983 Relative to POLARBJORN North of Spitsbergen at about 81°N 7°E -----	38
3.	Visual DMSP Picture for 4 July 1983, 0621 GMT -----	39
4.	Wind Velocity Vectors and Duct Thicknesses for 1-4 July, 14-17 July, 26-29 July MIZEX-83 -----	40
5.	Ice Coverage, 5 m Air Temperature and Sea-surface Temperature for 1-4 July 1983 -----	41
6.	(a) IREPS Output for 1 July 1983, 0023 GMT. (b) IREPS Output for 1 July 1983, 0023 GMT with Bogus Relative Humidity Value of 40% Inserted at 500 m -----	42
7.	(a) Q and θ Plot for Radiosonde Sounding 1 July 1983, 0023 GMT. (b) IREPS Output for 1 July 1983, 0023 GMT -----	43
8.	(a) Q and θ Plot for Radiosonde Sounding 1 July 1983, 0943 GMT. (b) IREPS Output for 1 July 1983, 0943 GMT -----	44
9.	(a) Q and θ Plot for Radiosonde Sounding 1 July 1983, 2332 GMT. (b) IREPS Output for 1 July 1983, 2332 GMT -----	45
10.	(a) Q and θ Plot for Radiosonde Sounding 2 July 1983, 1131 GMT. (b) IREPS Output for 2 July 1983, 1131 GMT -----	46
11.	(a) Q and θ Plot for Radiosonde Sounding 2 July 1983, 2333 GMT. (b) IREPS Output for 2 July 1983, 2333 GMT -----	47
12.	(a) Q and θ Plot for Radiosonde Sounding 3 July 1983, 1134 GMT. (b) IREPS Output for 3 July 1983, 1134 GMT -----	48

13.	(a) Q and θ Plot for Radiosonde Sounding 3 July 1983, 2330 GMT. (b) IREPS Output for 3 July 1983, 2330 GMT -----	49
14.	(a) Q and θ Plot for Radiosonde Sounding 4 July 1983, 0805 GMT. (b) IREPS Output for 4 July 1983, 0805 GMT -----	50
15.	(a) Q and θ Plot for Radiosonde Sounding 4 July 1983, 1522 GMT. (b) IREPS Output for 4 July 1983, 1552 GMT -----	51
16.	(a) Q and θ Plot for Radiosonde Sounding for 4 July 1983, 2333 GMT. (b) IREPS Output for 4 July 1983, 2333 GMT -----	52
17.	Visual DMSP Picture for 2 July 1983, 1943 GMT -----	53
18.	(a) Radiosonde (o) and Spiral Sounding (·) Start Positions During 14-17 July MIZEX-83. (b) Ice Morphology on 14 July 1983 Relative to POLARBJORN's Position -----	58
19.	Ice Coverage, 5 m Air Temperature and Sea Surface Temperature for 14-17 July 1983 -----	59
20.	Surface Analyses for 16 July 1983, 1500 GMT -----	60
21.	Visual DMSP Picture at 14 July 1983, 0432 GMT -----	61
22.	(a) Q and θ Plot for Radiosonde Sounding 14 July 1983, 2022 GMT. (b) T and T_d Plot for Radiosonde Sounding 14 July 1983, 2022 GMT -----	62
23.	(a) Q and θ Plot for Spiral Sounding 15 July 1983, 1809 GMT. (b) Q and θ Plot for Spiral Sounding, 15 July 1983, 2004 GMT -----	63
24.	(a) Q and θ Plot for Spiral Sounding 15 July 1983, 1134 GMT. (b) IREPS Output for 15 July 1983, 1134 GMT -----	64
25.	(a) Q and θ Plot for Spiral Sounding 15 July 1983, 2105 GMT. (b) IREPS Output for 15 July 1983, 2105 GMT -----	65
26.	Plot for Radiosonde Sounding 15 July 1983, 2335 GMT. Humidity Sensor Failed at Launch -----	66
27.	(a) Q and θ Plot for Radiosonde Sounding 16 July 1983, 1147 GMT. (b) IREPS Output for 16 July 1983, 1147 GMT -----	67

28.	(a) Q and θ Plot for Radiosonde Sounding 16 July 1983, 1734 GMT with Wind Barbs in Knots. (b) IREPS Output for 16 July 1983, 1734 GMT -----	68
29.	(a) Q and θ Plot for Radiosonde Soundings for 17 July 1983, 1415 GMT with Wind Barbs in Knots. (b) IREPS Output for 17 July 1983, 1415 GMT -----	69
30.	(a) Q and θ Plot for Radiosonde Sounding 17 July 1983, 2331 GMT. (b) IREPS Output for 17 July 1983, 2331 GMT -----	70
31.	T and T_d Plot for 17 July 1983, 2331 GMT -----	71
32.	Visual DMSP Picture at 15 July 1983, 2014 GMT -----	72
33.	Visual DMSP Picture at 16 July 1983, 1953 GMT -----	73
34.	Infrared DMSP Picture at 16 July 1983, 1953 GMT ---	74
35.	Visual DMSP Picture at 17 July 1983, 1932 GMT -----	75
36.	Infrared DMSP Picture at 17 July 1983, 1932 GMT ---	76
37.	Radiosonde (o) and Spiral (·) Sounding Start Positions During 27-29 July 1983 -----	81
38.	Ice Coverage, 5 m Air Temperature and Sea Surface Temperature for 27-29 July 1983 -----	82
39.	Surface Pressure Analysis for 26 July 1983, 0300 GMT -----	83
40.	Surface Pressure Analysis for 27 July 1983, 0300 GMT -----	84
41.	(a) Visual and DMSP Picture at 29 July 1983, 0420 GMT. (b) Infrared DMSP Picture at 29 July 1983, 0420 GMT -----	85
42.	(a) Q and θ Plot for Spiral Sounding 27 July 1983, 1148 GMT. (b) IREPS Output for 27 July 1983, 1148 GMT -----	87
43.	(a) Q and θ Plot for Radiosonde Soundings Made 27 July 1983, 1404 GMT. (b) IREPS Output for 27 July 1983, 1404 GMT -----	88
44.	(a) Q and θ Plot for Radiosonde Sounding 27 July 1983, 1416 GMT. (b) IREPS Output for 27 July 1983, 1416 GMT -----	89

45.	(a) Q and θ Plot for Radiosonde Sounding 27 July 1983, 1538 GMT. (b) IREPS Output for 27 July 1983, 1538 GMT -----	90
46.	(a) Q and θ Plot for Spiral Sounding 28 July 1983, 1331 GMT. (b) IREPS Output for 28 July 1983, 1331 GMT -----	91
47.	(a) Q and θ Plot for Spiral Sounding 28 July 1983, 1456 GMT. (b) IREPS Output for 28 July 1983, 1456 GMT -----	92
48.	(a) Q and θ Plots for Spiral Sounding 28 July 1983, 1550 GMT. (b) IREPS Output for 28 July 1983, 1550 GMT -----	93
49.	(a) Q and θ Plots for 28 July 1983, 1621 GMT. (b) IREPS Output for 28 July 1983, 1621 GMT -----	94
50.	(a) Q and θ Plot for Spiral Sounding 28 July 1983, 1647 GMT. (b) IREPS Output for 29 July, 1647 GMT -----	95
51.	(a) Q and θ Plot for Spiral Sounding 28 July 1983, 1737 GMT. (b) IREPS Output for 29 July 1983, 1737 GMT -----	96
52.	(a) Q and θ Plot for Spiral Sounding 29 July 1983, 1157 GMT. (b) IREPS Output for 29 July 1983, 1157 GMT -----	97
53.	(a) Q and θ Plot for Spiral Sounding 29 July 1983, 1244 GMT. (b) IREPS Output for 29 July 1983, 1244 GMT -----	98
54.	(a) Q and θ Plot for Spiral Sounding 29 July 1983, 1309 GMT. (b) IREPS Output for 29 July 1983, 1309 GMT -----	99
55.	(a) Q and θ Plot for Radiosonde Soundings Made 29 July 1983, 1329 GMT. (b) IREPS Output for 29 July 1983, 1329 GMT -----	100
56	Surface Analysis for 26 July 1983, 1500 GMT -----	103
57	(a) Q and θ Plot for Radiosonde Sounding 25 July 1983, 2332 GMT. (b) IREPS Output for 25 July 1983, 2332 GMT -----	111
58.	(a) Q and θ Plot for Radiosonde Sounding 26 July 1983, 1937 GMT. (b) IREPS Output for 26 July 1983, 1937 GMT -----	112

Because of the significant atmospheric horizontal temperature gradient across the ice edge, mesoscale features such as fronts or cellular circulations similar to land breezes may exist (Tucker, 1984). Due to the relatively warm air over the open water region of the MIZ, a downward-sloping pressure gradient from the sea to the ice may develop so that air above the atmospheric boundary layer would accelerate towards the ice. The resulting flow aloft causes a pressure increase over the ice and a pressure decrease over the ocean at the surface so that a semi-permanent off-ice surface flow is generated.

D. AIR AND OCEAN TEMPERATURE

The relatively warm North Atlantic Ocean Current flows northward off Norway. In July and August it has a temperature of approximately 5°C. The warm saline Atlantic Ocean water flows north in the West Spitsbergen Current and enters the Arctic Ocean as a subsurface current north of Spitsbergen. Along the Greenland coast the cold, less saline East Greenland Current transports ice, polar water and recirculated Atlantic Ocean water equatorward (Johannessen et al., 1983). Water with surface temperatures below 0°C may extend more than 12 km away from the ice edge with air temperatures rarely falling below such values (Wadhams and Squire, 1983).

Air temperatures correlate with the SST extrema for the same time period. Climatology indicates that air temperature differences across the MIZ may be as great as 5°C. Observations

ship reports available. Permanent observation stations are located on Spitsbergen and Greenland which have significant topographic features. The Greenland ice cap forms an extensive plateau, 2,000 m to 3,000 m in elevation, and Spitsbergen has terrain extending up to 1400 m. Observed surface winds at the Greenland coast reflect a strong katabatic flow. Based on observations made at the West coast of Greenland, Mahrt and Larsen (1984) showed that oscillations associated with trapped internal waves could control nocturnal air motion over a sloping valley floor. Clearly, coastal surface wind climatology may not reflect the surface wind field of the MIZ.

The MIZEX-83 areas was to the north of the primary synoptic scale depression tracks. Depressions reaching the region are likely to be occluded, relatively small in extent and associated with little bad weather (Vowinckel and Orvig, 1970). The mean air pressure distribution for July as shown by Vowinckel and Orvig (1970) and Prik (1959), indicate that southerly or southwesterly winds are most likely.

C. SURFACE WINDS

Shipboard observed surface winds described in the Brown et al. (1984) summary were obtained from the U.K. Meteorological Office. The observations span the period from May 1871 to October 1979 with more than two-thirds of the record covering the period from 1966 to 1979. In June and July the wind direction should be variable in the eastern MIZ and from the south to southwest or northwest in the western MIZ. Wind speeds should be from 2 m/s to 8 m/s.

II. METEOROLOGY IN THE MARGINAL ICE ZONE

A. GENERAL

Although oceanographic research has been underway in the East Greenland Sea marginal ice zone for several years the first comprehensive atmospheric study of the region was conducted during MIZEX-83. Previous Arctic meteorological studies such as the Arctic Ice Dynamics Joint Experiment (Pritchard, 1980) have provided information regarding the growth, motion and decay of sea ice in the interior of the Arctic Ocean. However, the area of greatest thermodynamical importance is the region north and west of Spitsbergen, where the Arctic Ocean interacts with the warmer southern waters.

The existing MIZ climatology is extremely qualitative and indicates the need for continued research in the region. A climatological summary was compiled by Brown et al. (1984, unpublished manuscript) in which the following aspects of the MIZ were discussed: synoptic climatology, surface winds, air and ocean temperatures, visibility-clouds-precipitation, boundary layer climatology and heat budget climatologies. Most of this chapter is based on the Brown et al. (1984) summary.

B. SYNOPTIC CLIMATOLOGY

Synoptic climatology of the MIZ is poorly understood because of the minimal number of atmospheric soundings and

5. Remote Sensing

The Defense Meteorological Satellite Program (DMSP) satellite F6 was in a near polar orbit during MIZEX-83. Both the visual and infrared DMSP imagery were obtained from the National Snow and Ice Data Center, Boulder, Colorado. The resolution of the visual imagery and of most of the infrared imagery is 2.7 km. The infrared mosaics have a resolution of 5.4 km.

The vertical soundings were plotted on pseudo-adiabatic diagrams as temperature and dew-point temperature by personnel at the Polar Science Center of the University of Washington.

3. Aircraft Measurements

A Beechcraft Baron atmospheric research aircraft operated by ARA was instrumented to measure the wind, temperature, humidity and turbulence. Eleven flights were made with each flight producing about six spiral soundings. The air temperature was measured by a standard Rosemount 50-ohm resistance wire sensor. The dew-point temperature was measured by the Cambridge dew-point system utilizing a chilled mirror. Navigation was primarily by Omega and NDB (non-directional beacon).

The vertical profiles consist of 15 s averaged values of parameters, including position, time, pressure, altitude, air temperature, dew-point temperature and virtual potential temperature. Virtual potential temperature (solid line) and specific humidity (dashed line) plots were constructed.

4. Ice Edge Characteristics

The movement of ice floes in the MIZ was monitored using Motorola radar transponders and radar reflectors which were tracked by POLARBJORN during the drift phase. The Scott Polar Research Institute data summary includes useful descriptions and photographs of ice conditions in the MIZ.

primary source for surface observations has been the Preliminary Field Meteorological Data Report compiled by the investigators aboard POLARBJORN and by Airborne Research Associates (ARA). Included in the report are POLARBJORN's bridge weather observations, including sea-surface temperature (SST) and air temperature. Weather observations were made every three hours in accordance with standard World Meteorological Organization (WMO) procedures.

The SST was measured at a seawater intake inside the ship. A correction factor of -2.0°C was applied to the intake temperature to provide better correlation with the temperature measured with a boom mounted thermistor. The surface air temperature was measured by a resistance thermistor mounted at 5 m above sea level. Radiation measurements were made aboard POLARBJORN from 21 June through 28 July 1983. The upward looking array of radiometers measured shortwave irradiance, longwave irradiance, and total incoming irradiance.

2. Radiosondes

Radisonde observations aboard POLARBJORN were made with the Vaisala Micro-Cora Upper Air Sounding System using the RS-80 radiosonde. Wind direction and speed were determined by tracking the balloon within the Omega navigational network and averaging balloon motion over a period of two to four minutes. Ascent rates were 120-150 m/min (the WMO standard is 300 m/min) with pressure, temperature and relative humidity reported every 10 s.

TABLE I

IREPS Classification of Refraction Conditions

IREPS CLASSIFICATION	$\frac{dN}{dz} [\text{km}^{-1}]$	$\frac{dM}{dz} [\text{km}^{-1}]$	RANGE
SUBREFRACTION	>0	>157	REDUCED
NORMAL	0 to -79	79 to 157	NORMAL
SUPER-REFRACTION	-79 to -157	0 to 79	INCREASED
TRAPPING	<-157	<0	GREATLY INCREASED

variability can be considered an order of magnitude less than that of the temperature and humidity gradients.

Refractivity classifications used in IREPS, developed by the Naval Ocean Systems Command, are listed in Table I. Normal refraction conditions are represented by N decreasing with height at a rate of 0 to -79 N units per kilometer. Where $M = N + 0.157h$, for altitude (h) in meters, super-refraction conditions are represented by M increasing with height at a rate of 0 to 79 M units per kilometer. Trapping conditions are best represented by the M profile where $dM/dZ < 0$. When analyzing IREPS results it is important to characterize trapping as either weak or strong because a weak trapping layer could easily be a super-refractive layer.

A trapping layer is the region where ray radius will be equal to or less than the earth's radius. A duct is the region associated with a trapping layer and is the layer in which the EM energy is partially confined and channeled between the top and bottom of the duct. The duct may be elevated or surface based. The duct thickness determines which frequencies will be affected. A low frequency signal will be more easily trapped in a deep duct than a shallow one. Both the transmitter and receiver must be located in the duct for trapping to occur.

D. MIZEX-83 DATA ACQUISITION

1. Observations and Measurements

During MIZEX-83 a variety of meteorological data were collected from ship, aircraft, balloon and satellite. A

$$n = 1.0003$$

Refraction of incident rays (which are perpendicular to the phase fronts of radiated energy) across a discontinuity of n is described by Snell's Law (Kerr, 1951). When refracted, the EM wave front tilts towards the higher n value which corresponds to the more dense medium. A convenient refraction parameter is the atmospheric refractivity (Kerr, 1951):

$N = (n-1) \times 10^6$ given by the relation:

$$N = (77.6P)/T + (3.73 \times 10^5 e)/T^2$$

where:

P is atmospheric pressure in millibars,

T is temperature in Kelvins, and

e is water vapor pressure in millibars.

Refraction conditions are defined on the basis of the refractivity gradient dN/dz . Considering the relevant atmospheric parameters, the vertical gradient of refractivity is expressed as:

$$\frac{dN}{dz} = \frac{\partial N}{\partial P} \frac{dP}{dz} + \frac{\partial N}{\partial T} \frac{dT}{dz} + \frac{\partial N}{\partial e} \frac{de}{dz}$$

Near the surface the first term on the right hand side is essentially a constant. The partial derivatives in the second and third terms are calculated for each level but their

to make a qualitative judgment of the occurrence of anomalous propagation in the MIZ.

The association of elevated ducting with stratus clouds is examined. The physical processes involved in determining the height of the inversion base are discussed. The role of atmospheric boundary layer stability, as determined by horizontal advection and sea-surface temperature (SST), is also discussed.

Finally, some conclusions are made regarding the parameters which must be defined in order to effectively model the atmospheric refraction conditions in the MIZ. Several recommendations are made which suggest a need for continued research in this area.

C. ATMOSPHERIC REFRACTION CONCEPTS

The following discussion is limited to the refraction of electromagnetic radiation within the wavelength range of 1 cm to 10 m. This includes microwave, ultra high frequency (UHF) and very high frequency (VHF). Electromagnetic (EM) signals are transmitted through matter by the absorption and emission of EM energy by the atomic and molecular constituents of the medium. The interaction of the EM wave with the medium is described by the dielectric constant, ϵ , which is dependent upon the characteristics of the medium and upon the frequency. By definition the index of refraction, $n = \sqrt{\epsilon} = c/v$. A representative value of the index of refraction for air is:

of information. Another goal was to establish and test cooperative measurement procedures. The MIZEX-83 area was north and west of Spitsbergen. Atmospheric data were collected from radiosondes launched from the research vessel POLARBJORN. Additional meteorological data were collected from the research vessel POLARSTERN, a twin engine Beechcraft BARON aircraft, and a U.S. Navy RP-3A research aircraft.

B. PURPOSE OF THESIS

This thesis addresses the synoptic and mesoscale variability observed during MIZEX-83 with emphasis on the atmospheric refraction conditions of the region during the observation period. The availability of satellite data helps to alleviate the problems caused by data scarcity in the high latitude region. Imagery from the Defense Meteorological Satellite Program (DMSP) are utilized to infer synoptic features, direction of the representative airflow and horizontal extent of stratiform clouds.

The vertical temperature and moisture profiles obtained from radiosondes and aircraft measurements are used to describe the mesoscale temporal and spatial variability of the troposphere below 700 mb. Pressure, temperature and humidity data are the input parameters for the Integrated Refractive Effects Prediction System (IREPS). The atmospheric refraction and propagation conditions are predicted by IREPS. The relative strength of trapping and subrefractive layers and the characteristics of the sounding profiles are examined

I. INTRODUCTION

A. GENERAL DESCRIPTION OF MIZEX

Modern naval weapon and communications systems are dependent upon the environment in which they operate. Regional changes in atmospheric properties such as moisture and temperature have a significant effect on many electro-magnetic and electro-optical systems. The Arctic marginal ice zone (MIZ) is a region of strong mesoscale oceanic and atmospheric variability. The MIZ is described as the region in which the polar air, ice and water masses interact with the temperate ocean and climate systems (Wadhams and Squire, 1981).

Scientific interest in the region is due to the strong horizontal and vertical gradients in the atmosphere and the ocean which affect the heat, salt and momentum fluxes in the MIZ. These physical properties are important to the Navy because they can dramatically enhance or degrade weapon systems performances. The horizontal and vertical gradients of atmospheric and oceanic properties are being investigated during the Marginal Ice Zone Experiment (MIZEX).

A pilot field program (MIZEX-83) was conducted during June and July of 1983. One goal of the six-week experiment was to ensure that the temporal and spatial scales selected for the experimental arrays could yield the maximum amount

ACKNOWLEDGMENTS

I wish to extend my sincere appreciation to my thesis advisor, Professor K.L. Davidson. His support, both as an advisor and friend has made this research a more meaningful experience. Special thanks must go to all the members of the Environmental Physics Group, Mike McDermot, Professor C.H. Wash, and the Educational Media Department. I am grateful to Ron Lindsey of the Polar Science Center, University of Washington, for providing the shipboard radiosonde data. The aircraft data were provided by Dr. C.W. Fairall of Penn State and Dr. Ralph Markson of Airborne Research Associates. A highlight of my research has been the time spent with Jay Rosenthal and Roger Helvey of the Pacific Missile Test Center Geophysics Branch. Additionally, I wish to thank my father for his encouragement and leadership. Finally, my sincere thanks is offered to our many friends on the Peninsula who have been interested in my welfare and have impressed me with their hospitality.

59.	Downward Shortwave Radiation Measured from R/V POLARBJORN During MIZEX-83 -----	115
60.	Downward Longwave Radiation Measured from R/V POLARBJORN During MIZEX-83 -----	116
61.	(a) T and T_d Plot from Radiosonde Sounding 1 July 1983, 0023 GMT. (b) T and T_d Plot from Radio- sonde Sounding 3 July 1983, 2330 GMT -----	119

for an area 0° to 10°W during June through August indicates that surface layer stability is determined by the horizontal advection of the mean airflow.

E. VISIBILITY--CLOUDS--PRECIPITATION

According to the Arctic Pilot (1975) fog is so common in the MIZ that "a belt of fog on the horizon may indicate the ice edge." Shipboard observations for the MIZ from 0°-10°W show that visibility less than 2 km was reported for 65% of June and 35% of July. According to Vowinckel and Orvig (1970) mean cloud amounts over the MIZ are likely to be from 70% to 90%. Due to upper level warm air advection, medium level clouds such as altocumulus and altostratus are as likely as lower-level stratus and stratocumulus.

The observation of a laminated structure in the Arctic stratus, with a clear air layer separating cloud layers, has been associated with the interaction of the cloud field and radiation (Herman and Goody, 1976). The physical characteristics of Arctic stratus clouds were further investigated by Tsay and Jayaweera (1984) using data acquired by aircraft measurements over the Beaufort Sea during June 1980. They concluded that arctic stratus clouds fall into two categories determined by the airflow in which they form. When cold polar air flows over a warmer sea-ice surface the stratus clouds tend to form by a convective-type process and are characterized by an elevated base and a low liquid water content. When warm, moist maritime air flows over the colder Arctic Ocean

the stratus clouds form very near the sea-ice surface and more than one cloud layer may form depending on the availability of moisture aloft.

Precipitation amounts are characteristically low in the MIZ; Spitsbergen and northeast coastal Greenland have mean annual precipitation amounts of 20 to 30 cm. Mid-May to mid-July is probably the driest period according to the Arctic Pilot (1975).

F. BOUNDARY LAYER CLIMATE

The atmospheric boundary layer (ABL) of the MIZ is structured by air from one of three sources: air from the polar ice cap, maritime air which has traversed a long open ocean fetch, or air from the Greenland landmass. The first case was examined by Belmont (1958) using two years of data from ice island T-3. He found that for a mixed layer capped by an elevated inversion the mean inversion base height was about 450 m in June and 590 m in July.

The height of the ABL in high latitudes can be estimated from a formulation by Brown (1981). His model depends on a surface scaling velocity determined by the surface stress, the Coriolis parameter and a stratification parameter which depends on the air-sea temperature difference. For unstable conditions in the MIZ the model yields maximum ABL depths of 370 m over the ocean and 620 m over the ice. For stable conditions the ABL can be as shallow as 50 m over both water and ice.

During March of 1979 and 1981 approximately 150 radiosondes were launched in the MIZ from the R/V SURVEYOR in the Bering Sea. During three periods of northerly winds the ship steamed away from the ice while radiosondes were launched at a spacing of about 10-20 km along a track of 100 km. For this off-ice wind case Overland et al. (1983) found only a slight rise in inversion height with downwind distance despite significant warming of the boundary layer. Near the ice edge a strong inversion capping a mixed layer at about 500 m was characteristic of the ABL. The warming of the layer in the open water region by heat flux resulted in an air-sea temperature difference of about 10°C. The horizontal temperature gradient in the MIZ ABL and the change in surface roughness between pack ice and open water can combine to increase the wind speed across the region by about 10% (Overland et al., 1983).

For relatively smooth pack ice, such as in the Bering Sea, the wind-induced horizontal surface stress is the principal atmosphere-ice momentum transfer mechanism (Macklin, 1983). Observations show that the magnitude of the drag coefficient over sea ice is determined by the roughness of the surface over which the wind travels and the ABL stability. The drag coefficient is largest for unstable conditions and hence momentum transfer to the surface is most effective.

In October 1981 a series of five radiosondes were launched from the Soviet icebreaker MIKHAIL SOMOV in the Antarctic along a 150 km track from the ice edge southeastward into the

pack ice. Within the Antarctic MIZ northerly, on-ice, winds were observed. Increasing surface roughness due to increasing ice coverage decelerated the on-ice airflow within the stable ABL. The induced vertical velocity could have caused the observed inversion height increase from 491 m to 1050 m over a distance of 150 km downwind of the increased surface stress (Andreas et al., 1984).

G. HEAT BUDGET CLIMATOLOGIES

Estimates of the surface thermodynamic energy budget for the polar ocean and Norwegian-Barents Sea areas were given by Vowinckel and Orvig (1970). Results for June and July in the Norwegian Sea and the Polar Ocean are summarized in Table II. We see that the turbulent fluxes of latent and sensible heat are likely to be small, namely, less than 10 W/m^2 . This is significant because surface buoyancy fluxes are important to mixed layer evolution.

TABLE II

Estimates of the Terms in the Surface Heat Budget (After Vowinckel and Orvig, 1970).

S↓ = Shortwave Down, L↓ = Longwave Down,
L↑ = Longwave Up, in W/m²

	S↓	L↓	L↑	Net Radiation	Sensible Heat	Latent Heat	Ocean Storage
<u>Norwegian Sea Area</u>							
May	145	280	-335	90	- 5	-25	- 65
June	180	290	-340	130	+10	-10	-130
July	165	320	-350	135	+15	-10	-130
August	115	305	-350	70	+10	-25	- 60
<u>Polar Ocean Area</u>							
May	90	240	-280	50	-15	-10	- 25
June	125	275	-315	85	-10	- 5	- 65
July	125	305	-335	95	0	- 5	- 95
August	75	300	-330	45	-10	-10	- 25

III. CASE STUDIES

A. GENERAL

In this chapter the mesoscale and synoptic features and atmospheric refraction conditions observed during MIZEX-83 are examined for three case studies. Matching the refraction conditions at different locations in the MIZ during specific synoptic regimes is used to understand the variability in electromagnetic wave propagation in the region.

The refraction conditions of the marginal ice zone atmospheric boundary layer during MIZEX-83 were estimated by IREPS. Radiosonde and aircraft spiral data were the meteorological input to IREPS. The output consisted of the propagation conditions summary which contains a plot of refractivity versus height and the environmental data list which tabulates the refraction conditions for a maximum of 29 levels.

Visual and infrared imagery from the Defense Meteorological Satellite Program (DMSP) were useful in locating probable areas of electromagnetic wave ducting. Subsidence inversion bases are often located at the stratus cloud top which can be identified in DMSP imagery. Specific humidity and temperature jumps in the inversion layer can cause anomalous refraction conditions depending on their sign and magnitude. Evaporation duct heights could not be determined because the bulk exchange coefficients for the different regions of the MIZ have not been determined.

In this study, we consider different locations (over open water and dense pack ice) and different synoptic regimes (cold air advection and warm air advection). Over the open water vertical variations in the index of refraction will be related to shallow convection and surface layer mixing. Over the dense pack ice refraction conditions will be related to subsidence inversion preservation by stable conditions in the surface layer. Three case studies are examined which have the following synoptic regimes and factors:

Case 1. Warm air advection over dense pack ice causing strong elevated ducting and subrefraction from 1 to 4 July 1983.

Case 2. Cold air advection over relatively open water where normal refraction conditions were observed from 14 to 17 July 1983.

Case 3. Large scale subsidence in the western quadrants of an anticyclone leading to super-refraction and weak elevated ducting from 27 to 29 July 1983.

The factors influencing duct elevations and strengths include entrainment, subsidence, convection, and cloud top cooling/heating due to radiative transfer. Surface layer stability is another factor and can be quantitatively described by the bulk Richardson number. Errors due to radiosonde humidity sensor wetting must be considered in all interpretations. Spurious humidity jumps could cause IREPS to designate the layers as trapping layers when they may have been only super-refractive.

Horizontal homogeneity is assumed implicit in IREPS output. Clearly, the diverse mesoscale forcing mechanisms in the MIZ require that horizontal homogeneity not be applied in an area much different than that of the sounding location.

B. CASE STUDIES

1. Case 1: 1-4 July 1983

a. Synoptic and Mesoscale Features

This case pertains to a period of warm air advection over the dense pack ice region of the MIZ during which the surface layer was stable. Figures six through 16 appear at the end of this section in the order in which the soundings were made. The radiosonde launch ship, R/V POLARBJORN, was moored to an ice flow during the "drift phase" from 27 June to 8 July (Figs. 1,2).

Synoptic scale cyclones did not appear to penetrate the MIZ during the period but their track to the south had recognizable effects on MIZ weather. On 4 July a rapidly developing northeastward moving cyclone was located south of Greenland (Fig. 3). The surface wind in the MIZ shifted from the southwest (190° at 2.6 m/s on 3 July 1500 GMT) to northeast (080° at 2.6 m/s on 4 July 1200 GMT) as a flow of moist oceanic air into the cyclone developed (Fig. 4). Satellite imagery shows that the Greenland ice cap was generally covered by stratus. This implies that the landmass was dominated by high pressure. The subsiding air in the high formed a strong inversion under which the stratus formed.

The surface winds were from the open water onto the dense pack ice from 1 July 0000 GMT through 4 July 0900

GMT. The surface winds were nearly parallel to the compact ice edge from 4 July 1200 GMT through 5 July 1200 GMT. Ship-board measured sea-surface temperatures (SST) over the four-day period averaged -1.3°C with a standard deviation of $.05^{\circ}\text{C}$. The 5 m air temperatures were consistently greater than the SST throughout the period, indicating a stable surface layer (Fig. 5). Fog was observed during seven of the 11 soundings and stratus clouds were present during four of the soundings.

Advection fog extended from the surface to about 500 m on 2 July 1131 GMT but the relative humidity did not decrease from 100% until 560 m (Fig. 10). This may have been due to the humidity sensor becoming wetted in the fog and not drying out fast enough to describe the gradient change. A relatively dry layer existed above the fog until the specific humidity increased at 1200 m marking the base of a cloud layer. Within a cloud layer, from 1200 m to 2200 m, atmospheric properties are more uniform. Based on the potential temperature lapse rate the cloud top was at the same level as a subsidence inversion base. The specific humidity jump (ΔQ) at the inversion was about -3.5 g/kg and the potential temperature jump (ΔT) was 3°C .

b. Refraction Conditions

Although aircraft verification of cloud top heights are not available, the top of stratiform clouds generally marked the base of the trapping layer. The magnitude of the temperature and humidity jumps at the inversion indicate the strength and elevation of the EM ducts.

Vertical temperature and specific humidity profiles exhibit considerable variability from 1 through 4 July. Changes in specific humidity due to interspersed moist and dry layers and/or clouds caused rapidly changing refraction conditions. The IREPS propagation conditions summary for the 1 July radiosonde soundings at 0023 GMT, 0943 GMT and 2332 GMT show the persistence of elevated ducting (Figs. 7, 8,9). Assuming that errors due to radiosonde humidity sensor wetting existed, some trapping layers were probably displaced.

At 0023 GMT the trapping layer from 944 m to 1100 m was probably really located at about 500 m. This can be seen by comparing the IREPS output for the 0023 GMT sounding with that made with bogus values inserted for the same sounding (Fig. 6). The relative humidity at 0023 GMT probably decreased to a relatively low value such as 40% immediately above the stratus deck and may have caused trapping at that level.

The trapping layer from 582 m to 654 m on 2 July 1131 GMT was probably also located at about 500 m. The humidity should have decreased as the temperature increased due to subsidence. In the same sounding the strong trapping layer ($\Delta M/\Delta z = -232 \text{ km}^{-1}$) from 2229 m to 2366 m probably existed because of its association with the cloud layer (Fig. 10). Satellite imagery for 2 July 1943 GMT (Fig. 17) confirms the presence of the altocumulus layer indicated by the 2333 GMT sounding (Fig. 11). Normal refraction conditions

are indicated to have existed up to 700 mb. Convective clouds are not usually associated with trapping and in Fig. 11 the lapse rates show a change from a stable to a conditionally unstable layer above 1 km.

POLARBJORN observers reported clear skies on 3 July. The 1134 GMT propagation conditions summary indicates multiple subrefractive layers (Fig. 12). An inversion layer at 2330 GMT was associated with a weak trapping layer ($\Delta M/\Delta z = -5 \text{ km}^{-1}$) from 1490 m to 1533 m (Fig. 13). The overlying subrefractive layer was due to an increase in specific humidity from 3.8 to 4.0 g/kg in an isothermal layer.

Multiple subrefractive layers marked the bases of moist layers above a 300 m thick fog layer on 4 July at 0805 GMT. The subrefractive layer at 200 m was due to an increase in specific humidity near the top of the fog layer (Fig. 14).

On 4 July 1552 GMT POLARBJORN reported fog and in Fig. 14 a strong surface inversion is evident. The trapping layer from 285 m to 331 m was probably due to the humidity sensor becoming wetted when it passed through the shallow fog layer. The weak super-refractive layer ($\Delta M/\Delta z = +62 \text{ km}^{-1}$) at 500 m and the subrefractive layer at the base of a moist layer at 950 m were probably representative (Fig. 15).

On 4 July 2333 GMT POLARBJORN observers reported fog. The trapping layer at 308 m to 370 m was again probably a result of the humidity sensor becoming wetted. The super-refractive layer at 719 m to 803 m was probably valid because of the matching specific humidity decrease and temperature increase with height.

POLARBJORN POSITIONS
MIZEX 1983
RADIOSONDE LAUNCH POSITIONS

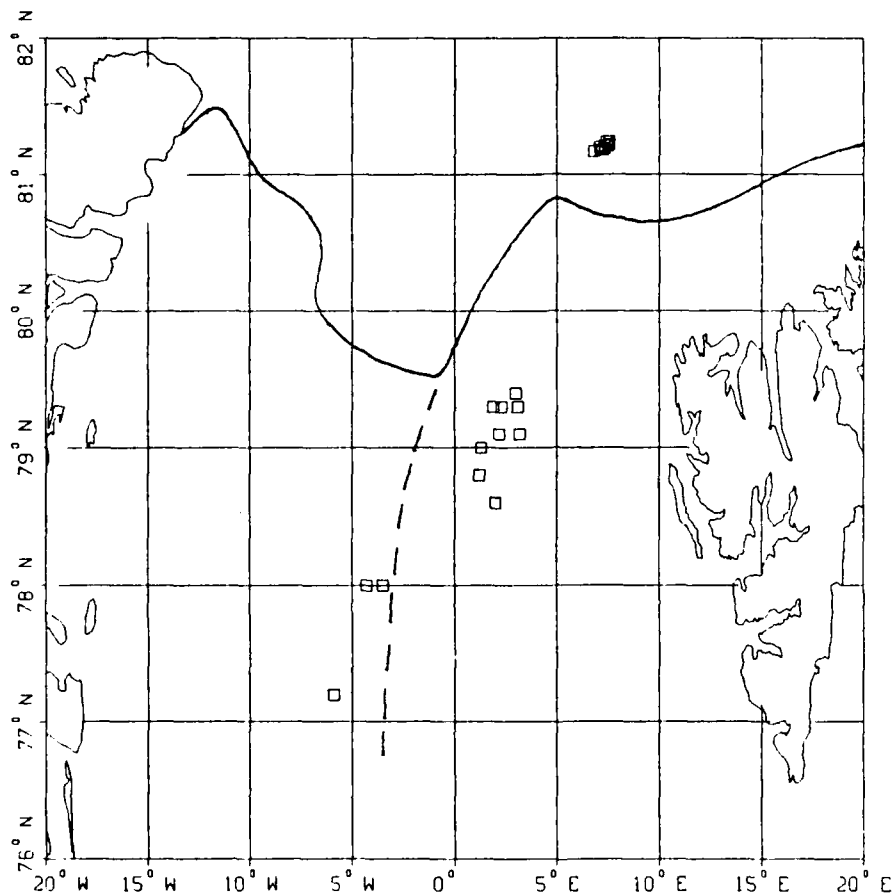


Figure 1. R/V POLARBJORN's Radiosonde Launch Positions for Three Case Studies: 1-4 July 1983, 14-17 July 1983, 27-29 July 1983. Solid Line Depicts Compact Ice Edge. Approximate Position of the Dense Pack Ice is to the West of the Dashed Line.

SOUNDING POSITIONS

MIZEX 1983

1-4 JULY

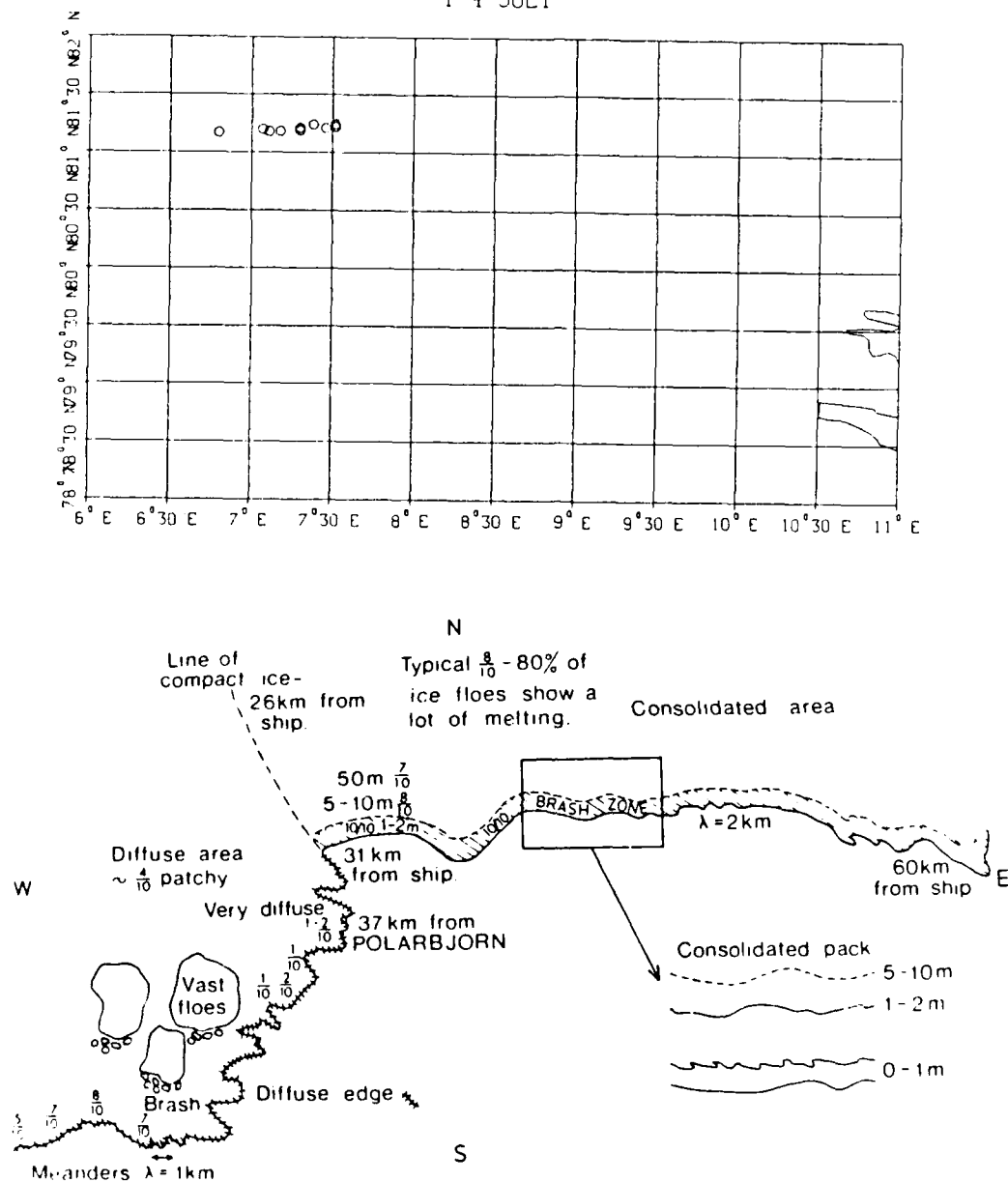


Figure 2. (a) R/V POLARBJORN's Radiosonde Launch Positions During 1-4 July 1983. (b) Ice Morphology on 1 July 1983 Relative to POLARBJORN North of Spitsbergen at about 81°N 7°E. From MIZEX-83 Data Summary, Scott Polar Research Institute.

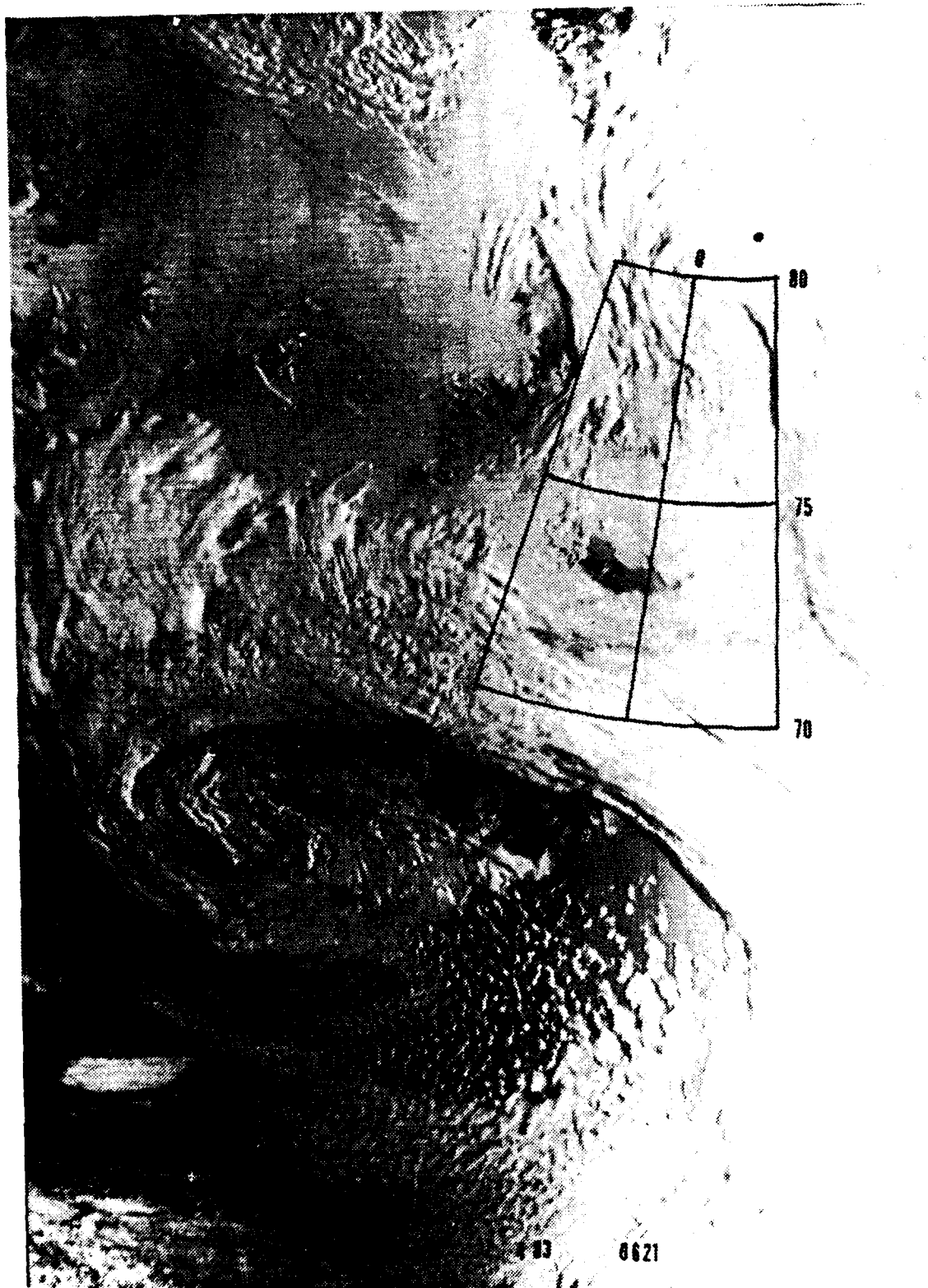
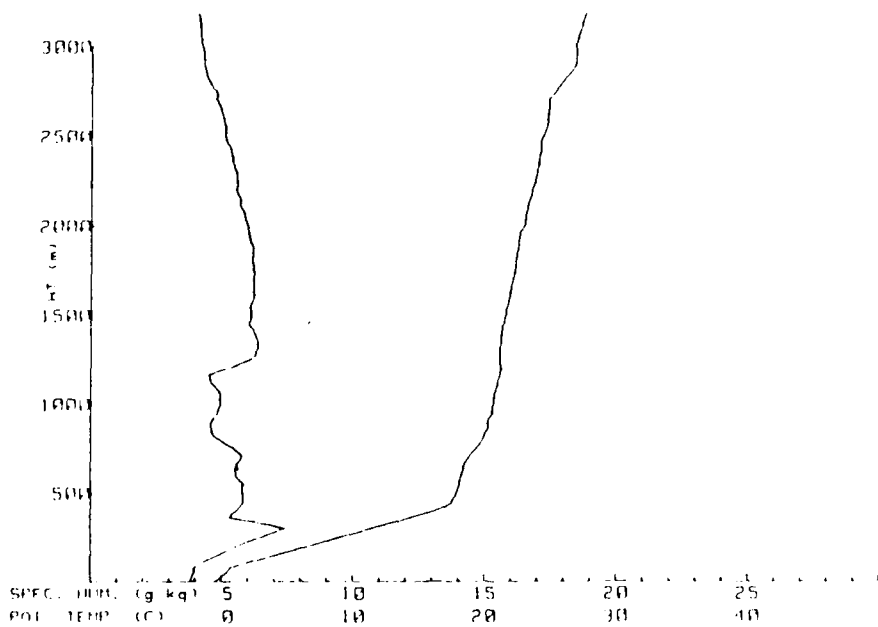


Figure 3. Visual DMSP Picture for 4 July 1983, 0621 GMT.
Grid is from 10°E to 10°W with POLARBJORN's
Position Marked by a Black Dot.



Figure 17. Visual DMSP Picture for 2 July 1983, 1943 GMT. Grid is from 10°W to 10°E with POLARBJORN's Position Marked by Black Dot.



LOCATION: 01.25N 07.16E HIZEN83
 DATE-TIME: 74-93 2333 L22

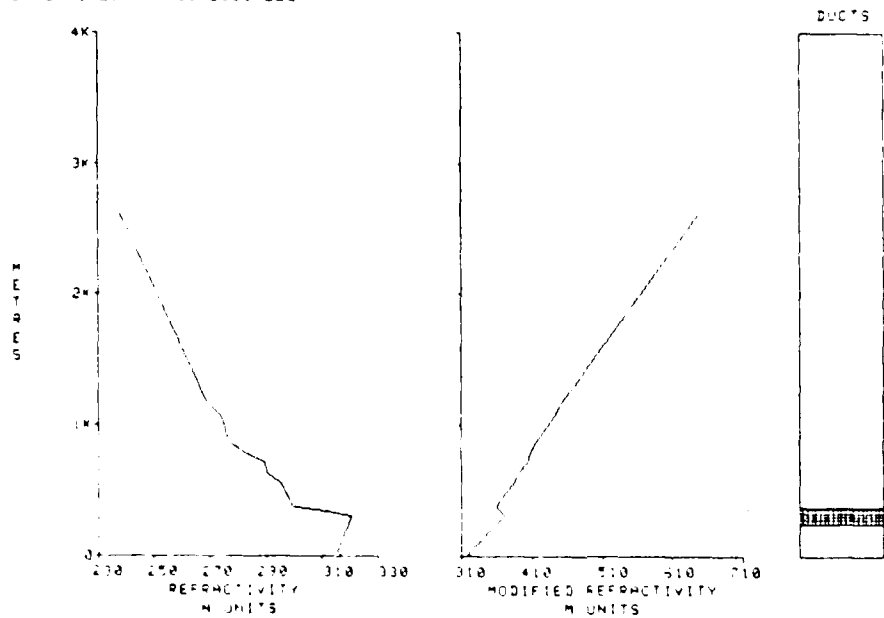
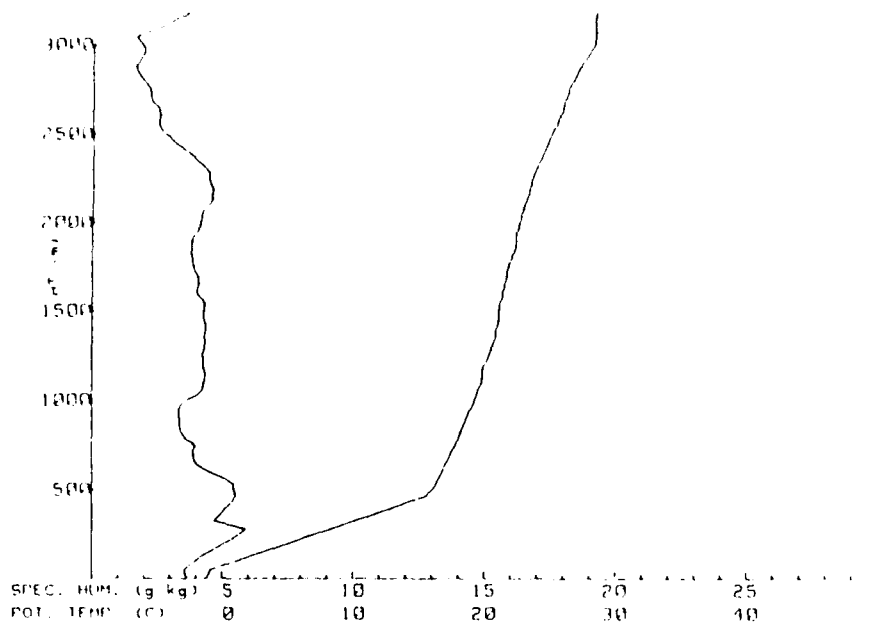


Figure 16. (a) Q and P Plot for Radiosonde Sounding for 4 July 1983, 2333 GMT. (b) IREPS output for 4 July 1983, 2333 GMT.



LOCATION: 31.24N 7.38E NIZE93
 DATE TIME: 7 4 83 1552Z L21

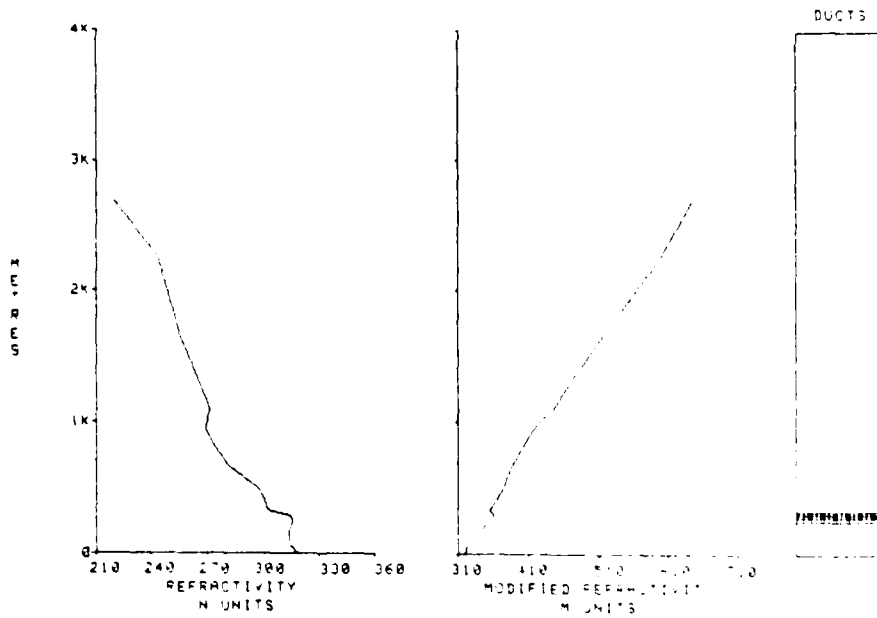
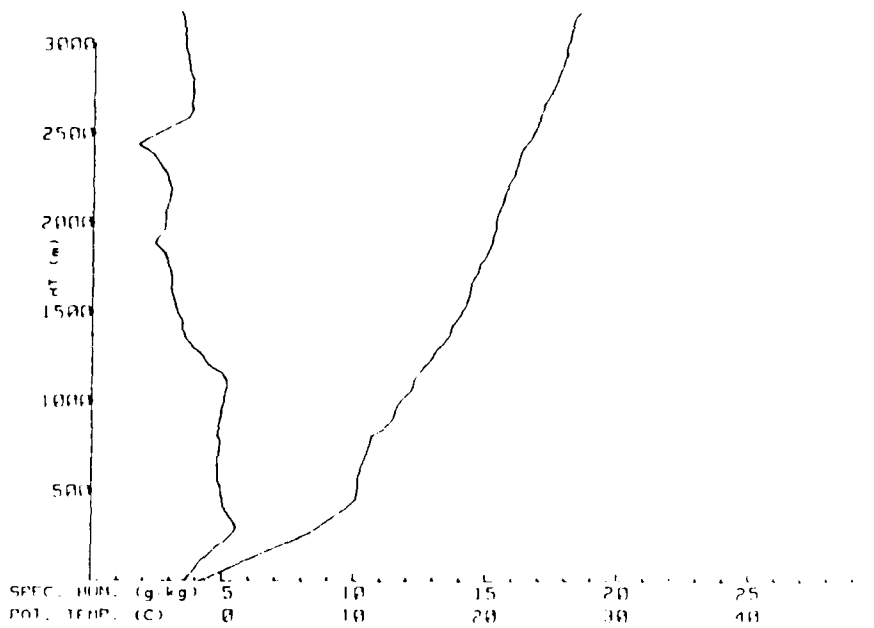


Figure 15. (a) Q and θ Plot for Radiosonde Sounding 4 July 1983, 1522 GMT. (b) IREPS Output for 4 July 1983, 1552 GMT.



LOCATION: 01.24N 7.52E MIZEX83
 DATE/TIME: 7 4 83 0805Z L20

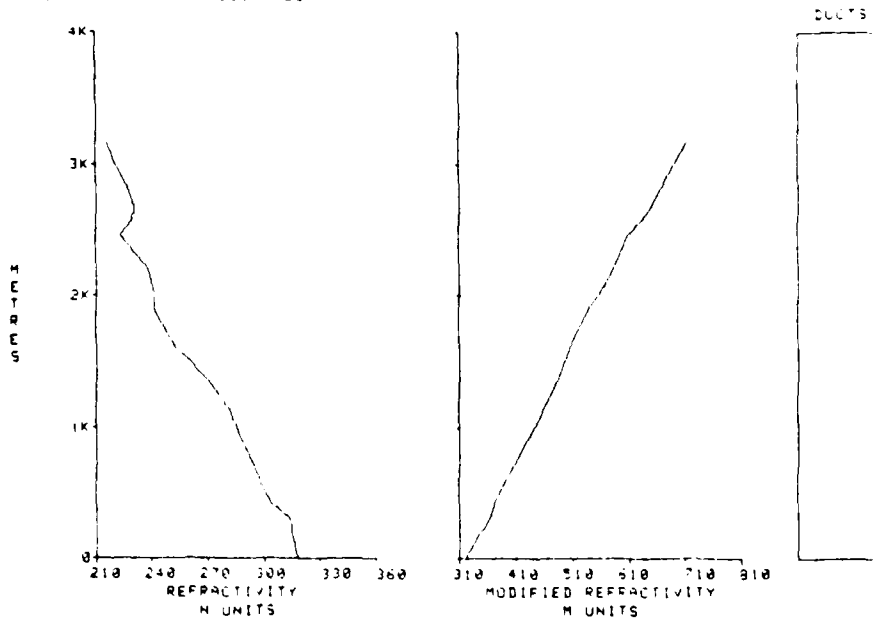
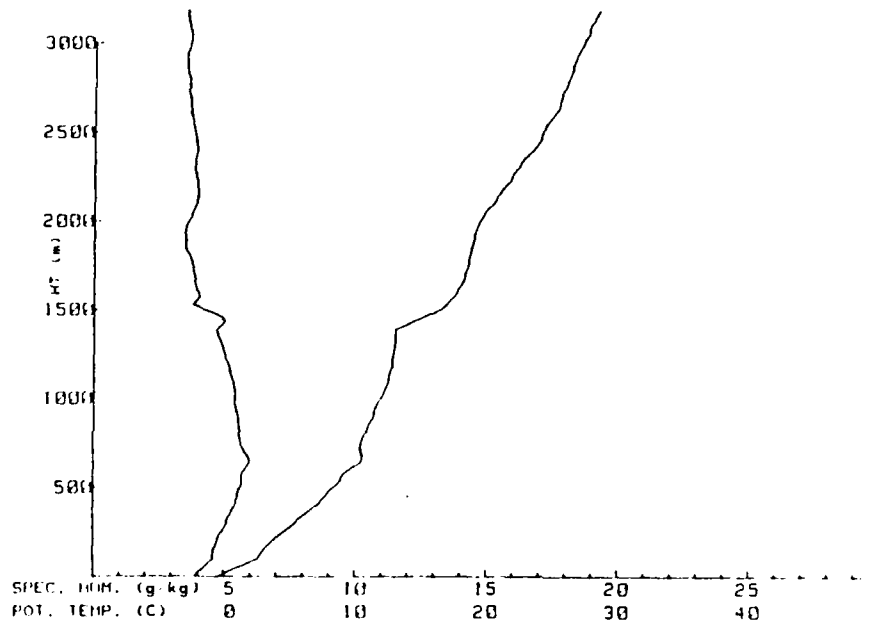


Figure 14. (a) Q and θ Plot for Radiosonde Sounding
 4 July 1983, 0805 GMT. (b) IREPS Output
 for 4 July 1983, 0805 GMT.



LOCATION: 01.21N 7.46E M12EX83
 DATE/TIME: 7/3/83 2330 L19

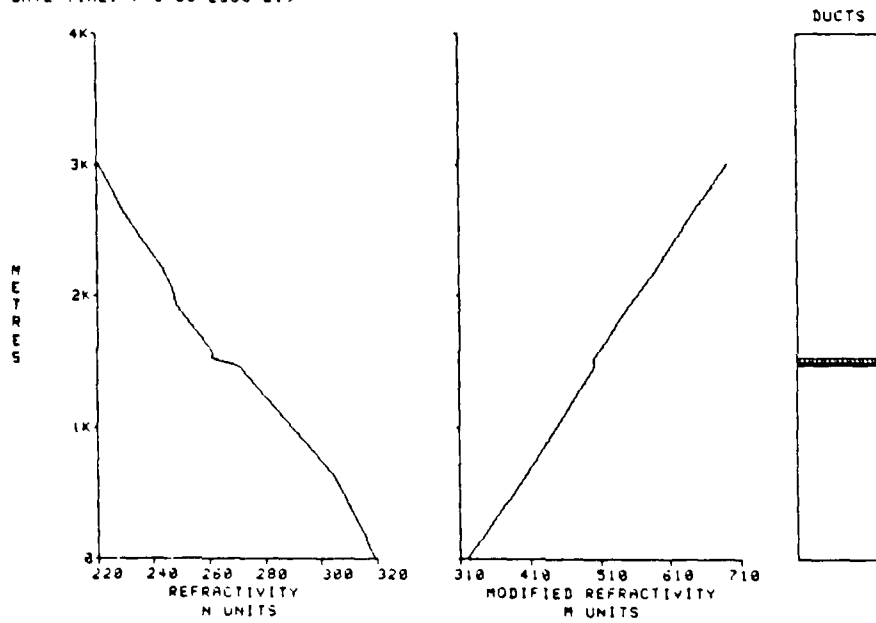
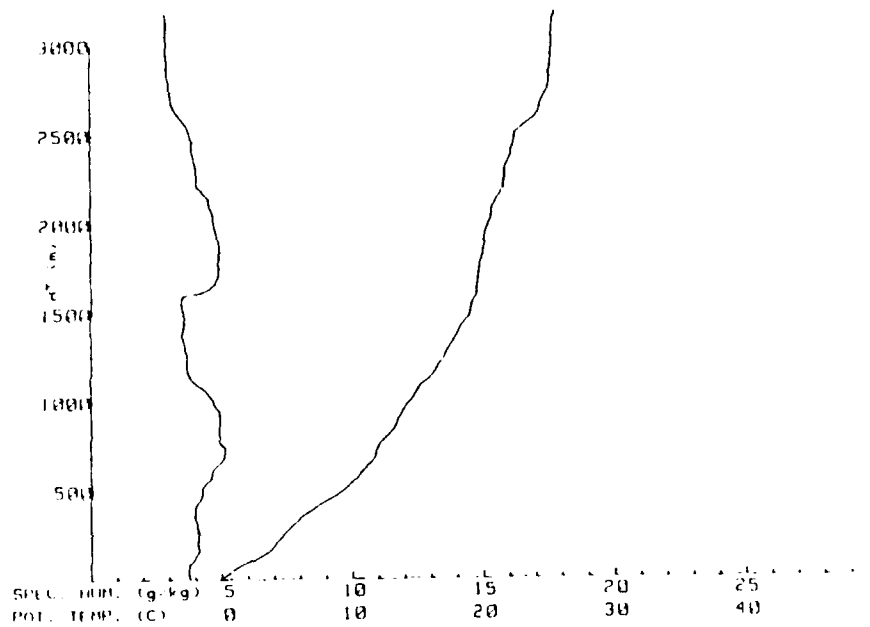


Figure 13. (a) Q and θ Plot for Radiosonde Sounding
 3 July 1983, 2330 GMT. (b) IREPS Output
 for 3 July 1983, 2330 GMT.



LOCATION: 81.22N 7.52E MIZEX83
 DATE-TIME: 7-3-83 1134Z L18

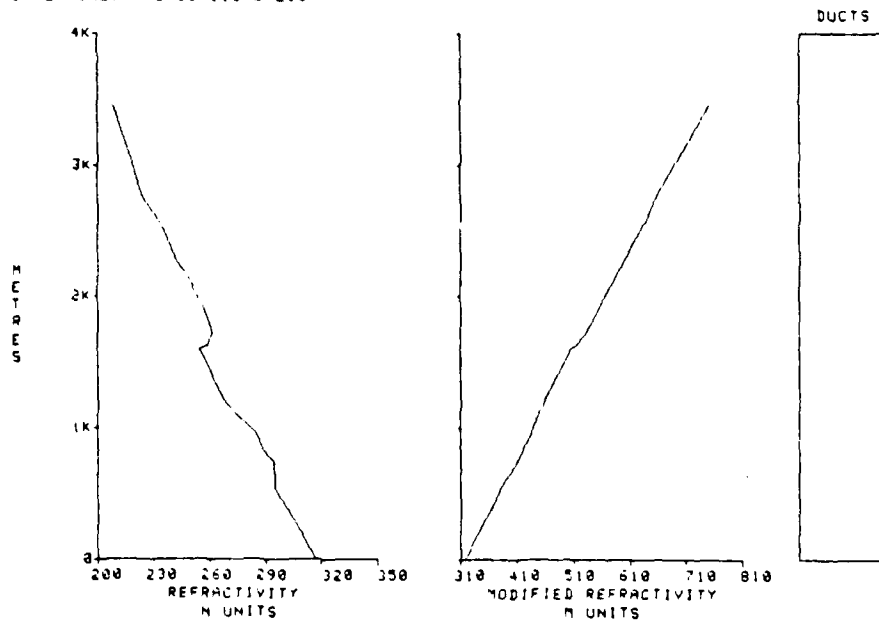
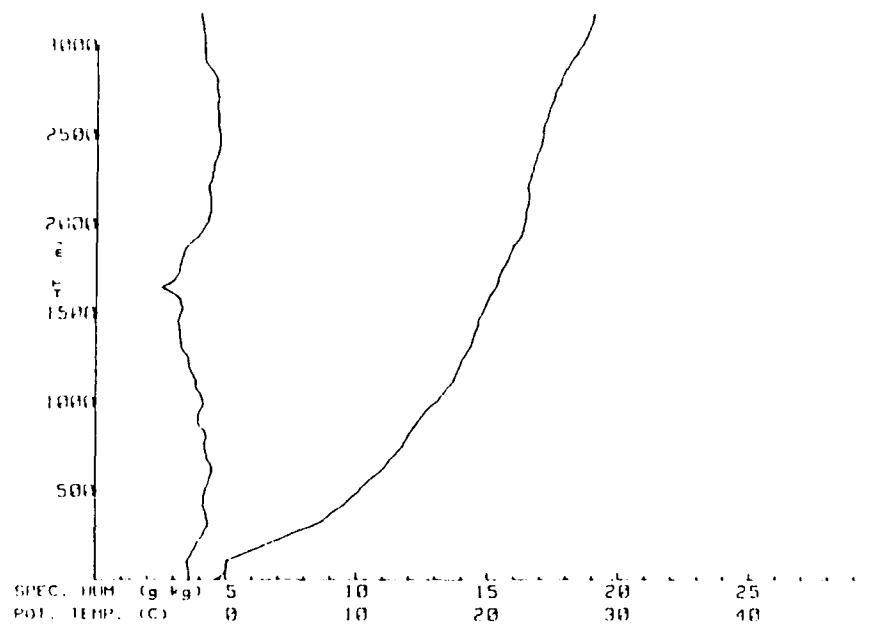


Figure 12. (a) Q and θ Plot for Radiosonde Sounding
 3 July 1983, 1134 GMT. (b) IREPS Output for
 3 July 1983, 1134 GMT.



LOCATION: 81.19N 7.1E
 DATE TIME: 7-2-83 233332 MIZEX83

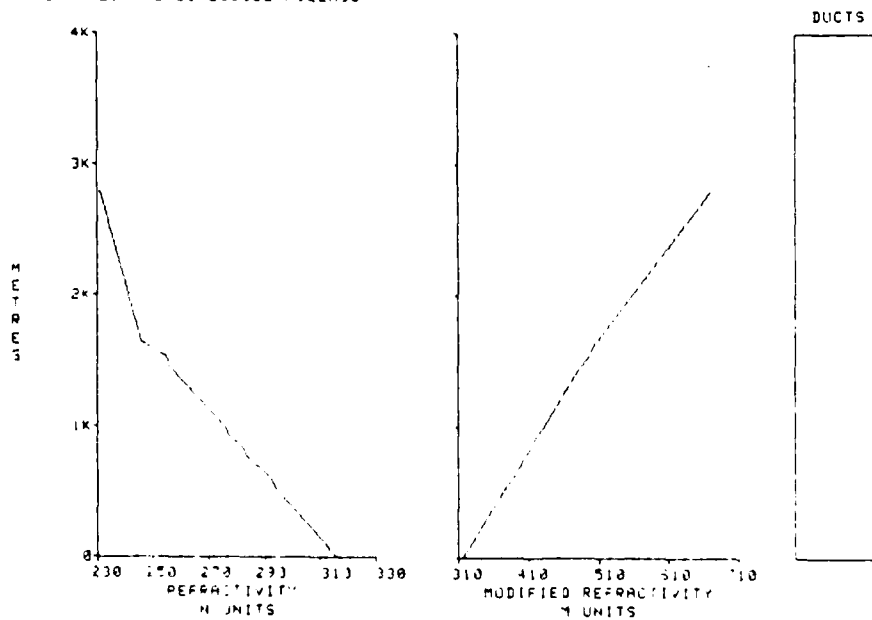
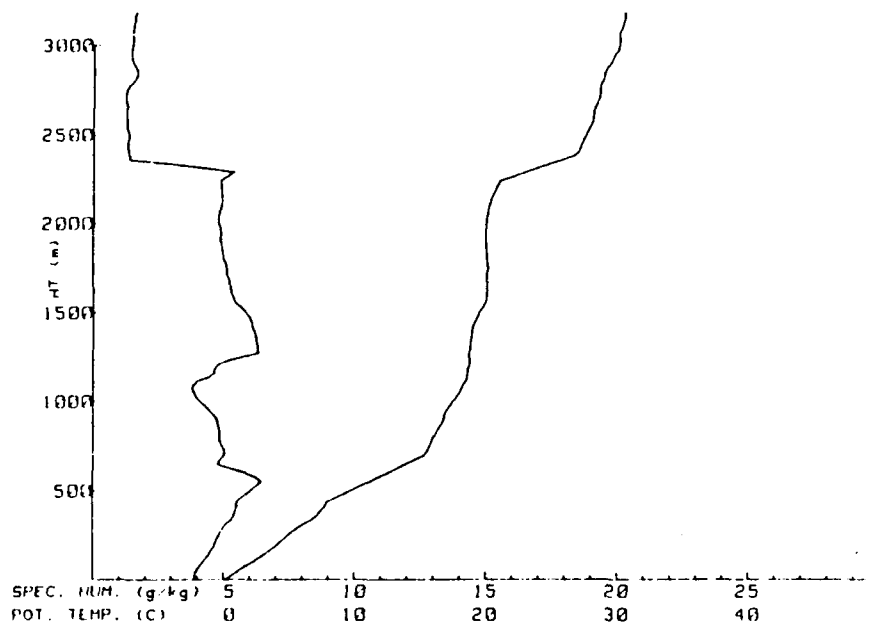


Figure 11. (a) Q and θ Plot for Radiosonde Sounding 2 July 1983, 2333 GMT. (b) IREPS Output for 2 July 1983, 2333 GMT.



LOCATION: 91.21N 7.3E
 DATE-TIME: 7 2 83 1131Z 112EX83

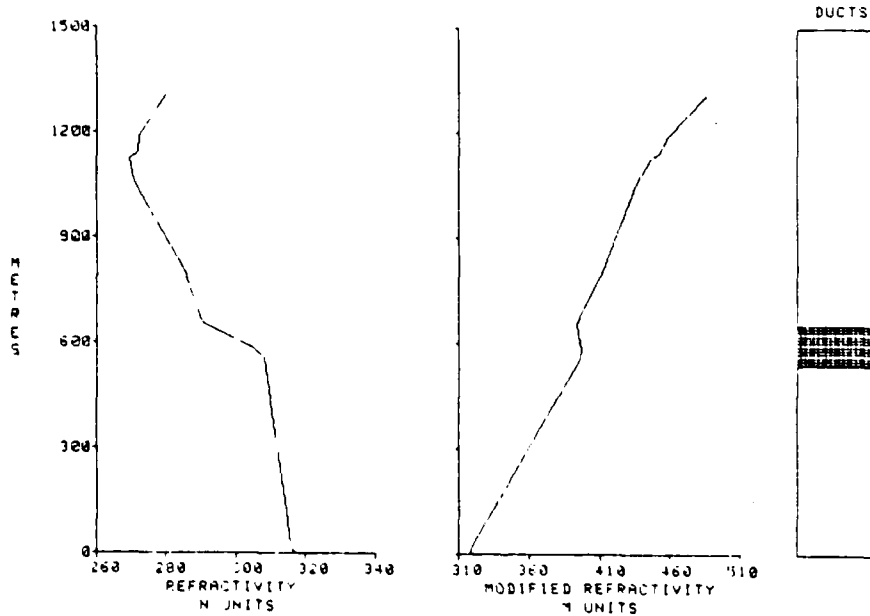
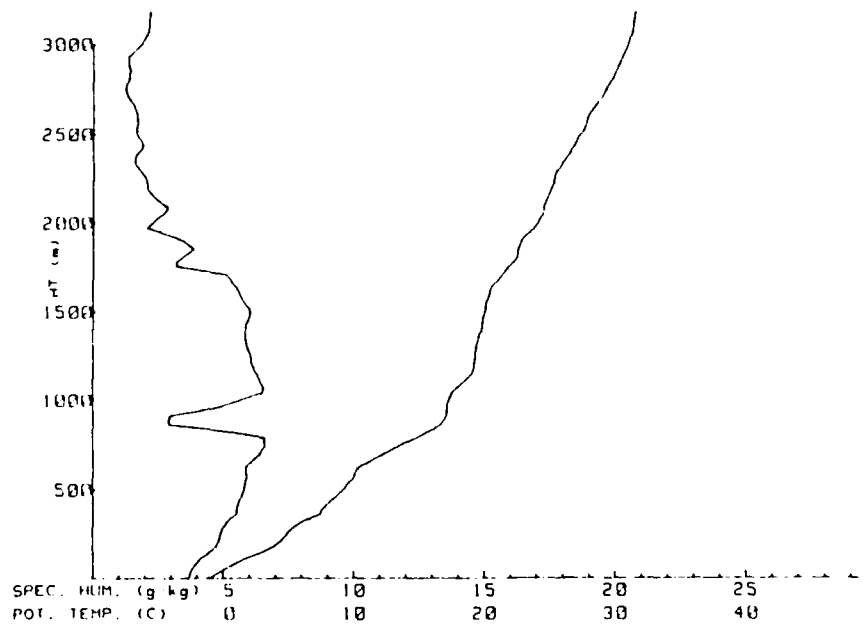


Figure 10. (a) Q and θ Plot for Radiosonde Sounding
 2 July 1983, 1131 GMT. (b) IREPS Output for
 2 July 1983, 1131 GMT.



LOCATION: 01.10N 7.11E M12EX03
 DATE-TIME: 7/1-83 2332Z

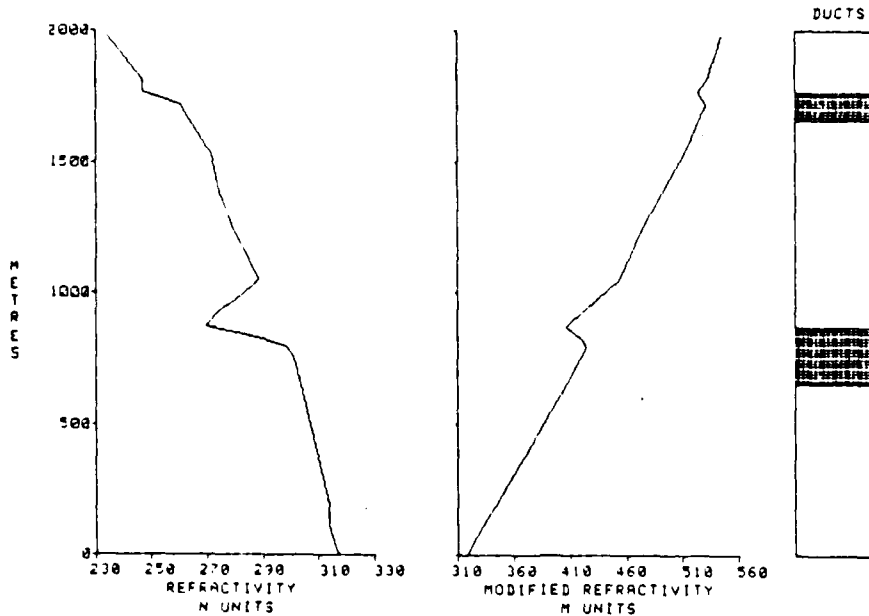
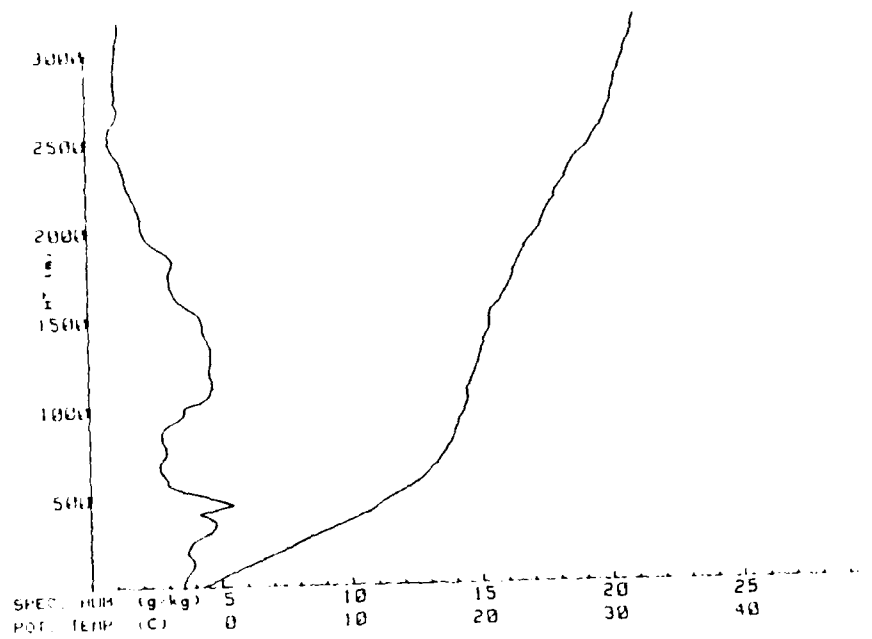


Figure 9. (a) Q and θ Plot for Radiosonde Sounding 1 July 1983, 2332 GMT. (b) IREPS Output for 1 July 1983, 2332 GMT.



LOCATION: 81.20N 7.07E M12EX83
 DATE/TIME: 1/7/83 0943Z

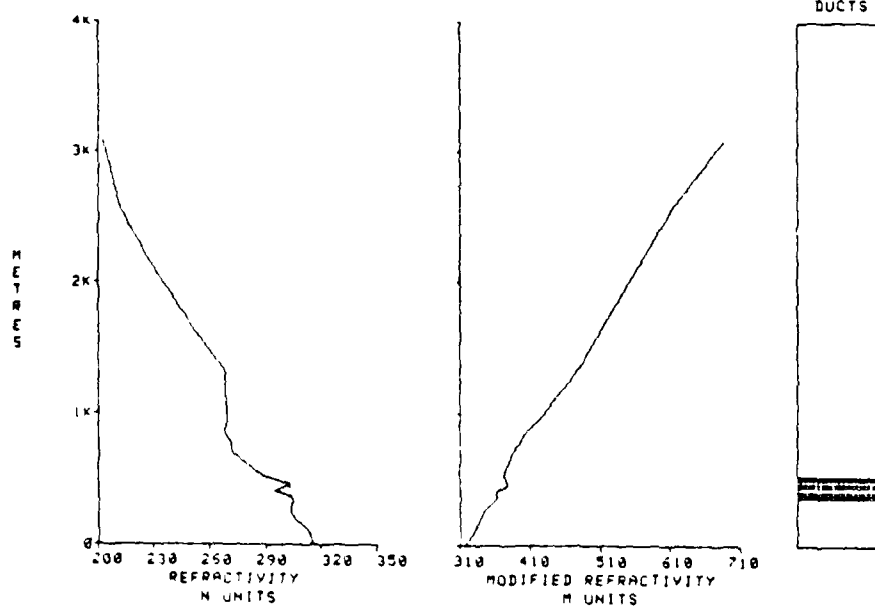
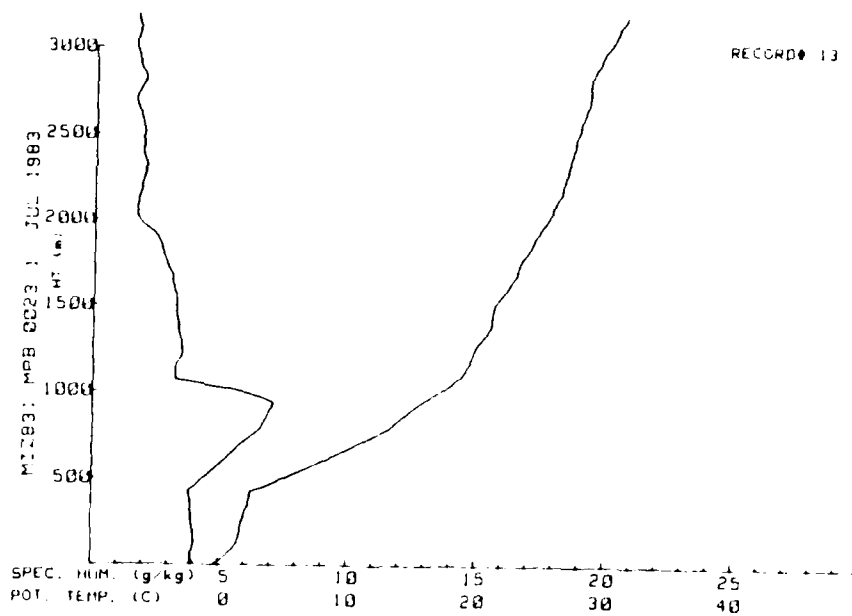


Figure 8. (a) Q and θ Plot for Radiosonde Sounding
 1 July 1983, 0943 GMT. (b) IREPS Output for
 1 July 1983, 0943 GMT.



**** PREPARATION CONDITIONS SUMMARY ****

LOCATION: 91.7N 6.90E MIZ83
 DATE-TIME: 71: 83 0023Z

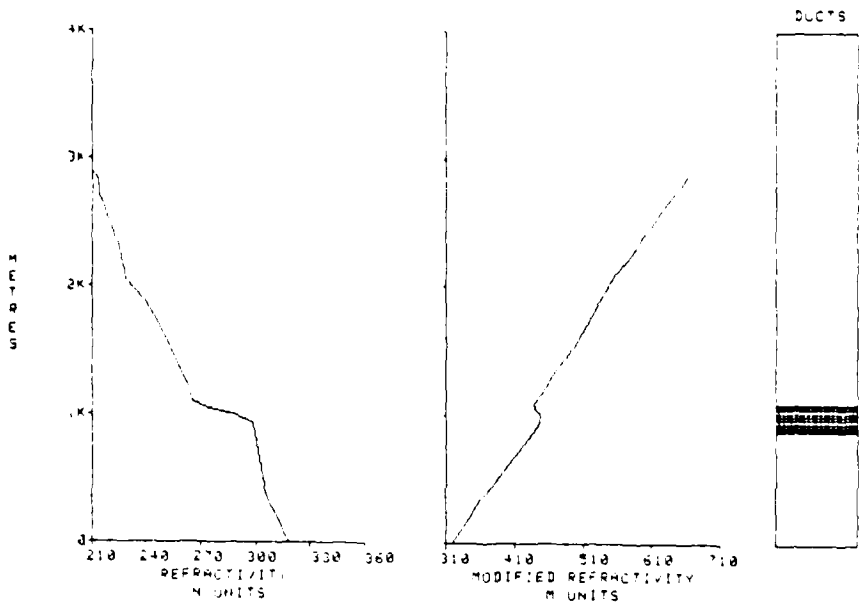
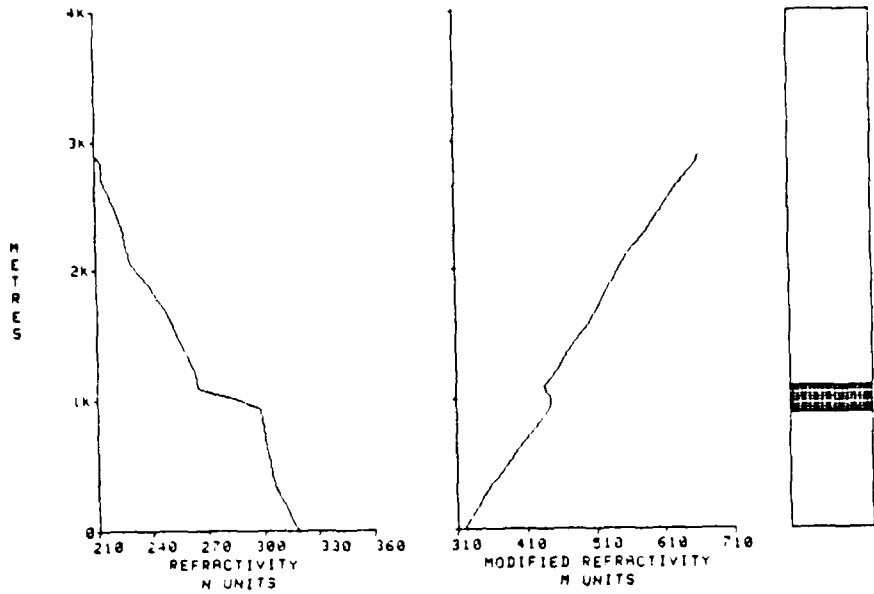


Figure 7. (a) Q and θ Plot for Radiosonde Sounding 1 July 1983, 0023 GMT. (b) IREPS Output for 1 July 1983, 0023 GMT.

LOCATION: 31.7N 6.80E MICE83
 DATE TIME: 7 1 83 0023Z



LOCATION: 31.7N 6.80E MICE-83
 DATE TIME: 7 1 83 0023Z 80505

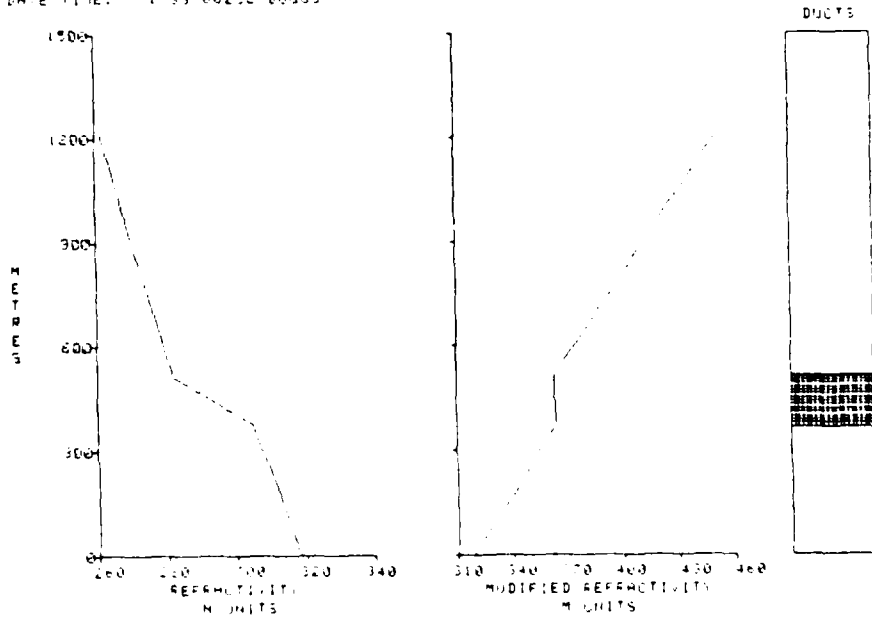
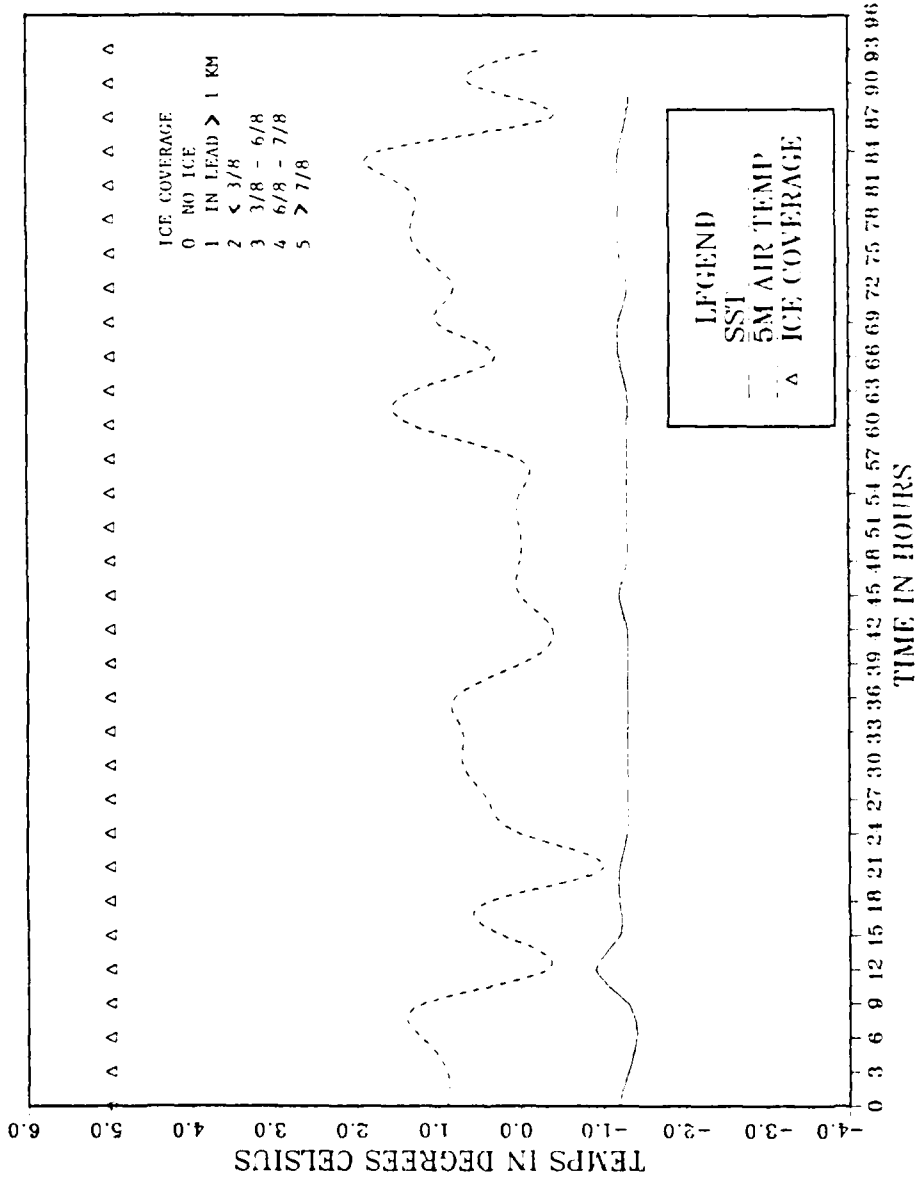


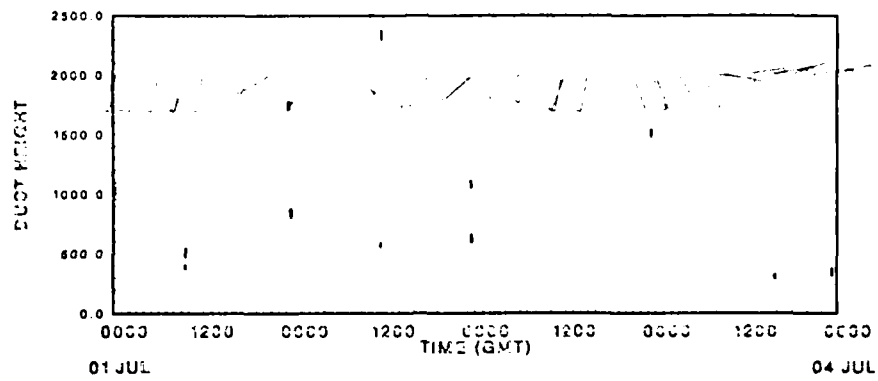
Figure 6. (a) IREPS Output for 1 July 1983, 0023 GMT.
 (b) IREPS Output for 1 July 1983, 0023 GMT
 with Bogus Relative Humidity Value of 40%
 Inserted at 500 m.

MIZEX83 DATA

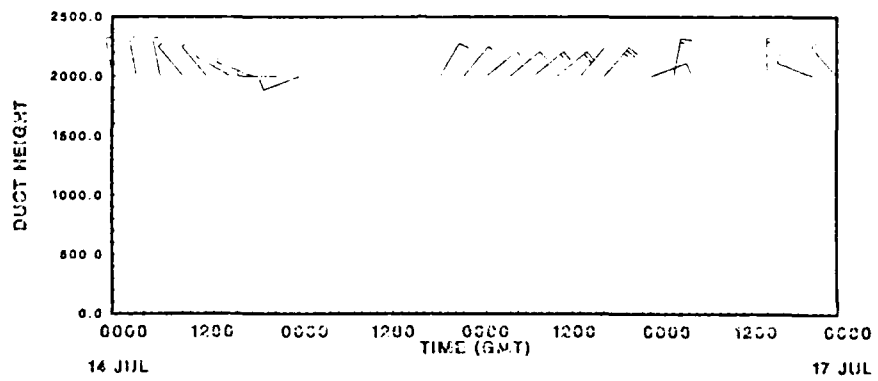


1-4 JULY 1983

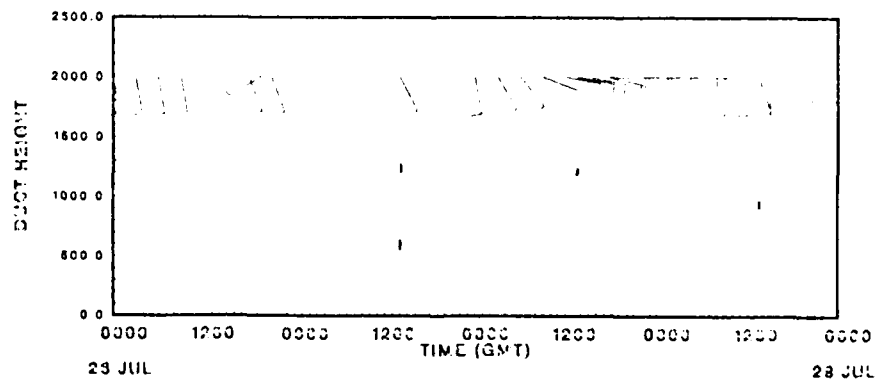
Figure 5. Ice Coverage, 5 m Air Temperature and Sea-surface Temperature for 1-4 July 1983



1 - 4 JULY MIZEX-83



14-17 JULY MIZEX-83



27 - 28 JULY MIZEX-83

Figure 4. Wind Velocity Vectors and Duct Thicknesses for 1-4 July, 14-17 July, 26-29 July MIZEX-83

2. Case 2: 14-17 July 1983

a. Synoptic and Mesoscale Features

This case pertains to a period of cold air advection over the open pack ice and open water regions of the MIZ during which the surface layer was near-neutral (Figs. 18, 19). Figures 22-31 appear at the end of this section in the order which the soundings were made. Wind directions were variable but were predominantly from the compact ice toward the open water at 2.5 m/s to 10 m/s.

Synoptic scale cyclones moved eastward on a path south of Iceland on 14 July and 17 July. Surface analyses prepared at Tromso, Norway show a stationary high pressure ridge over the Greenland ice cap (Fig. 20). The 14 July 0432 GMT visual picture shows stratocumulus clouds over the MIZ and a cyclone at 70°N (Fig. 21). The Greenland ice cap appears to have been partly covered by stratus.

Radiosonde soundings show that the mesoscale structure was dominated by lower level convection and turbulent mixing. Lapse rates above the surface layer were conditionally unstable since they were less than the dry-adiabatic lapse rate but greater than the saturated adiabatic lapse rate.

The 14 July 2022 GMT sounding indicates a near-neutral surface layer with higher mean specific humidity than the layers above (Fig. 22). The first 100-200 m of the radiosonde sounding may not be completely representative of the actual environment because of sensor response and the balloon

ascent rate. Therefore, the air-sea temperature difference may be a better indication of surface layer stability. The near-neutral stability is confirmed by Fig. 19. The 2100 GMT shipboard observation recorded the sea-surface temperature as 0.4°C warmer than the 5 m air temperature which agrees with the surface layer near-neutral lapse rate in Fig. 19. A stratocumulus layer was observed from POLARBJORN. The sounding indicates that a saturated lapse rate extended up to a capping inversion at 1430 m.

Further information is gained from measurements taken by an aircraft flying spiral patterns at locations over the ice and over the water on 15 July at 2004 GMT and at 1809 GMT respectively (Fig. 23). The aircraft over-water location was about 88 km southwest of POLARBJORN where the SST was -0.3°C and the five meter air temperature was 0.1°C at 1800 GMT. The spiral soundings indicate significant air temperature differences between the two locations. The 1809 GMT sounding air temperature at 18 m was 0.7°C and the 2004 GMT sounding air temperature at 9 m was -0.8°C . Of interest is the well defined capping subsidence inversion at about 600 m over the ice at 2004 GMT. The surface layer appears to have been stable and moist. Over the open water the lapse rate indicates conditional instability and the boundary layer is difficult to define. A temperature inversion base at 2100 m may be the same inversion layer detected by radiosonde at 1900 m 3.5 hours later at 2335 GMT and 180 km to the southeast. The 2014 GMT satellite visual picture shows altocumulus clouds

over the MIZ. To the west the orographic effect of the east Greenland coast caused cirrus clouds to form in the lee (to the west) of the coastal mountain range on 16 July 1954 (Fig. 32).

b. Refraction Conditions

Cold air advection over the relatively warmer open pack ice and open water region of the MIZ probably produced shallow convection during the period. The refraction conditions were therefore normal due to mixing above the surface layer. The surface layer stability varied about neutral depending on the surface air-sea temperature difference and mixing.

An aircraft spiral sounding made on 15 July at 2105 GMT over open water at 79.05°N 3.50°E showed a stable, moist surface layer (Fig. 31). A very weak super-refractive layer may have extended from 8 m to 51 m ($\Delta M/\Delta z = +72 \text{ km}^{-1}$). Observations from POLARBJORN at 21 GMT at 79.1°N 2.5°E show that the surface layer was stable and that the surface wind was from 040° at 4.6 m/s.

The IREPS output for 15 July 1134 GMT at 79.27°N 3.12°E and 16 July 1147 GMT at 79.22°N 3.17°E (Figs. 24,27) indicate normal refraction conditions up to 700 mb. The IREPS output for 17 July 1415 GMT at 78.98°N 1.31°E (Fig. 29) also indicates normal refraction conditions. A recurring feature in vertical profiles over the water has been a slight increase in specific humidity at the same level as a temperature inversion. Commonly called frontal inversions, these features

are generally associated with stratocumulus and altocumulus in the MIZ. POLARBJORN's location varied from open water on 16 July 1734 GMT to very open pack ice at 2333 GMT and to open pack ice throughout 17 July. The 5 m air temperatures were consistently less than the sea surface temperatures from 16 July 1500 GMT throughout 17 July. The wind was off-ice throughout the lower troposphere during the period.

The warm, moist layer could have been advected over the colder boundary layer but such a process would have resulted in strong vertical wind shear. There was some vertical wind shear evident at each temperature inversion but the inversion and boundary layers were under the influence of off-ice advection in each case. The 16 July 1953 GMT visual satellite picture (Fig. 33) shows a cyclone directly to the east of the MIZ which may have been responsible for the northeasterly surface winds observed on 16 July. The warm, moist air associated with the cyclone could have been advected into the MIZ where the lower layers would have been cooled by the ice.

The 17 July 2331 GMT sounding shows an increase in relative humidity from 92% to 96% (the specific humidity increased from 2.6 to 3.4 g/kg) as the temperature increased from -6.0°C to -3.5°C in a layer from 1108 m to 1391 m (Fig. 30). Normal refraction conditions were indicated for the layer. Satellite pictures for 17 July 1932 GMT show stratocumulus covering the sounding location (Fig. 34) and the effects of a well developed cyclone centered to the south of the MIZ which extended as far north as 75°N .

SOUNDING POSITIONS MIZEX 1983 14-17 JULY

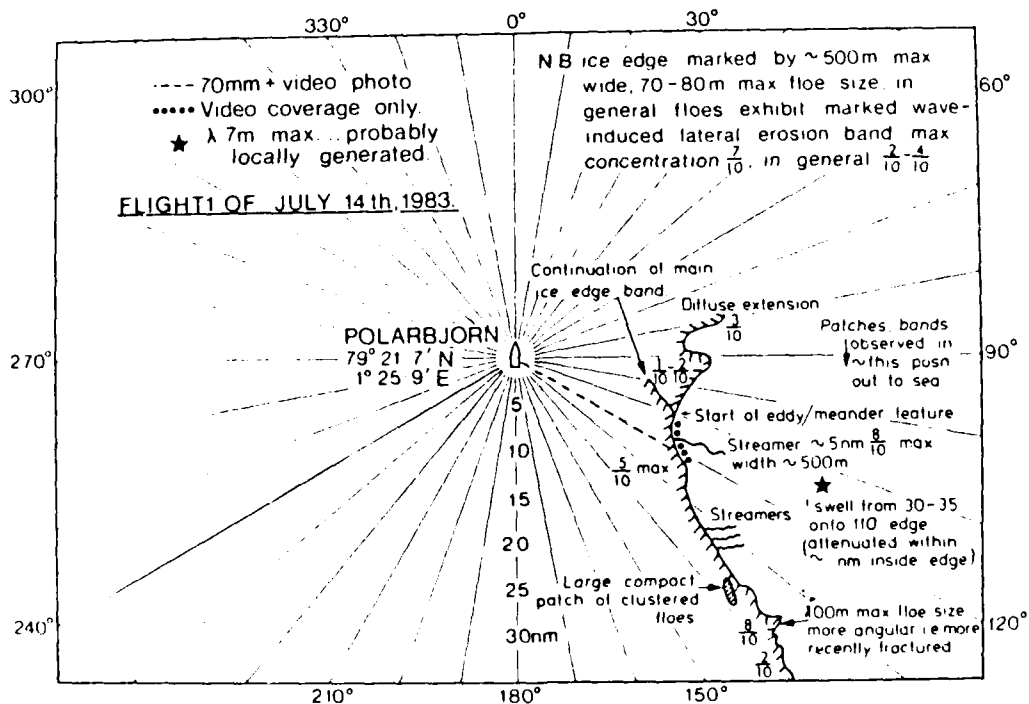
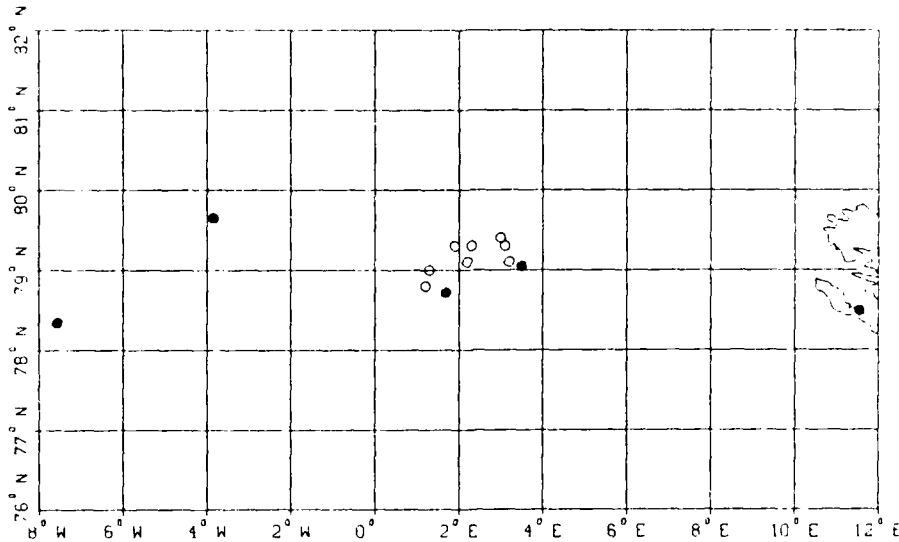
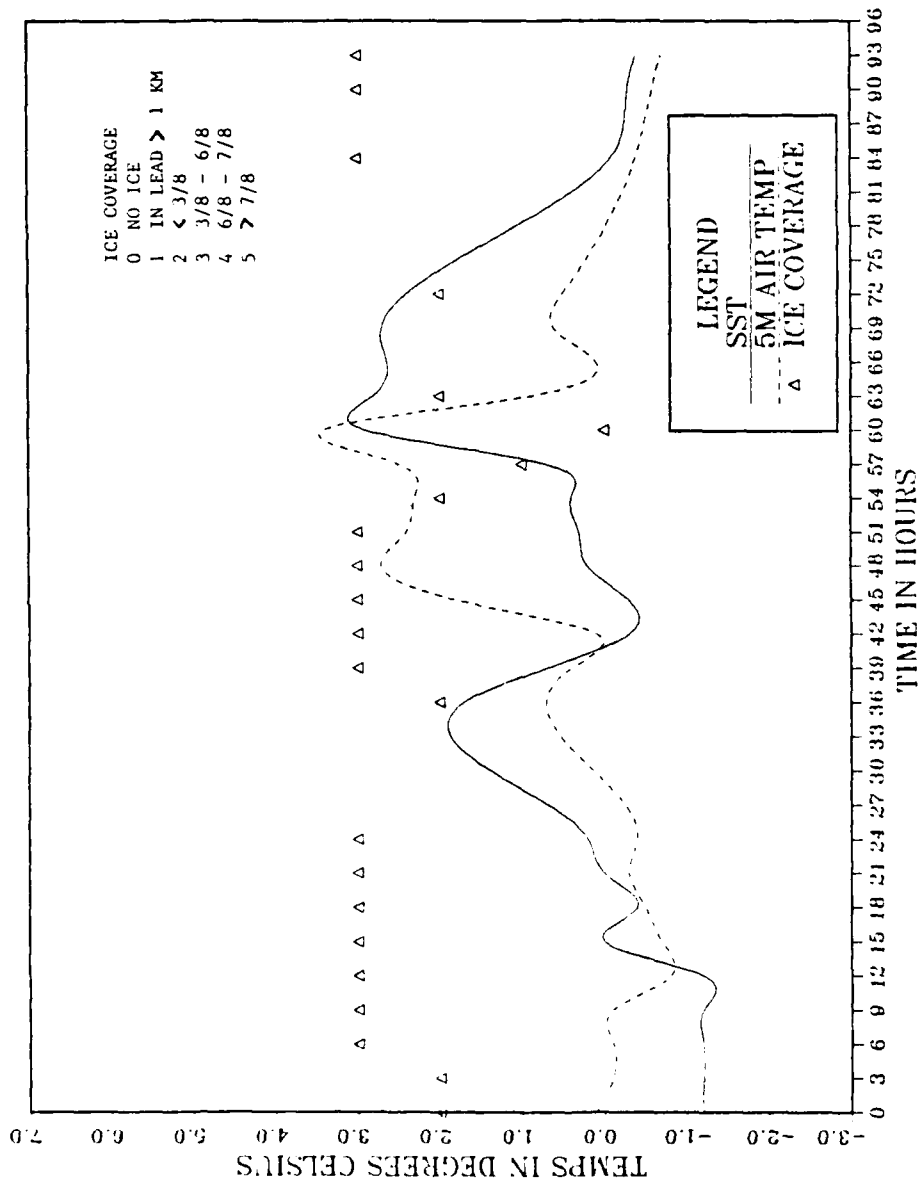


Figure 18. (a) Radiosonde (o) and Spiral Sounding (·) Start Positions During 14-17 July MIZEX-83. (b) Ice Morphology on 14 July 1983 Relative to POLARBJORN's Position.

MIZEX83 DATA



14-17 JULY 1983

Figure 19. Ice Coverage, 5 m Air Temperature and Sea Surface Temperature for 14-17 July 1983

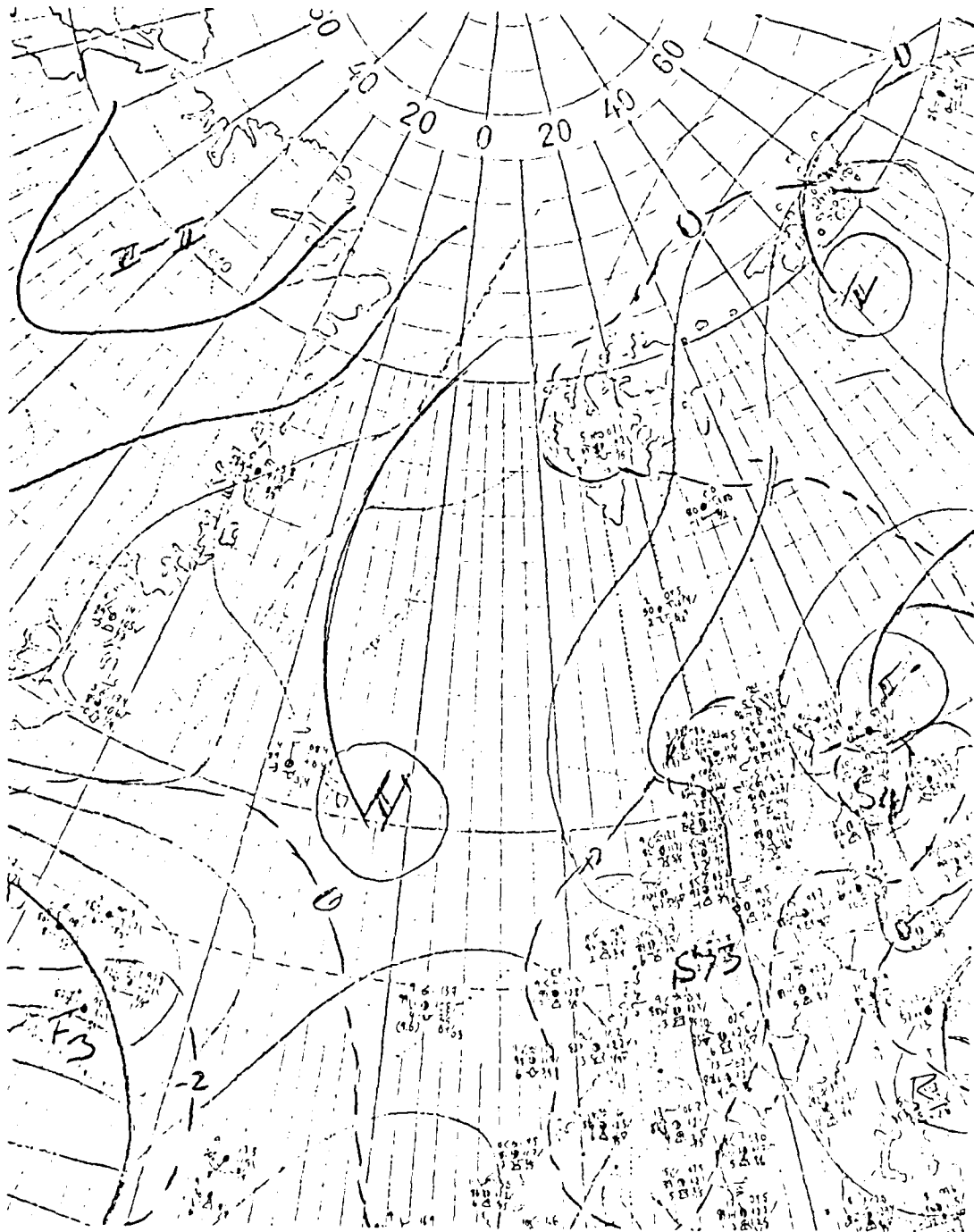


Figure 20. Surface Analyses for 16 July 1983, 1500 GMT



Figure 21. Visual DMSP Picture at 14 July 1983, 0432 GMT.
Grid is from 10°W to 10°E with POLARBJORN's
Position Marked by Black Dot.

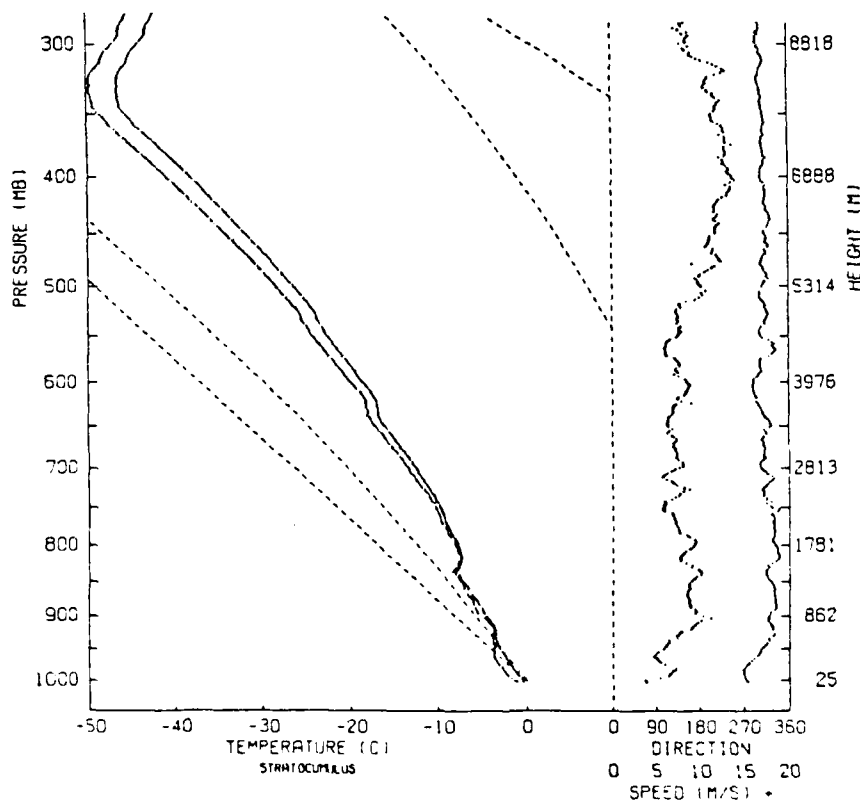
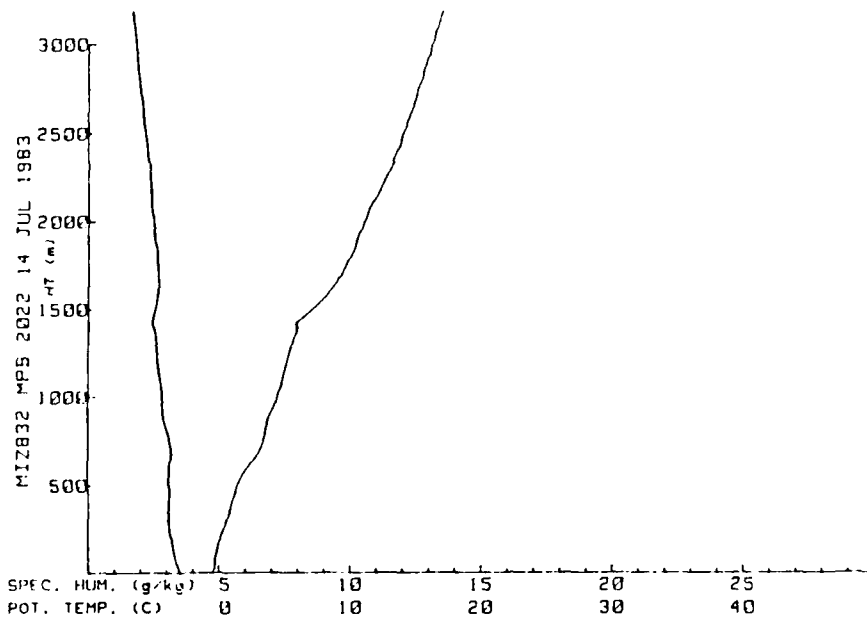


Figure 22. (a) Q and θ Plot for Radiosonde Sounding 14 July 1983, 2022 GMT. (b) T and T_d Plot for Radiosonde Sounding 14 July 1983, 2022 GMT

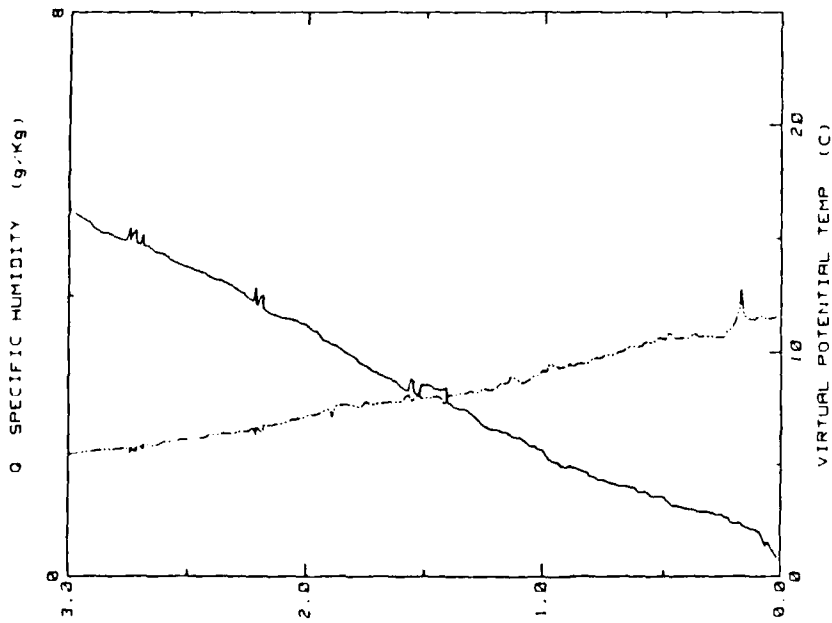
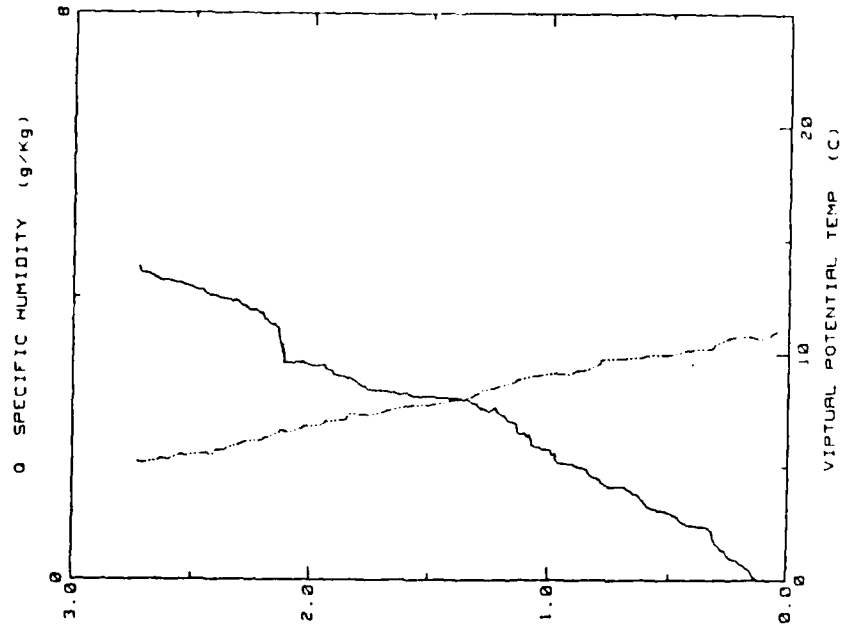
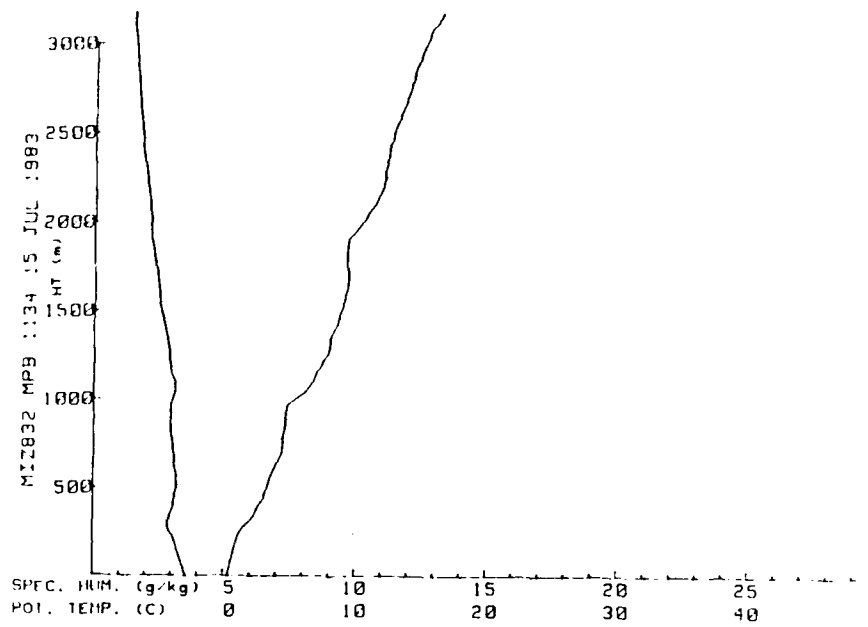


Figure 23. (a) Q and θ Plot for Spiral Sounding 15 July 1983, 1809 GMT. (b) Q and θ Plot for Spiral Sounding 15 July 1983, 2004 GMT.



OPERATIONS SECTION
 DATE TIME: 0 15 83 1134Z MIDE83

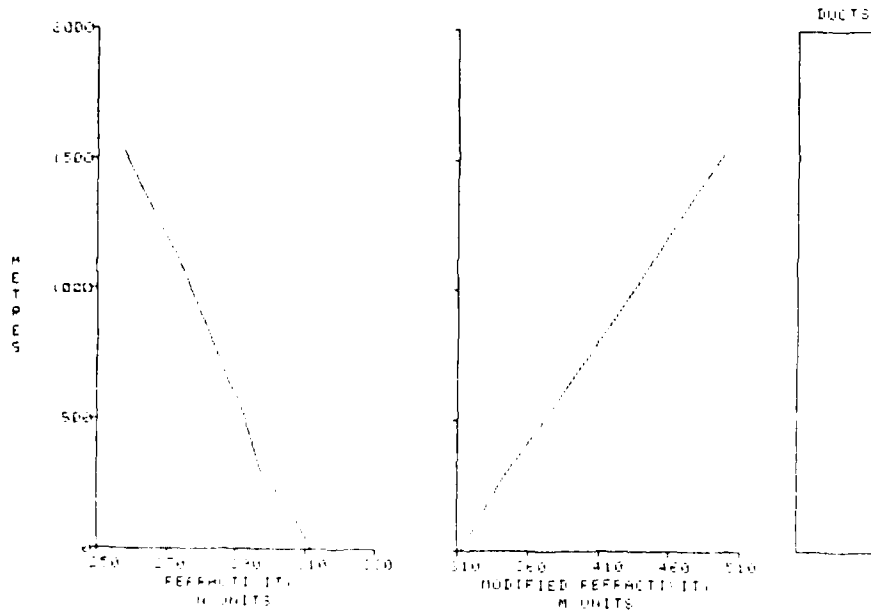
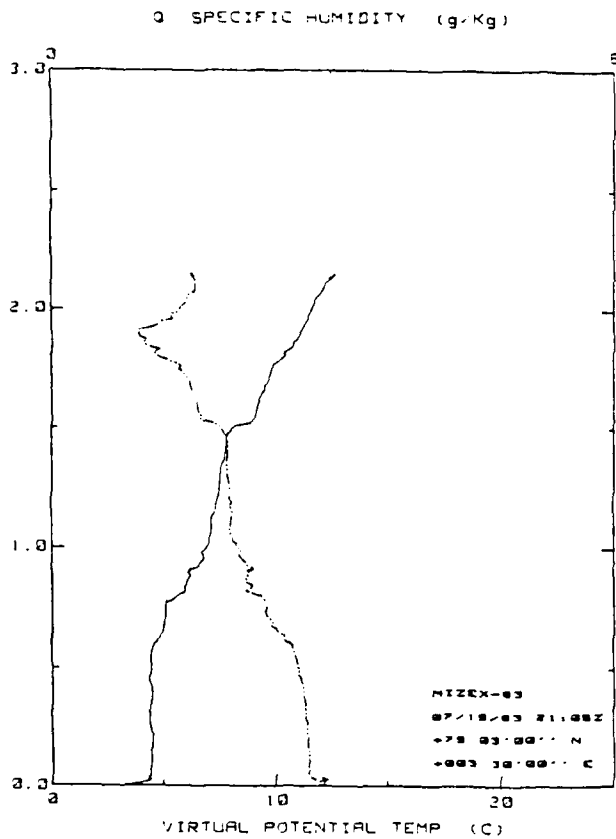


Figure 24. (a) Q and θ Plot for Spiral Sounding 15 July 1983, 1134 GMT. (b) IREPS Output for 15 July 1983, 1134 GMT.



LOCATION: 29 03 00N 003 30 00E
 DATE TIME: 7 15 83 2105Z NIZEX03 A

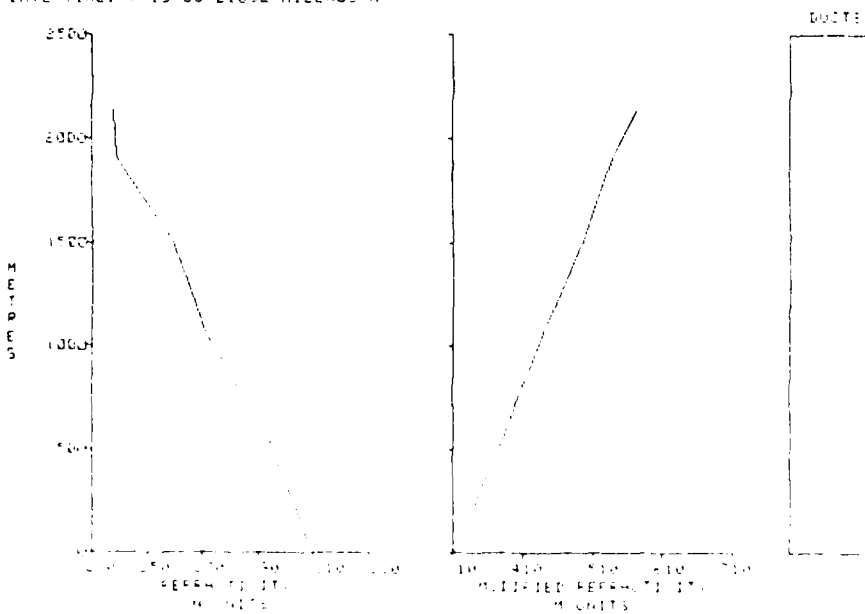


Figure 25. (a) Q and σ Plot for Spiral Sounding 15 July 1983, 2105 GMT. (b) IREPS Output for 15 July 1983, 2105 GMT.

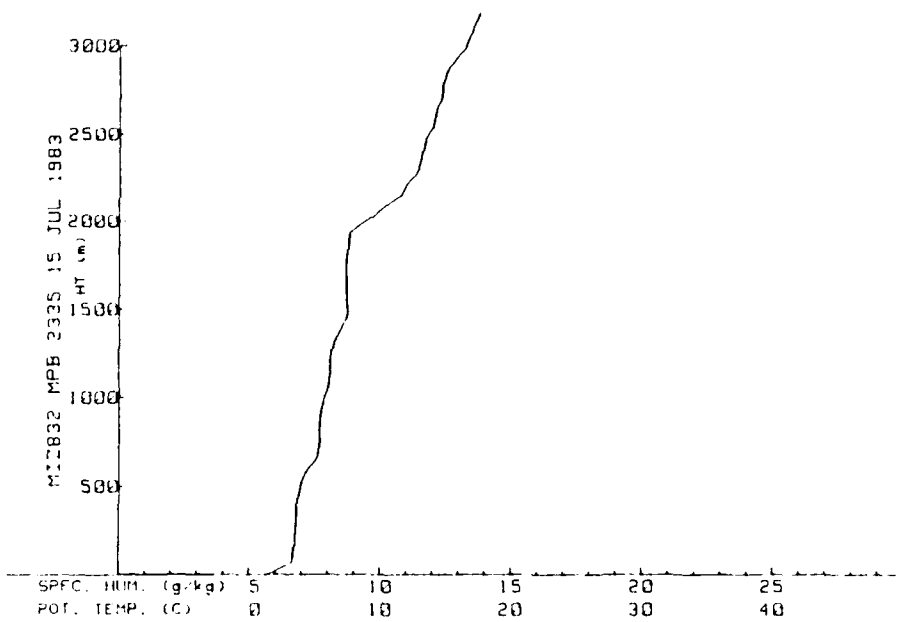
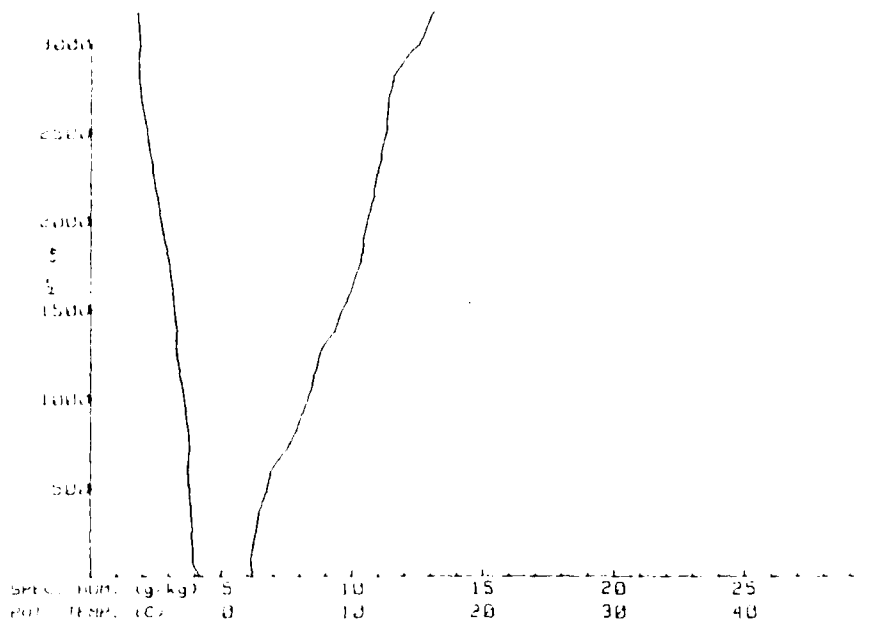


Figure 26. Plot for Radiosonde Sounding 15 July 1983, 2335 GMT



LOGHT104: 79.224 3.17E
 DATE TIME: 7 16 83 1147Z MIZEK53

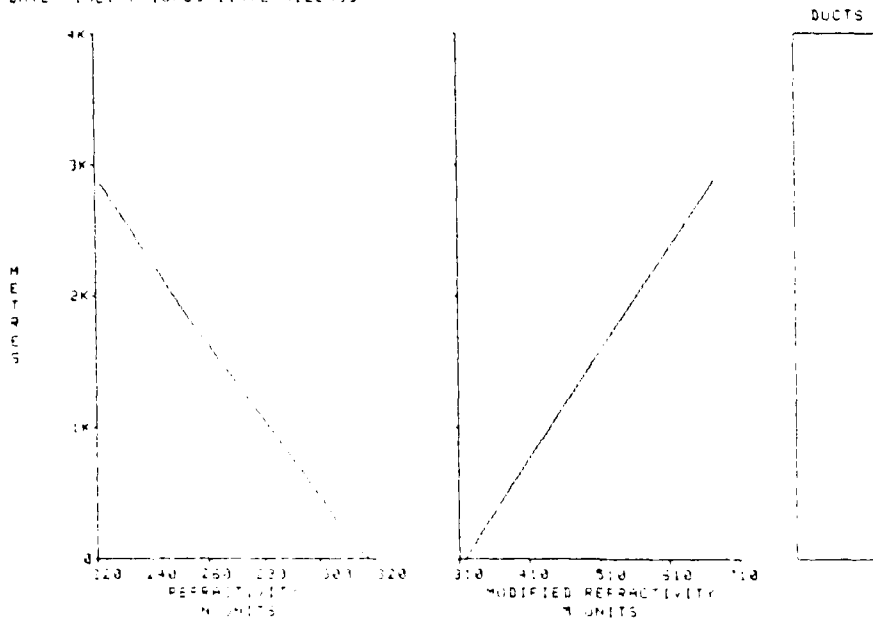


Figure 27. (a) Q and - Plot for Radiosonde Sounding 16 July 1983, 1147 GMT. (b) IREPS Output for 16 July 1983, 1147 GMT.

SOUNDING POSITIONS
 MIZEX 1983
 27-29 JULY

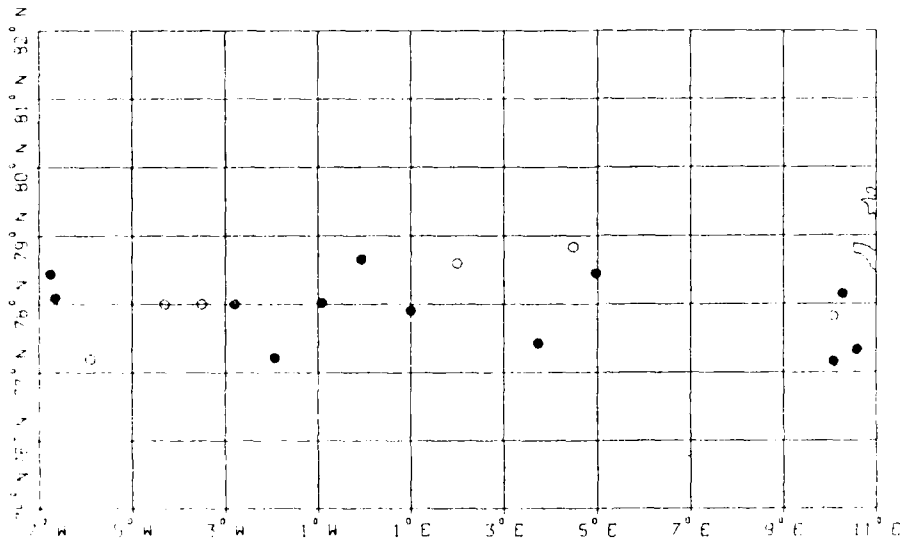


Figure 37. Radiosonde (o) and Spiral (·) Sounding Start Positions During 27-29 July 1983

subrefractive layer from 1254 m to 1309 m was due to a slight specific humidity increase.

On 29 July at 1329 GMT POLARBJORN's location was 77.18°N 5.87°W in transit from open to dense pack ice. Super-refractive layers probably extended from 23 m to 45 m, 873 m to 922 m, 948 m to 1024 m, and 1124 m to 1196 m (Fig. 55). A weak trapping layer extended from 922 m to 948 m ($\Delta M/\Delta z = -30.4 \text{ km}^{-1}$). A moist layer base at 1244 m caused subrefractive conditions. The following aircraft measurements were obtained on 29 July. At 1157 GMT (77.33°N 10.58°E) IREPS indicated subrefraction from 21 m to 27 m and trapping ($\Delta M/\Delta z = -48.8 \text{ km}^{-1}$) from 27 m to 32 m (Fig. 52). This may be the same layer as the super-refractive layer from 23 m to 45 m at 1329 GMT some 522 km eastward. The 1244 GMT (77.1°N 7.42°E) propagation conditions summary show normal refraction conditions up to 700 mb (Fig. 53). At 1309 GMT (77.43°N 03.73°E) a weak trapping layer ($\Delta M/\Delta z = -12.5 \text{ km}^{-1}$) extended from 128 m to 129 m (Fig. 54).

from 1220 m to 1264 m and subrefractive layers at 1846 m and 2050 m were caused by variations in specific humidity.

Aircraft measurements taken at 1148 GMT (77.92°N 01.00°E), 1416 GMT (78.67°N 00.07°W), and 1538 GMT (78.5°N 04.48°E) indicate that super-refractive and subrefractive conditions dominated throughout a substantial region of the MIZ (Figs. 42, 44, 45). The surface pressure measured aboard POLARBJORN increased from 1017.6 mb at 0000 GMT to 1020.3 mb at 1200 GMT and steadily decreased to 1003.5 mb on 30 July 0000 GMT.

The 28 July 1331 GMT radiosonde sounding was located at 78°N 3.5°E over the dense pack ice (Fig. 46). The trapping layer at 1183 m was probably somewhere closer to the stratocumulus top at about 820 m due to humidity sensor wetting. By 1737 GMT POLARBJORN's position was 78°N 4.32°W in dense pack ice. The moist mixed layer from 200 m to 950 m was probably a stratocumulus or stratus layer (Fig. 51). A super-refractive layer extended from about 950 m to 1043 m. Based on aircraft measurements for 1456 GMT (78.03°N 00.92°W) a trapping layer was predicted from 867 m to 926 m (Fig. 47). The IREPS output for 1550 GMT (78.05°N 02.78°W) shows a super-refractive layer from 40 m to 47 m and a trapping layer from 936 m to 996 m (Fig. 48). By 1621 GMT (78.08°N 06.67°W) the trapping layer extended from 1160 m to 1203 m (Fig. 49). At 1647 GMT trapping extended from 915 m to 972 m where super-refractive conditions extended to 1032 m (Fig. 50). A

77.82°N 07.42°E at 1244 GMT the inversion layer from 633 to 736 m in Fig. 53 was both warmer and more moist than the layer below ($\Delta T = 2.3^\circ\text{C}$ and $\Delta Q = 1.2 \text{ g/kg}$). The 1157 GMT sounding at 77.33°N 10.57°E (Fig. 52) shows a subsidence inversion extending from 910 m to 1063 m ($\Delta T = 1.5^\circ\text{C}$ and $\Delta Q = -0.64 \text{ g/kg}$). The visual and infrared satellite pictures from 29 July 0420 GMT show that the 1157 GMT sounding may have been to the east of an occluded front (Figs. 41,42). The 1244 GMT sounding may reflect the effect of the relatively uniform altostratus cloud layer overlying the colder, less moist atmospheric boundary layer.

b. Refraction Conditions

Radiosonde soundings and aircraft spiral soundings for the period 27 July through 29 July allows reconstruction of the spatial extent and temporal variability of the atmospheric refraction conditions.

On 27 July the 1404 GMT radiosonde sounding at 78.57°N 1.96°E over open water shows the presence of a cloud layer, identified by POLARBJORN as stratocumulus, from 30 m to 420 m. A trapping layer was predicted from 575 m to 618 m ($\Delta M/\Delta z = -289 \text{ km}^{-1}$). The lapse rates in Fig. 43 indicate that strong subsidence suppressed a well-mixed layer. Because the relative humidity never exceeds 98% and due to the instability of the atmospheric boundary layer the warm, moist layer from 420 m to 575 m can not be attributed to humidity sensor wetting. The weak trapping layer ($\Delta M/\Delta z = -18 \text{ km}^{-1}$)

3. Case 3: 27-29 July 1983

a. Synoptic and Mesoscale Features

This case pertains to a period when a significant high pressure system over the MIZ was weakened by an eastward moving frontal feature. Figures 42-55 appear at the end of this section in the order which the soundings were made. During 27-29 July POLARBJORN's position varied from 78.7°N 2.4°E in the open water to 77.0°N 5.7°W within the dense pack ice (Fig. 37). Surface winds were from the southeast (on-ice) at 4 m/s to 5.5 m/s. A synoptic scale anticyclone extended from Spitsbergen southeast to Norway on 27 July when it began to migrate eastward (Figs. 37,40). The developing cyclone to the southeast did not enter the MIZ but did establish a cold front about 10° south of the MIZEX area.

Coincident with a surface pressure decrease from 1020 mb on 27 July 1404 GMT to 1013 mb on 28 July 1331 GMT was an increase in mixed layer height from 420 m to 820 m. In the 27 July 1404 GMT sounding stratocumulus was observed in the mixed layer from 420 m to the top of the nonsaturated stable layer at 30 m (Fig. 43). The sounding was over open water. On 28 July 1331 GMT ice coverage was 6/8 to 7/8 (dense pack ice) and the stable surface layer extended to 120 m. Stratocumulus formed above the surface layer and extended to 820 m (Fig. 46).

Of interest is a comparison of two strikingly different aircraft soundings made on 29 July. Starting at



Figure 36. Infrared DMSP Picture at 17 July 1983, 1932 GMT. Grids Are from 10°W to 10°E with POLARBJORN's Location Marked by Black Dot.



Figure 35. Visual DMSP Picture at 17 July 1983, 1932 GMT. Grids Are from 10°W to 10°E with POLARBJORN's Position Marked by Black Dot.



Figure 34. Infrared DMSP Picture at 16 July 1983, 1953 GMT. Grids Are from 10°W to 10°E with POLARBJORN's Position Marked by Black Dot.

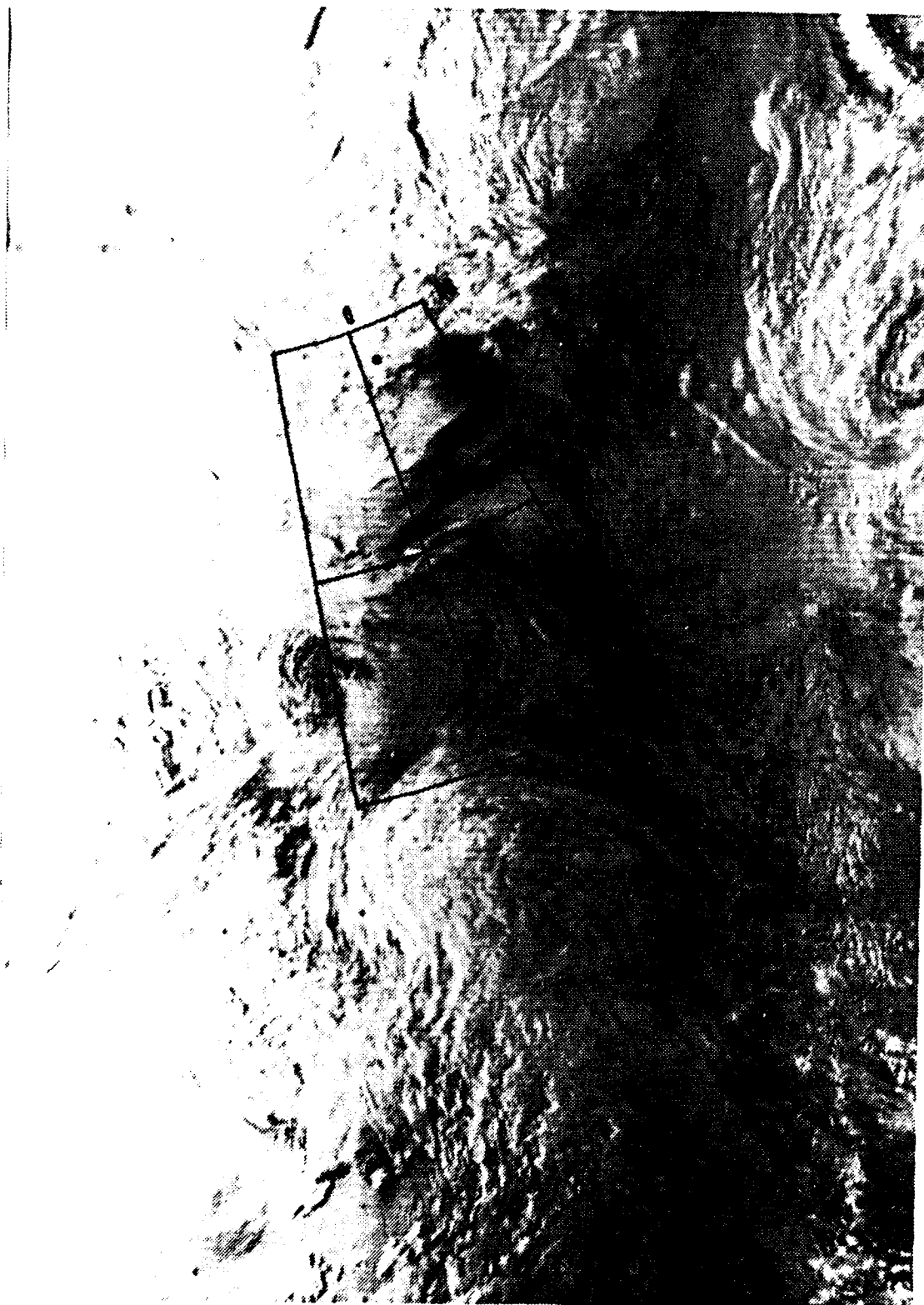


Figure 33. Visual DMSP Picture at 16 July 1983, 1953 GMT. Grid is from 10°W to 10°E with PLARBJORN's Position Marked by Black Dot.



Figure 32. Visual DMSP Picture at 15 July 1983, 2014 GMT. Grid is from 10°W to 10°E with POLARBJORN's Position Marked by Black Dot.

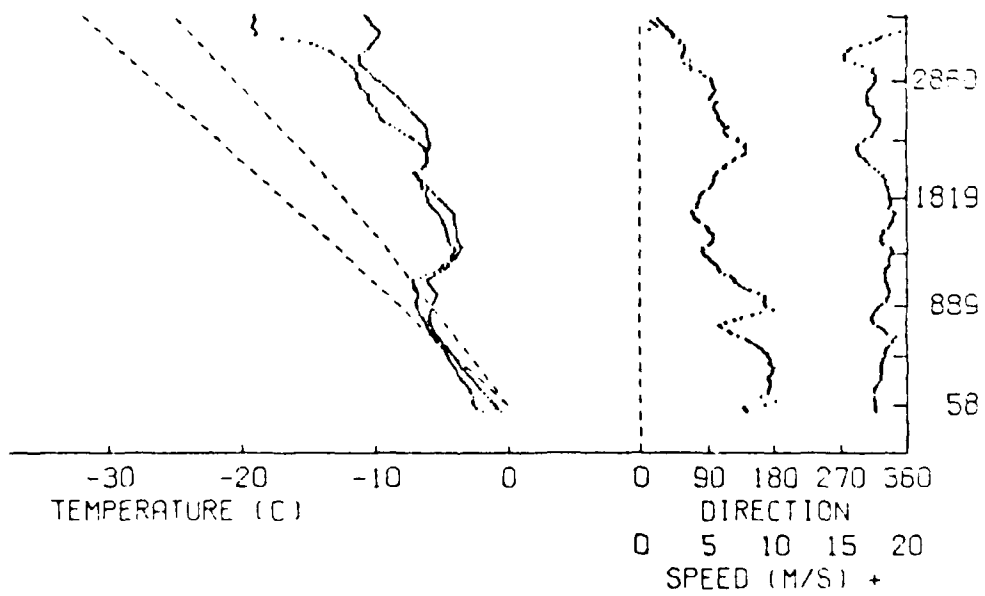
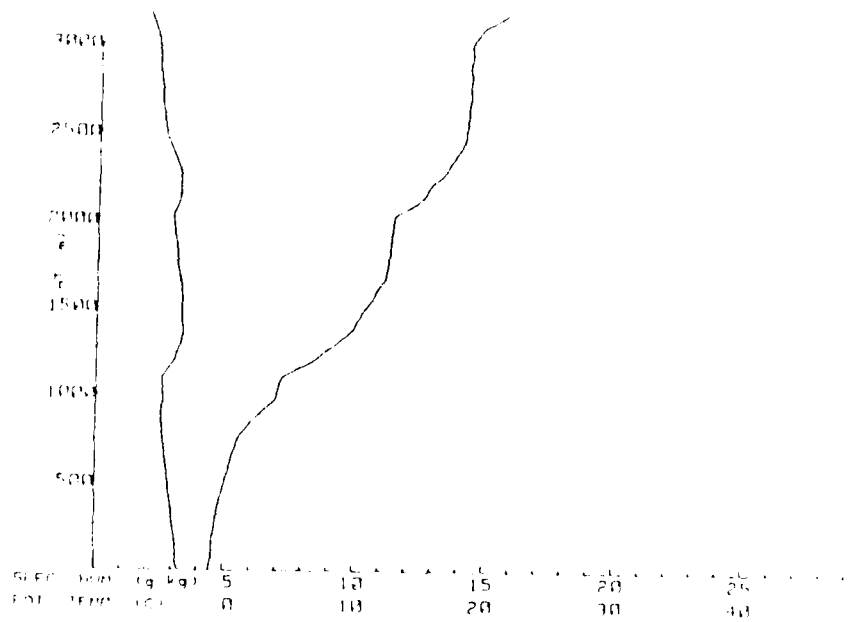


Figure 31. T and T_d Plot for 17 July 1983, 2331 GMT



LOCATION: 19.75N 100E MIZE+83
 DATE TIME: 7 17 83 2331Z US9

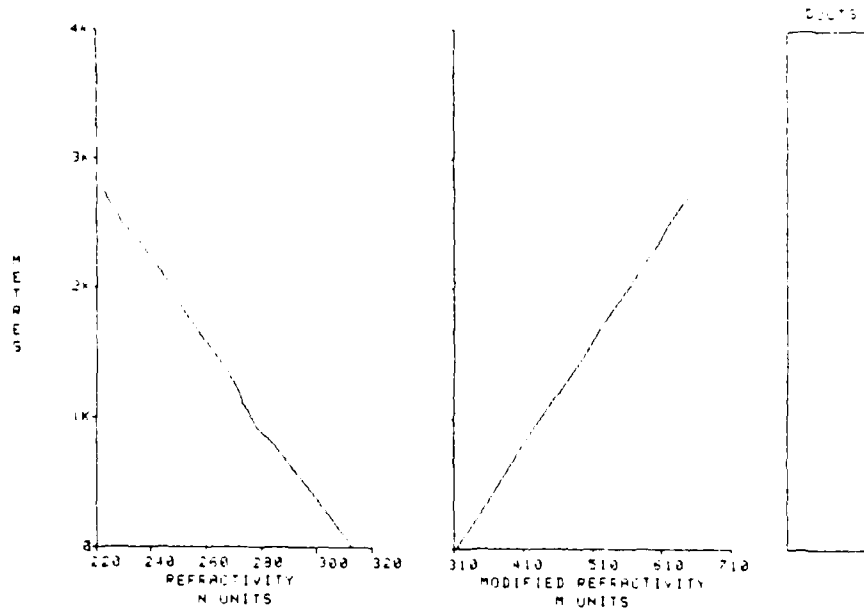


Figure 30. (a) Q and θ Plot for Radiosonde Sounding 17 July 1983, 2331 GMT. (b) IREPS Output for 17 July 1983, 2331 GMT.

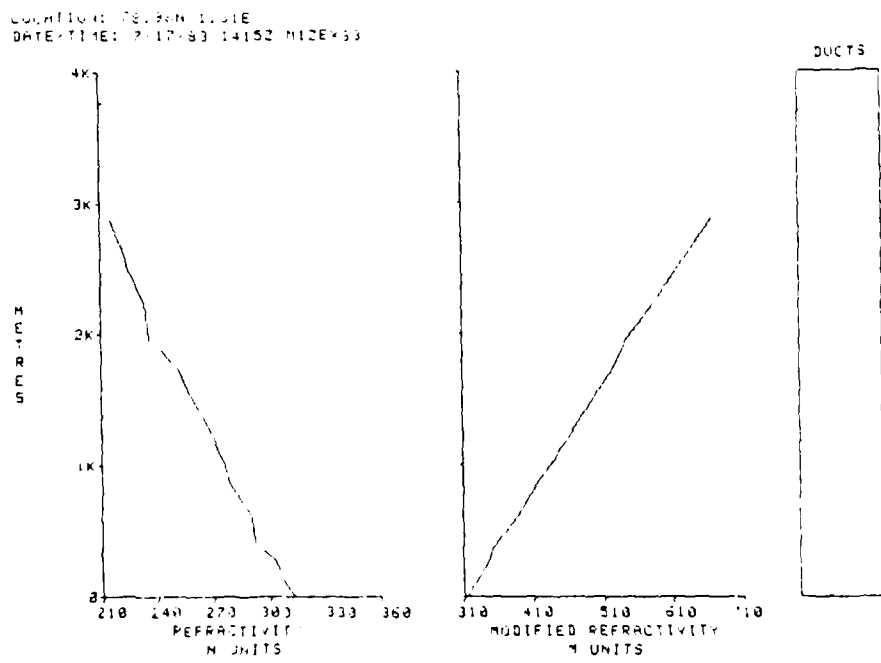
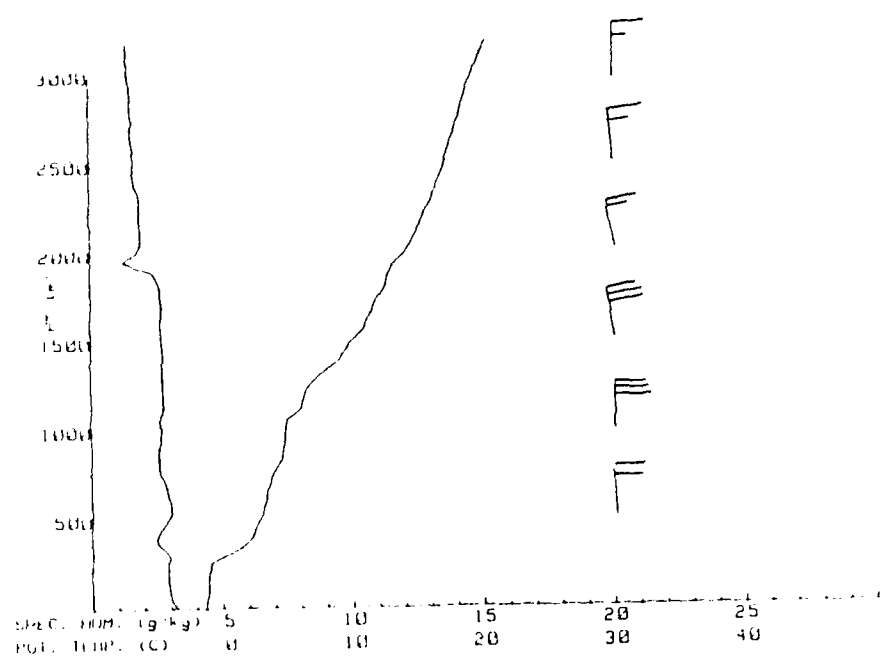
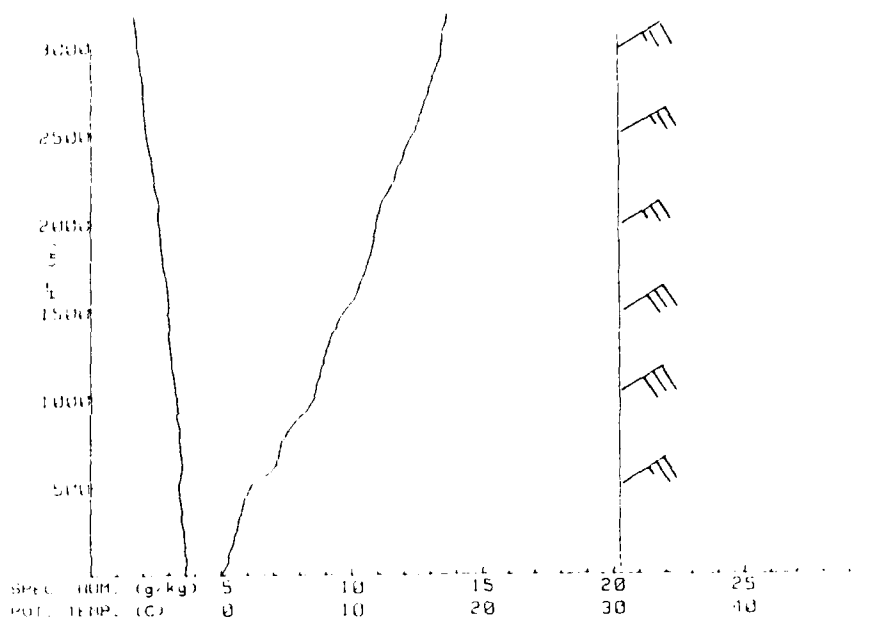


Figure 29. (a) Q and θ Plot for Radiosonde Soundings for 17 July 1983, 1415 GMT with Wind Barbs in Knots. (b) IREPS Output for 17 July 1983, 1415 GMT.



LOCATION: 79.3N 01.5E
 DATE TIME: 7/16/83 1734Z MIZE/83

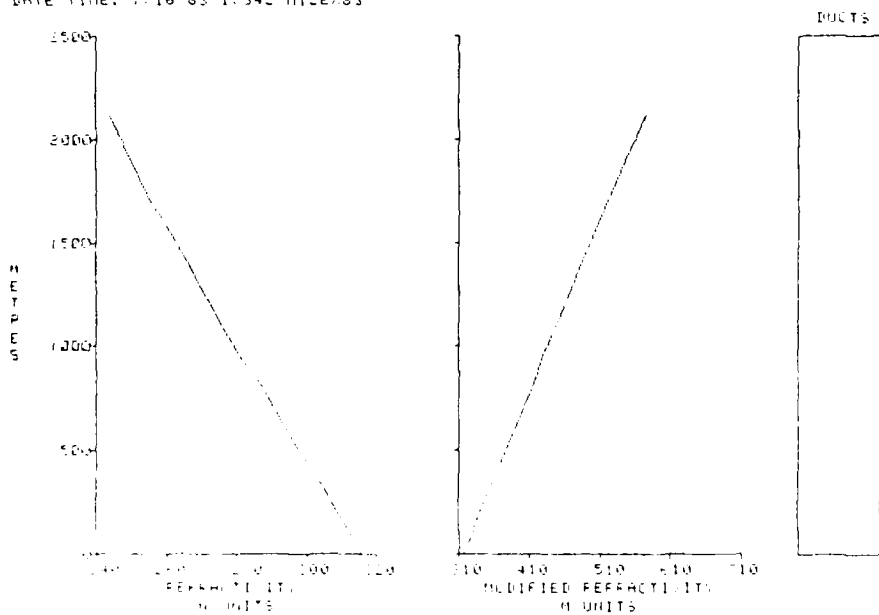
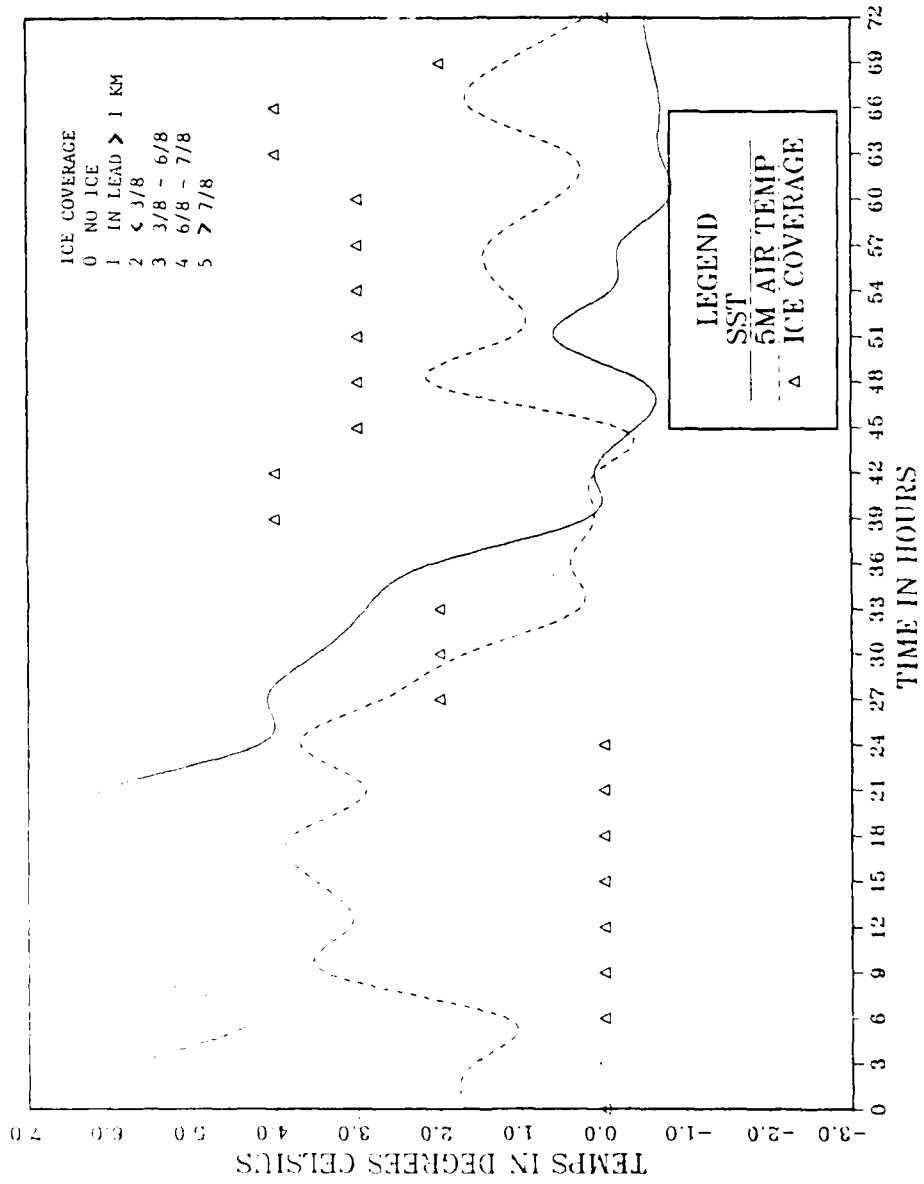


Figure 28. (a) Q and θ Plot for Radiosonde Sounding 16 July 1983, 1734 GMT with Wind Barbs in Knots. (b) IREPS Output for 16 July 1983, 1734 GMT.

MIZEX83 DATA



27-29 JULY 1983

Figure 38. Ice Coverage, 5 m Air Temperature and Sea Surface Temperature for 27-29 July 1983

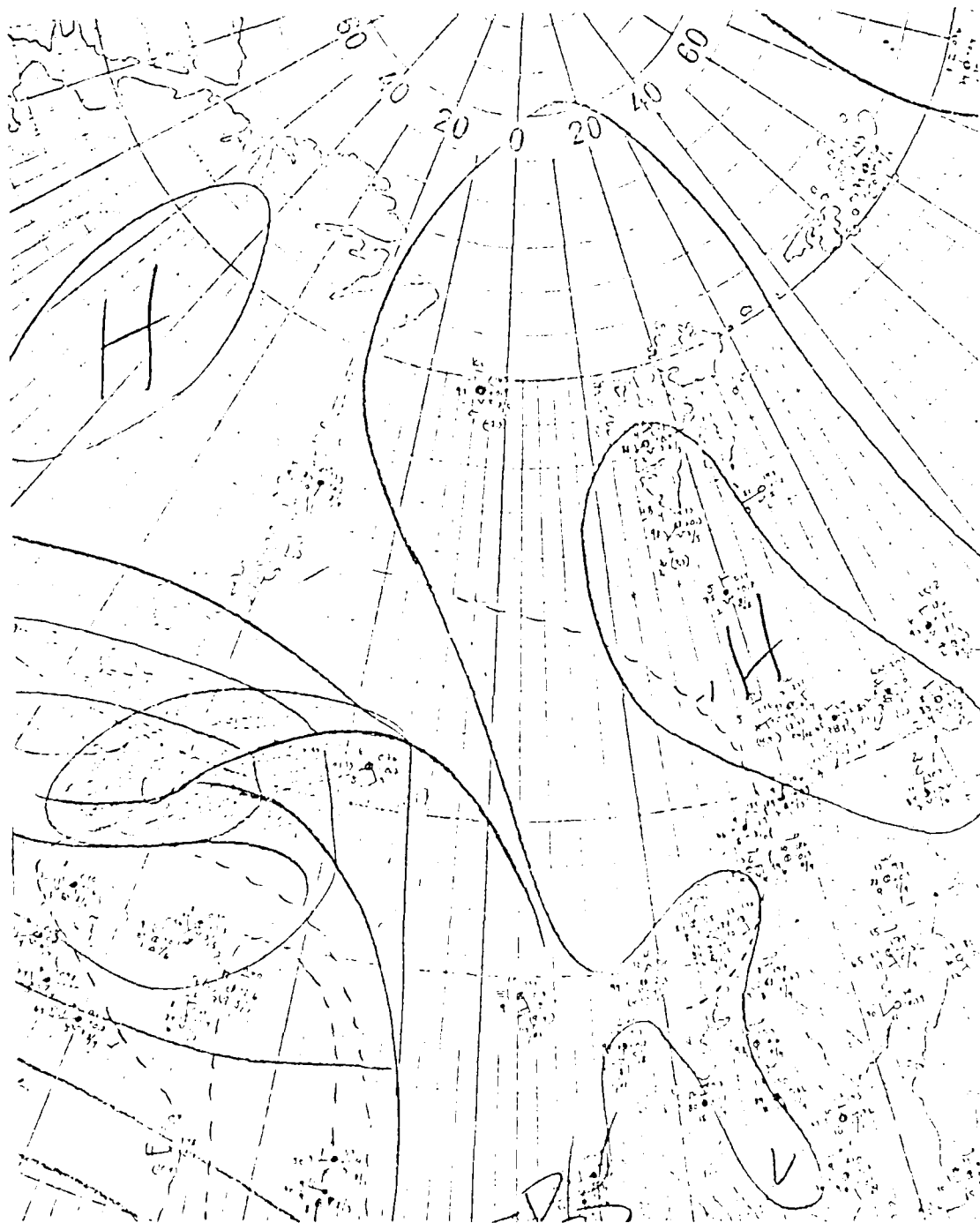


Figure 39. Surface Pressure Analysis for 26 July
1983, 0300 GMT

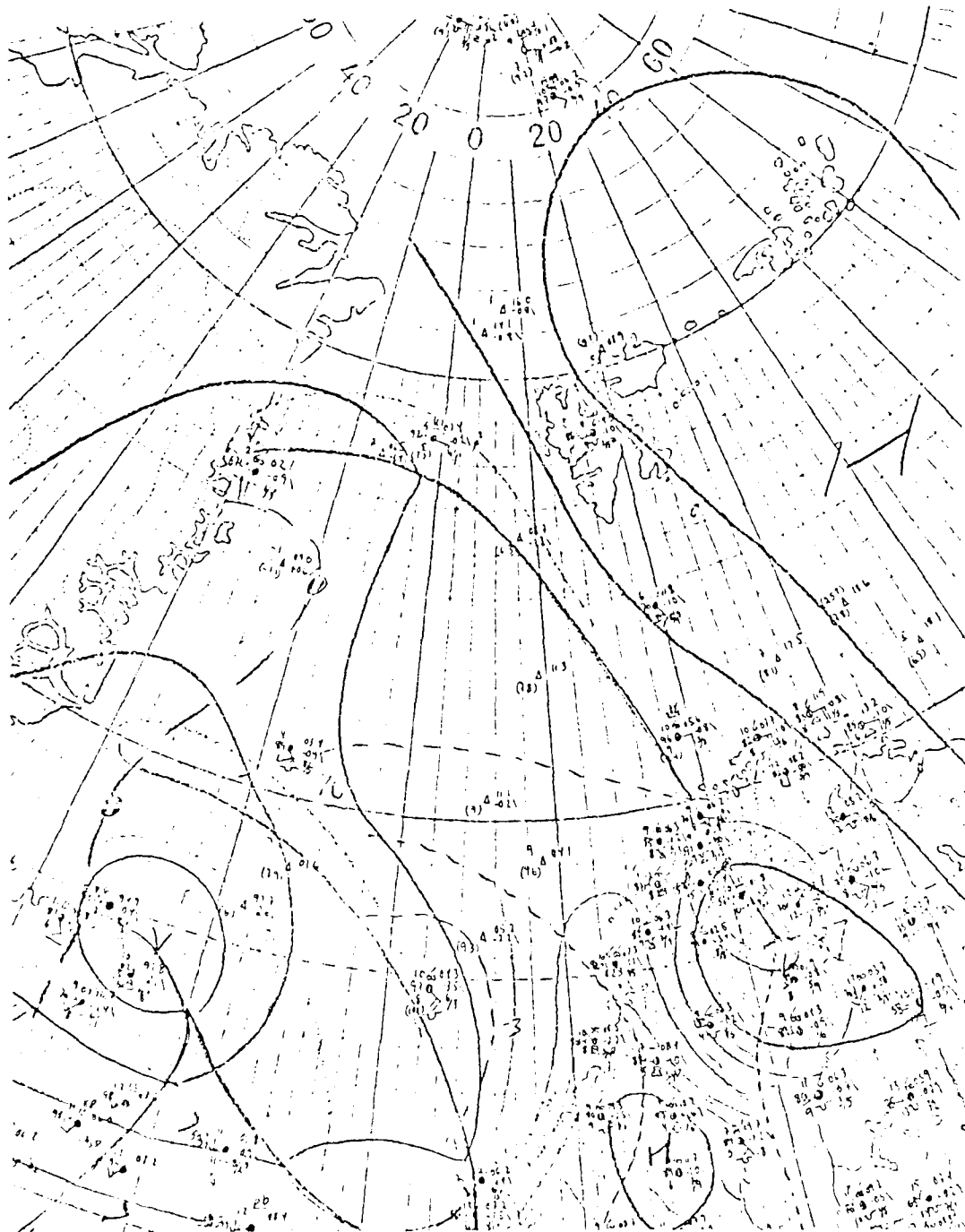


Figure 40. Surface Pressure Analysis for 27 July 1983, 0300 GMT

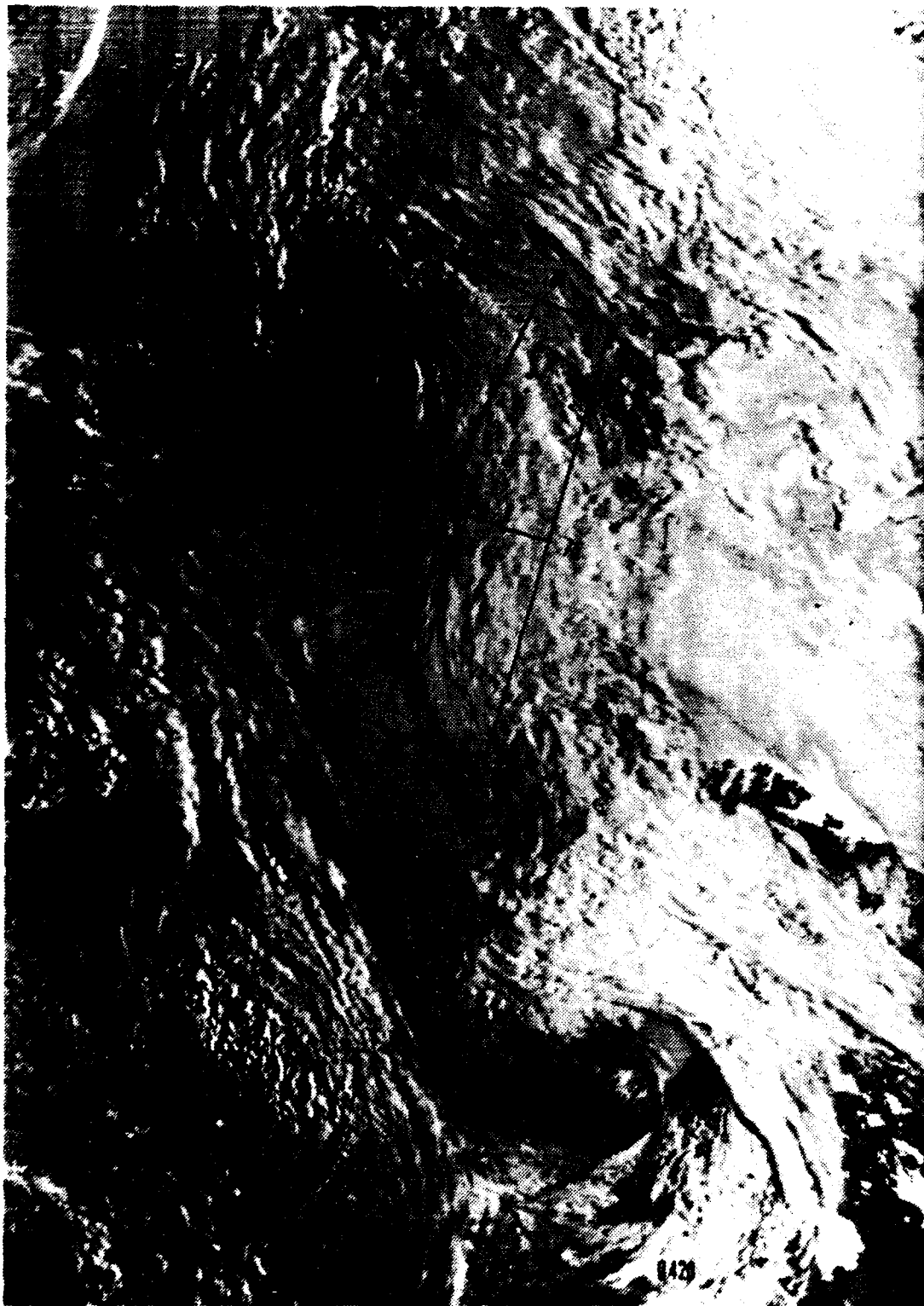
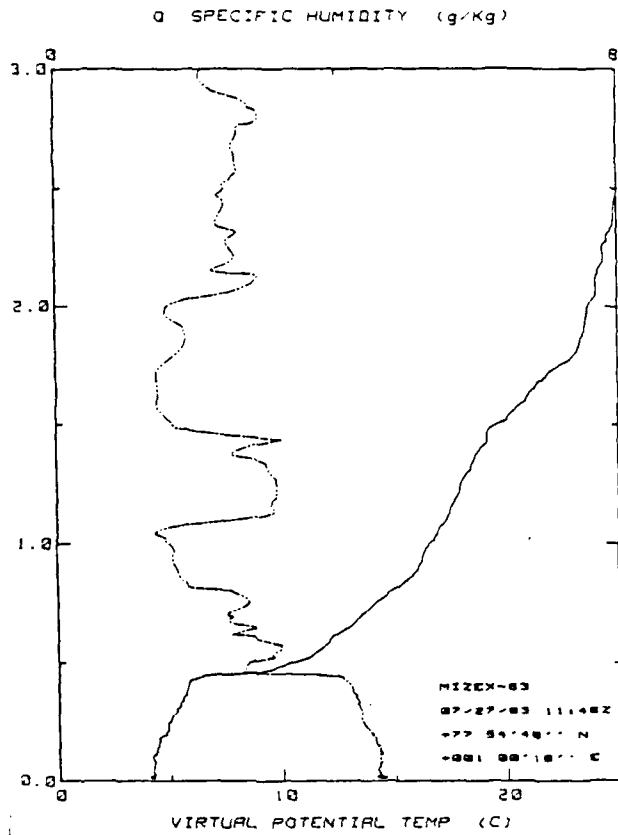


Figure 41a. Visual Picture at 29 July 1983, 0420 GMT.
Grids Are from 10°W to 10°E with POLARBJORN's
Location Marked by Black Dot.



Figure 4lb. Infrared DMSF Picture at 29 July 1983, 0420 GMT. Grids Are from 10°W to 10°E with POLARBJORN's Location Marked by Black Dot.



LOCATION: 77 54 48N 001 00 18E
DATE/TIME: 1148Z MIZEX83 A/C

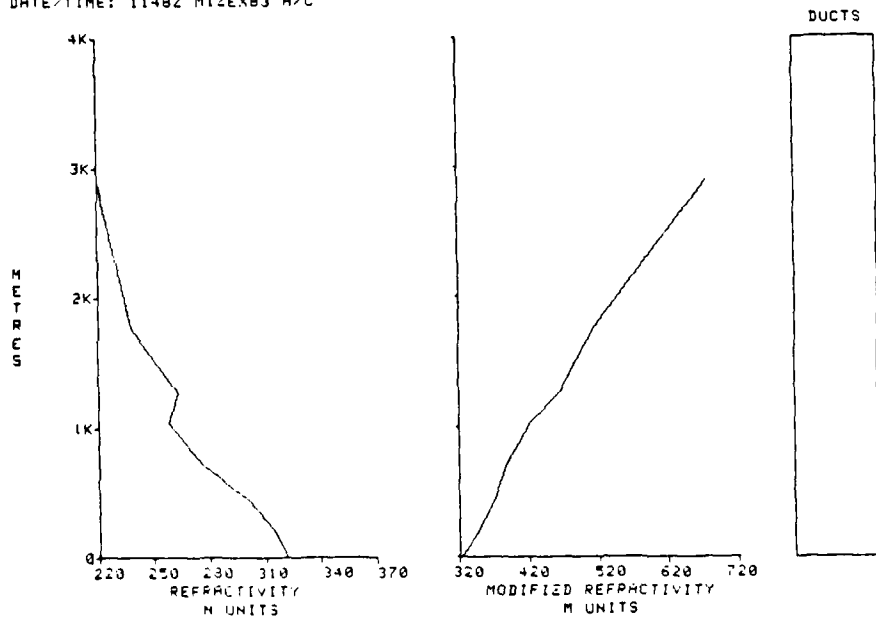
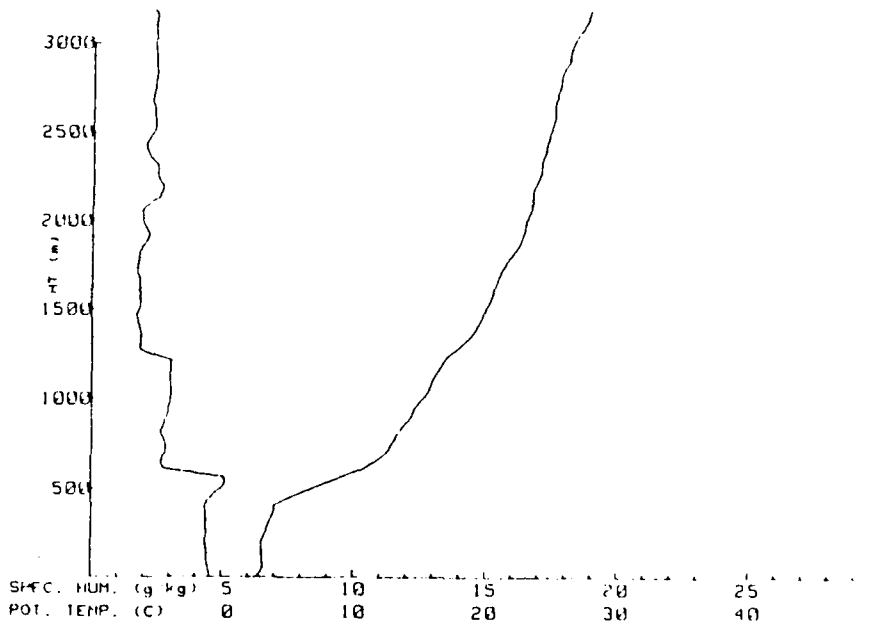


Figure 42. (a) Q and θ Plot for Spiral Sounding 27 July 1983, 1148 GMT. (b) IREPS Output for 27 July 1983, 1148 GMT.



LOCATION: 78.57N 1.96E MIZEX83
 DATE-TIME: 7-27-83 1404Z

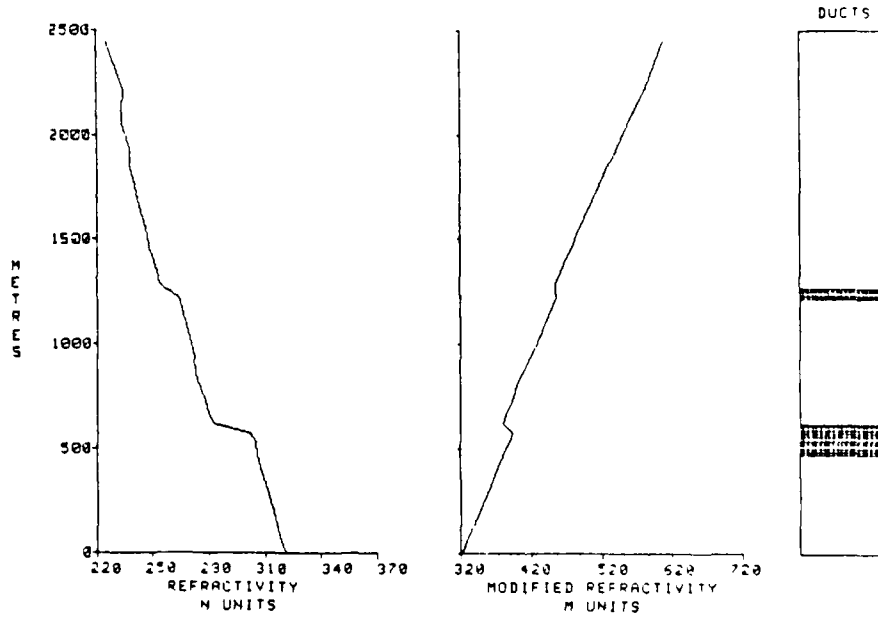
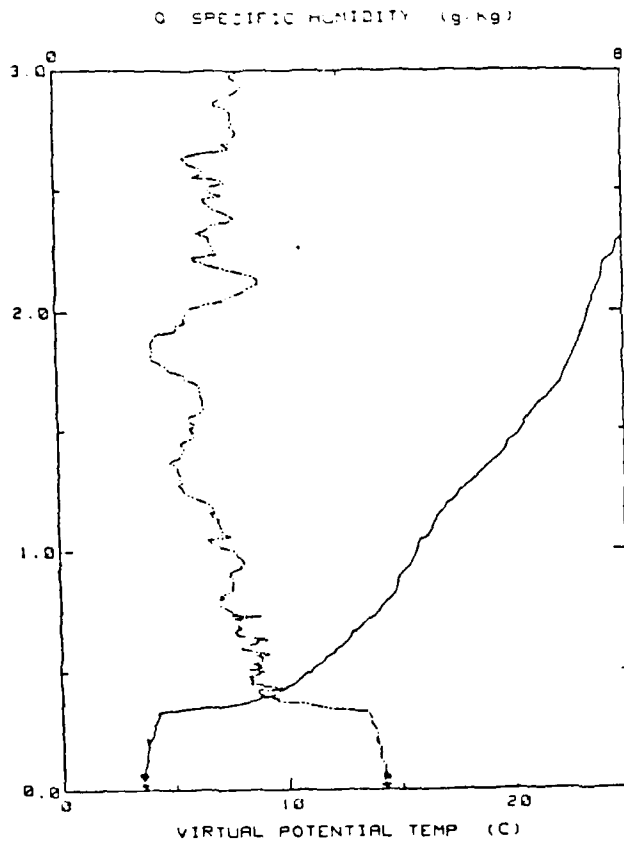


Figure 43. (a) Q and θ Plot for Radiosonde Soundings Made 27 July 1983, 1404 GMT. (b) IREPS Output for 27 July 1983, 1404 GMT.



LOCATION: 78 39 31N 000 03 36W
 DATE TIME: 1416Z 17JUL83 A/C

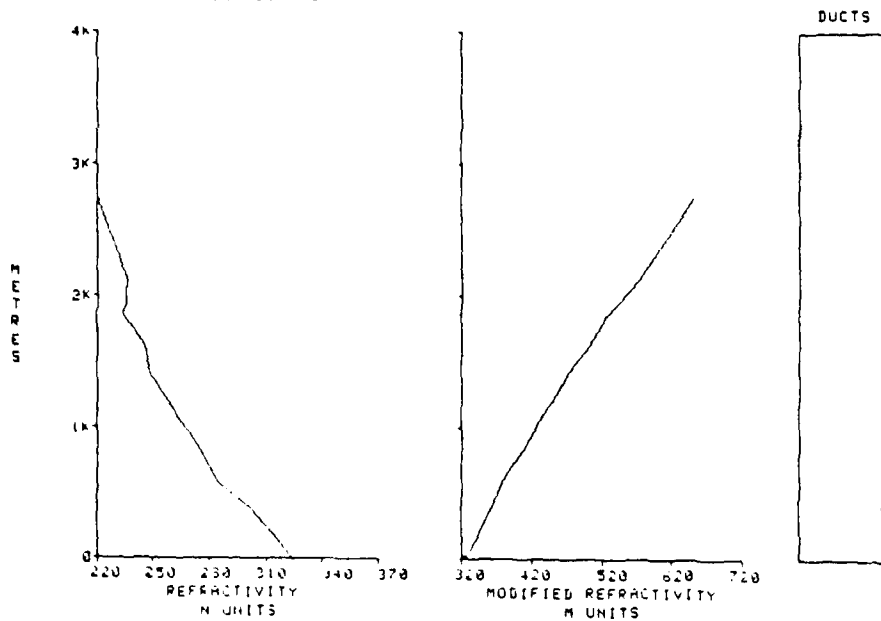
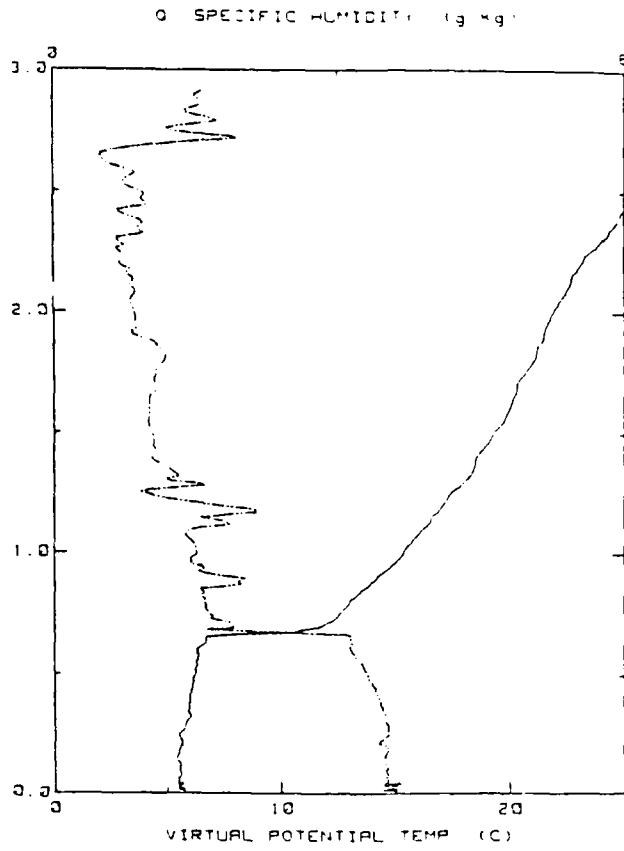


Figure 44. (a) Q and θ Plot for Radiosonde Sounding 27 July 1983, 1416 GMT. (b) IREPS Output for 27 July 1983, 1416 GMT.



LOCATION: 79 29 02N 094 28 41E
 DATE TIME: 7 27 83 1538Z MIZEX83 A

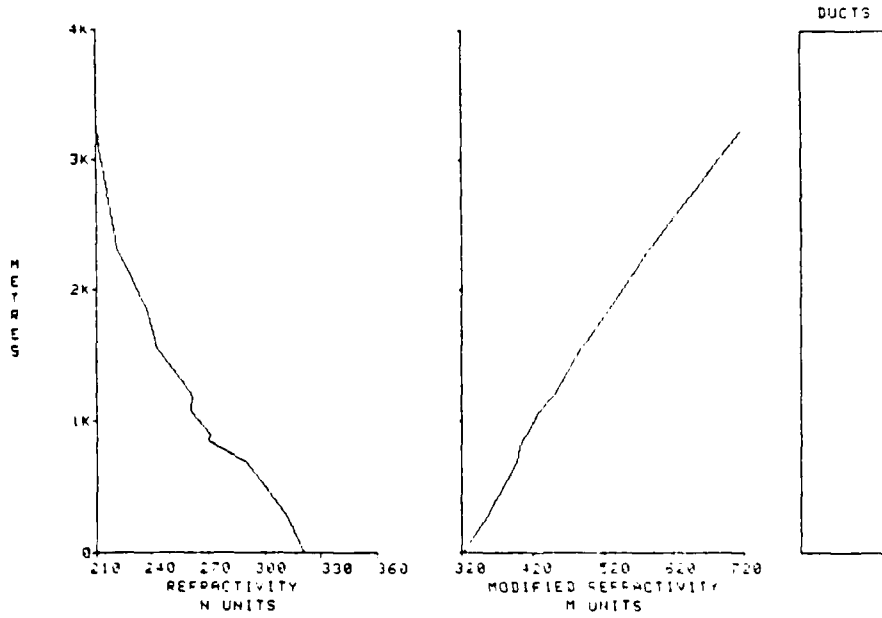
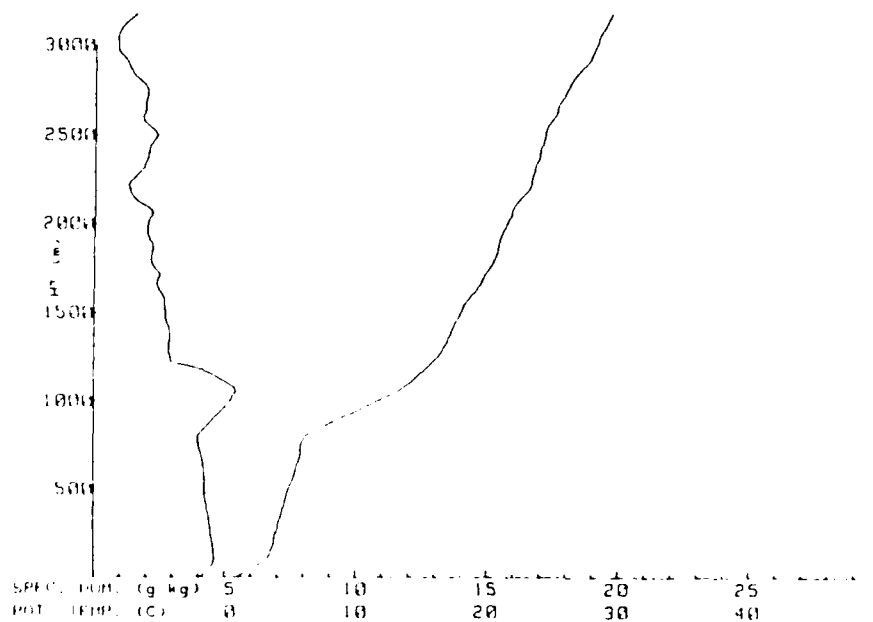


Figure 45. (a) Q and θ Plot for Radiosonde Sounding
 27 July 1983, 1538 GMT. (b) IREPS Output
 for 27 July 1983, 1538 GMT.



LOCATION: 77.39N -3.45E MIZEX83
 DATE/TIME: 7-28-83 1331Z

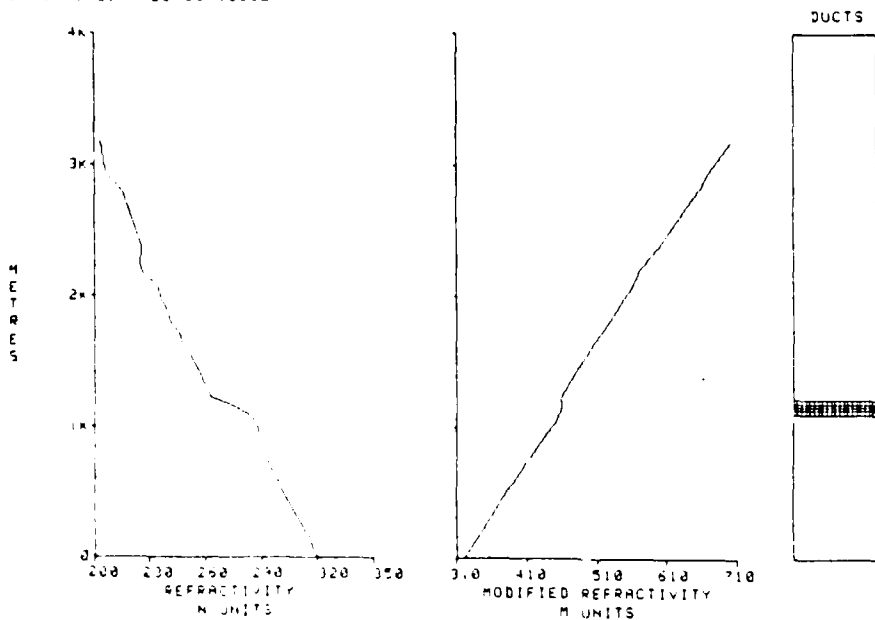
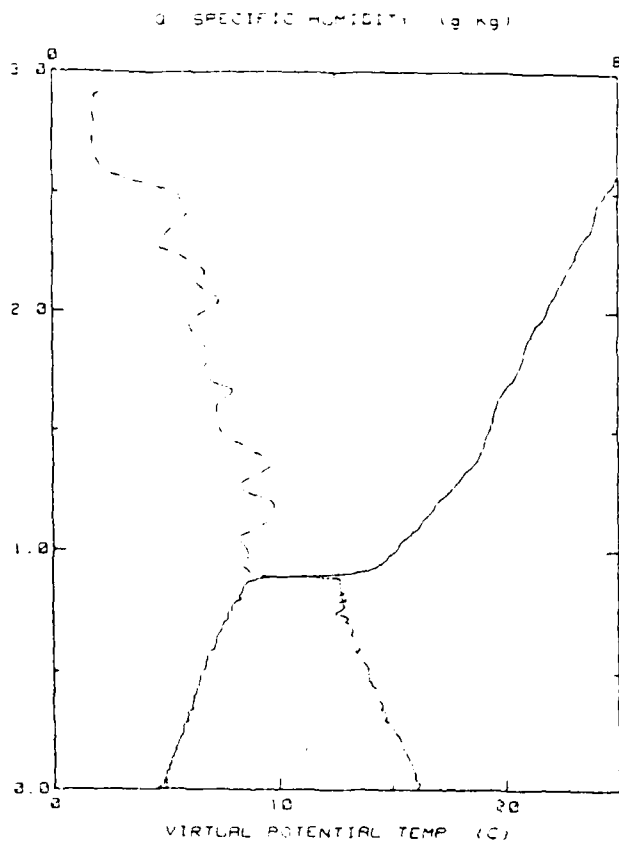


Figure 46. (a) Q and θ Plot for Spiral Sounding 28 July 1983, 1331 GMT. (b) IREPS Output for 28 July 1983, 1331 GMT.



LOCATION: 29 01 26N 000 54 53W
 DATE TIME: 1456Z 7-28-83 N12E43 AC

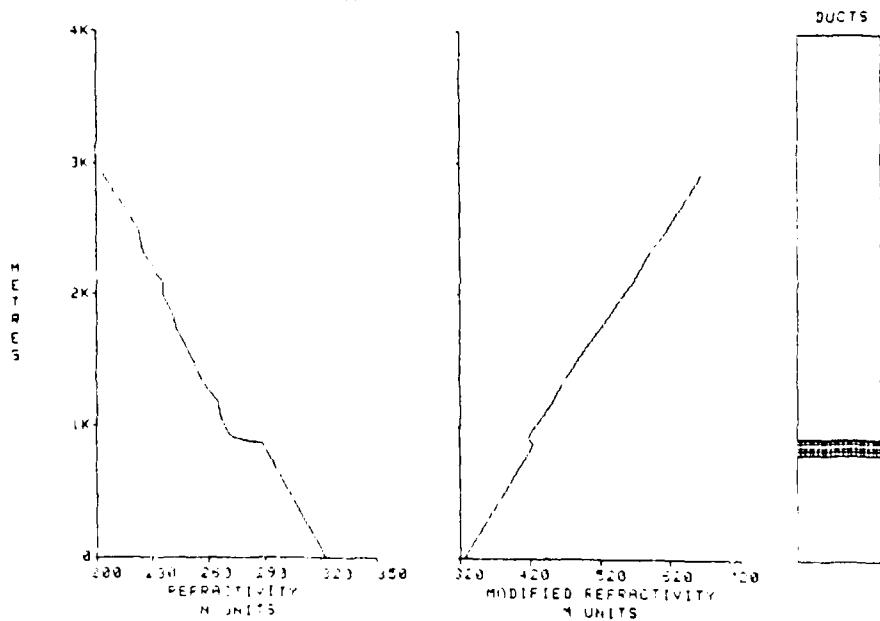
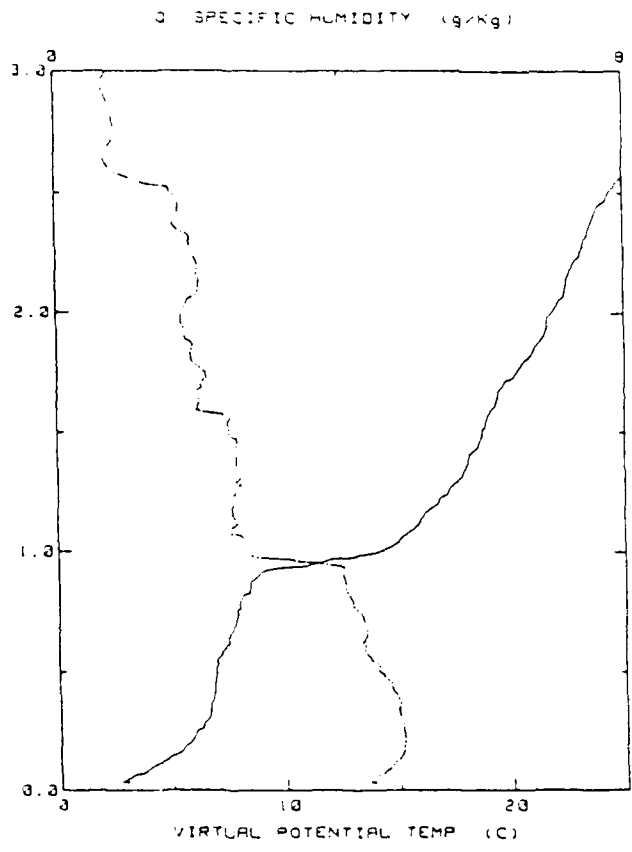


Figure 47. (a) Q and θ Plot for Spiral Sounding 28 July 1983, 1456 GMT. (b) IREPS Output for 28 July 1983, 1456 GMT.



LOCATION: 78 00 03N 002 47 18W
 DATE-TIME: 1050Z 7/28/83 MIZEX83 AC

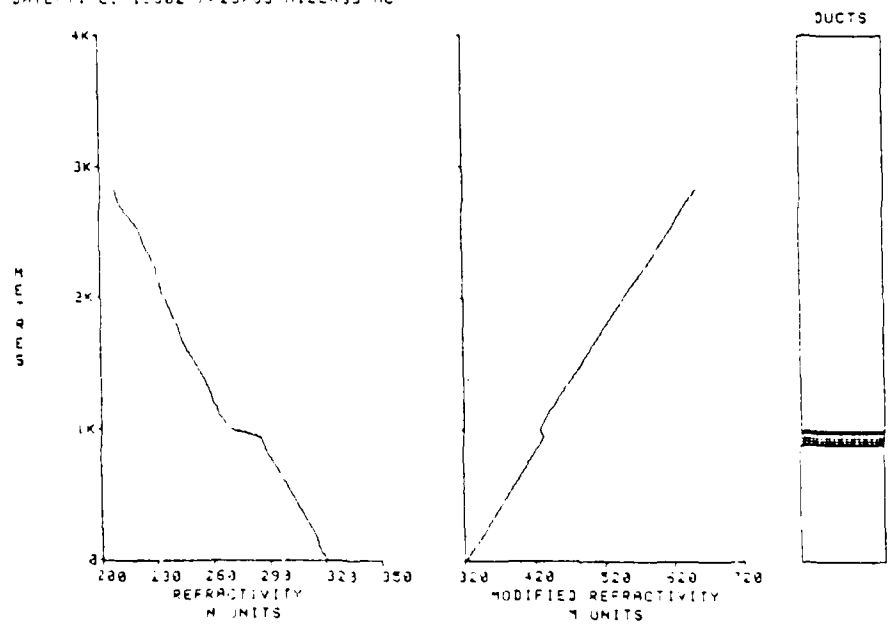
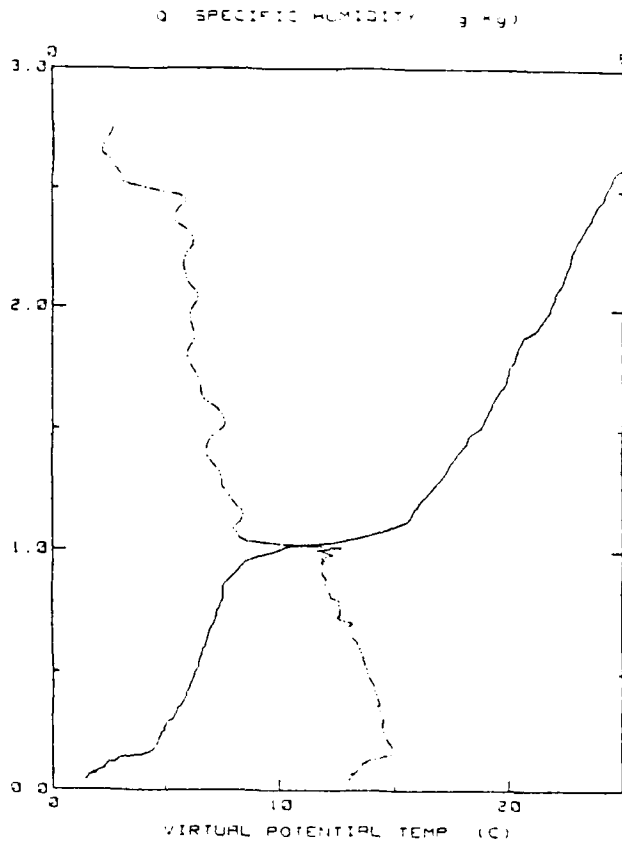


Figure 48. (a) Q and θ Plots for Spiral Sounding 28 July 1983, 1550 GMT. (b) IREPS Output for 28 July 1983, 1550 GMT.



LOCATION: 78 05 12N 006 39 57E
 DATE TIME: 1421Z 0728 83 MIDE-33 AC

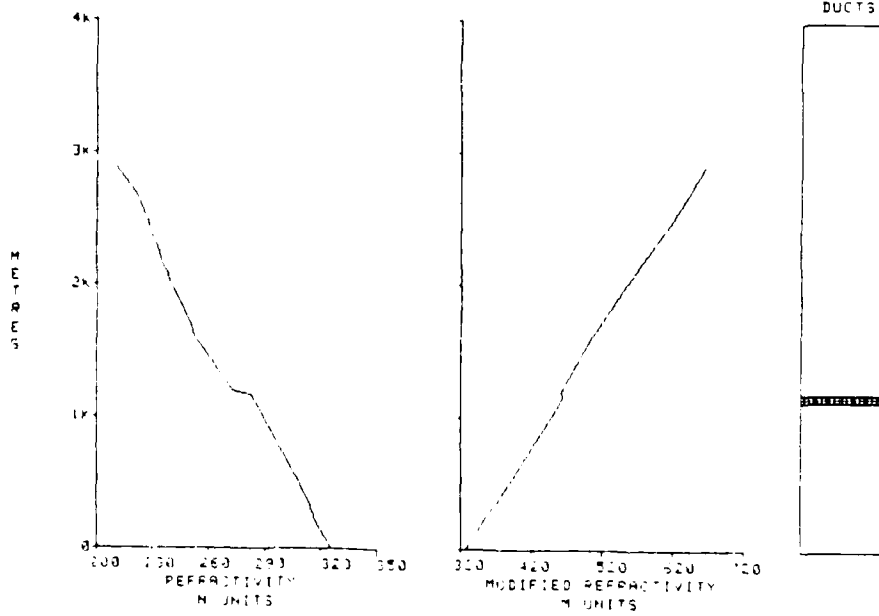
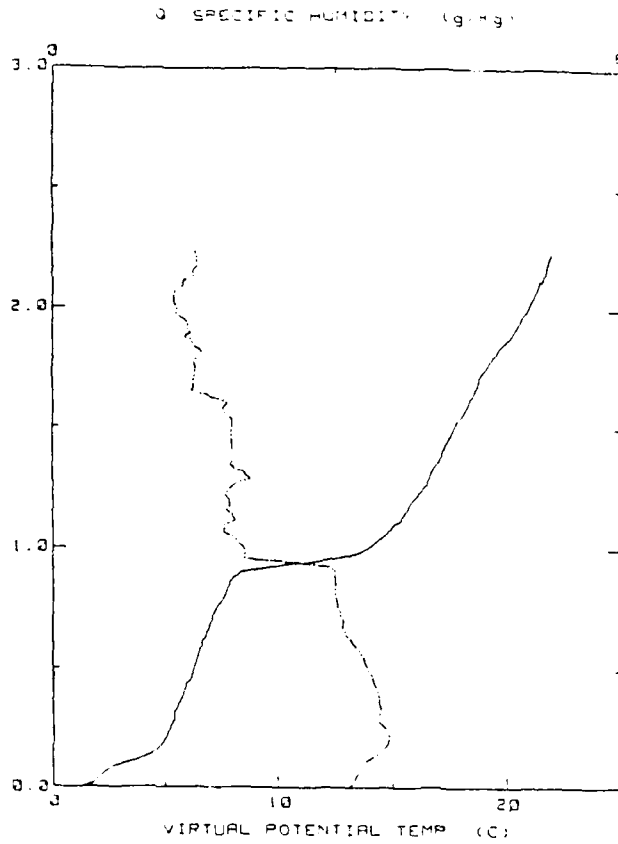


Figure 49. (a) Q and θ Plots for 28 July 1983, 1621 GMT. (b) IREPS Output for 28 July 1983, 1621 GMT.



LOCATION: 79 20 16N 006 45 29E
 DATE TIME: 1647 28 03 MIDE-83 AC

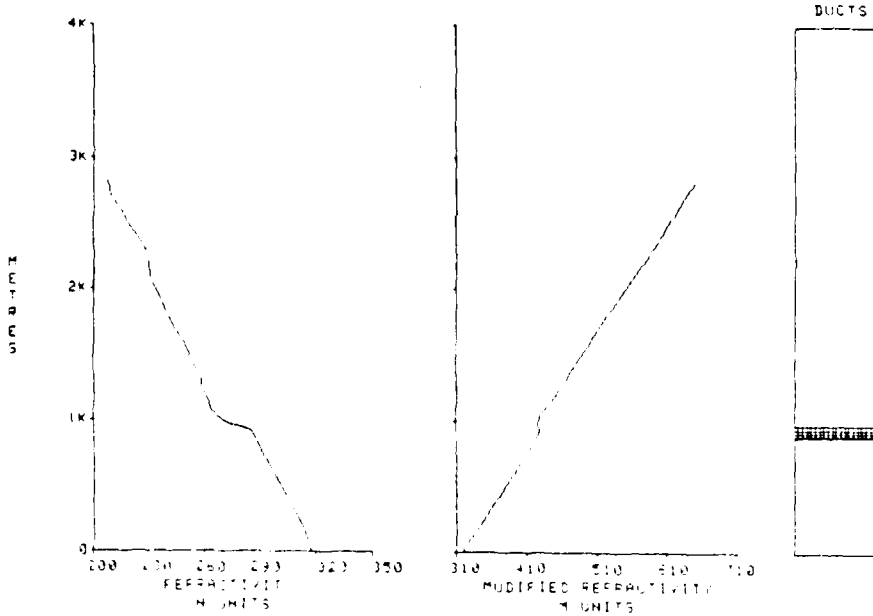
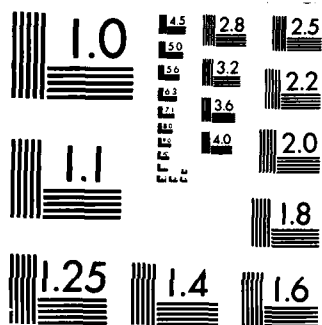
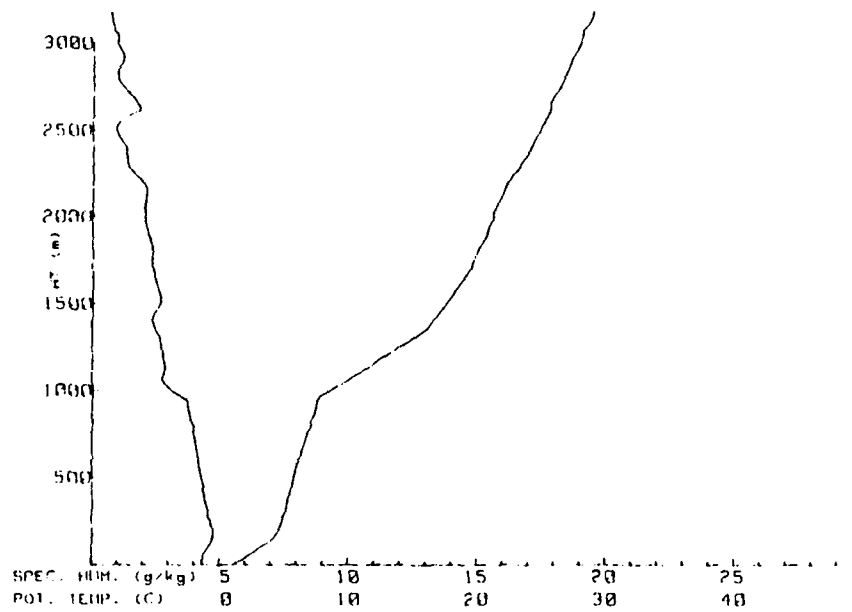


Figure 50. (a) Q and θ Plot for Spiral Sounding
 28 July 1983, 1647 GMT. (b) IREPS Output
 for 29 July 1983, 1647 GMT.



MICROCOPY RESOLUTION TEST CHART
NATIONAL BUREAU OF STANDARDS-1963-A



LOCATION: 77.99N -4.32E MIZEX83
 DATE/TIME: 7/28/83 1737Z

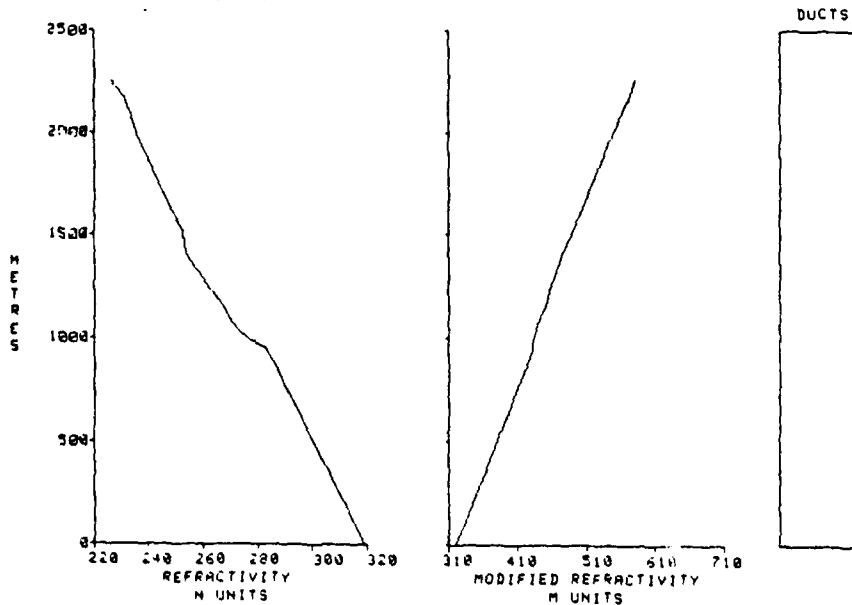
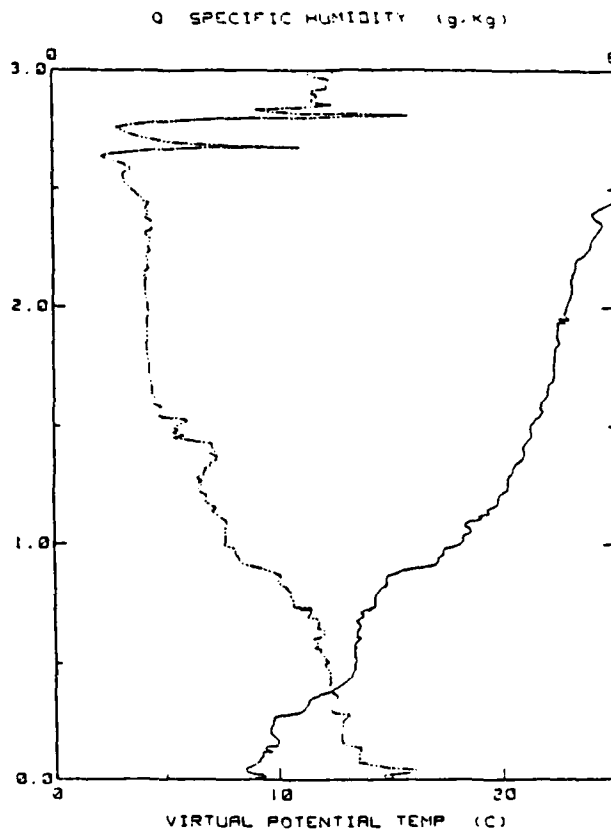


Figure 51. (a) Q and θ Plot for Spiral Sounding 28 July 1983, 1737 GMT. (b) IREPS Output for 29 July 1983, 1737 GMT.



LOCATION: 77 19 48N 010 34 31E
 DATE-TIME: 1157Z 7/29/83 MIZEN33 AC

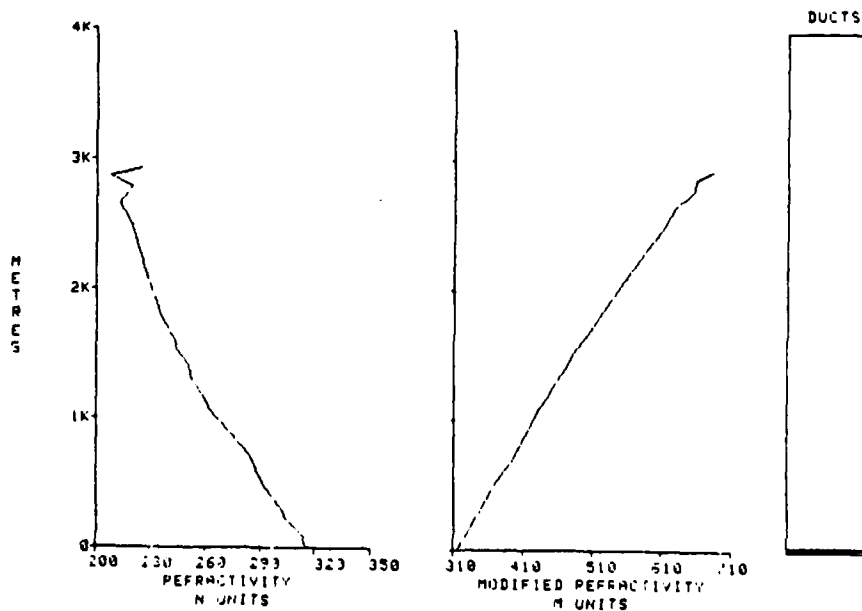
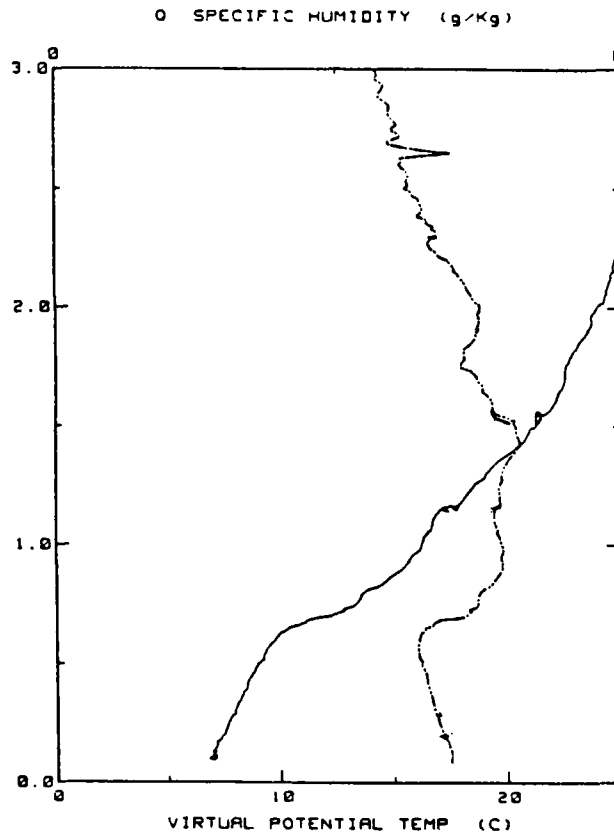


Figure 52. (a) Q and θ Plot for Spiral Sounding 29 July 1983, 1157 GMT. (b) IREPS Output for 29 July 1983, 1157 GMT.



LOCATION: 77 49 00N 087 25 00E
 DATE TIME: 1244Z 7-29-83 NICEK33 AC

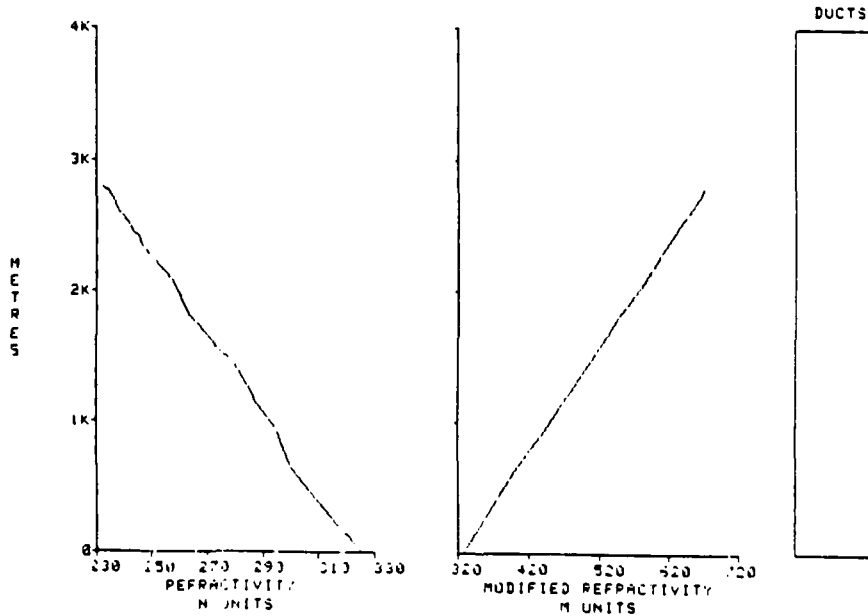
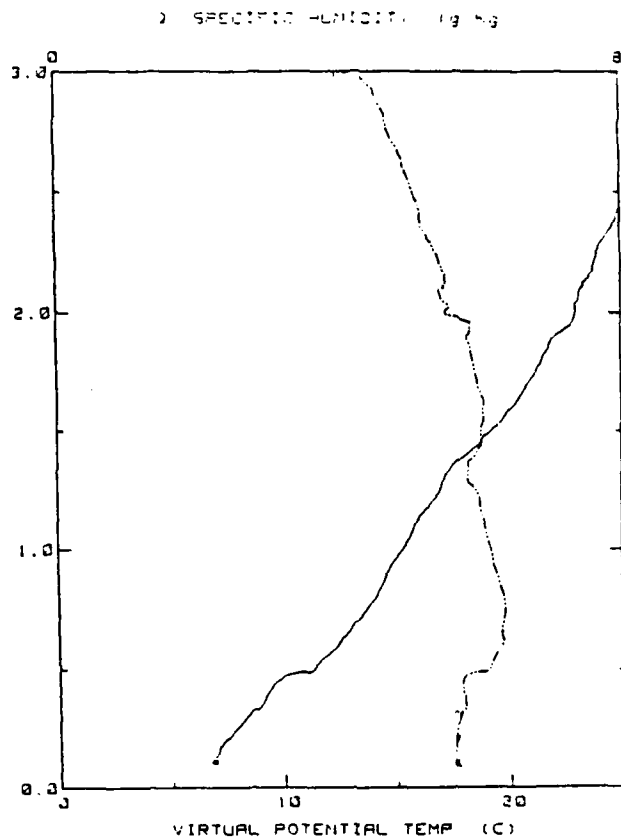


Figure 53. (a) Q and θ Plot for Spiral Sounding 29 July 1983, 1244 GMT. (b) IREPS Output for 29 July 1983, 1244 GMT.



LOCATION: 77 26 00N 003 44 00E
 DATE TIME: 11092 7 29 83 112453 AC

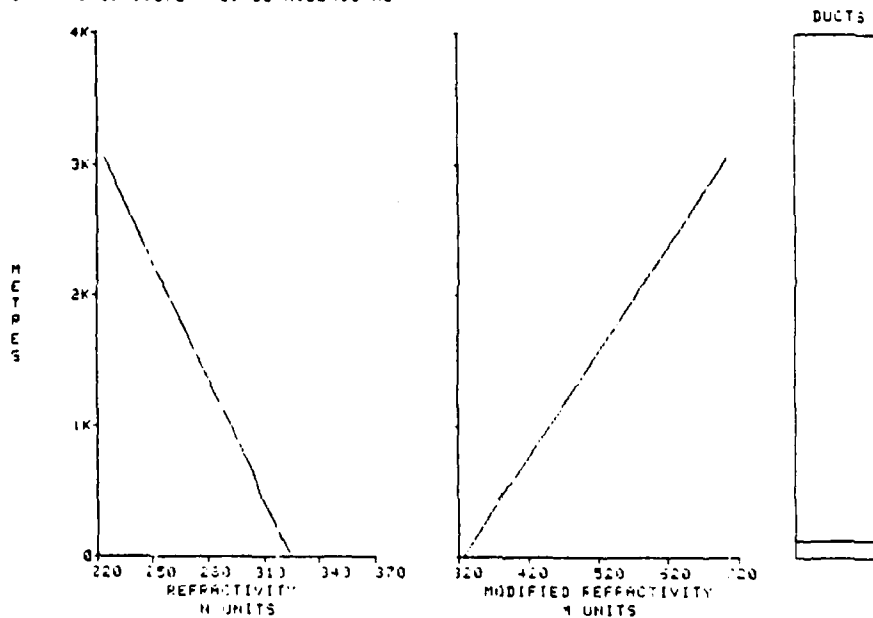
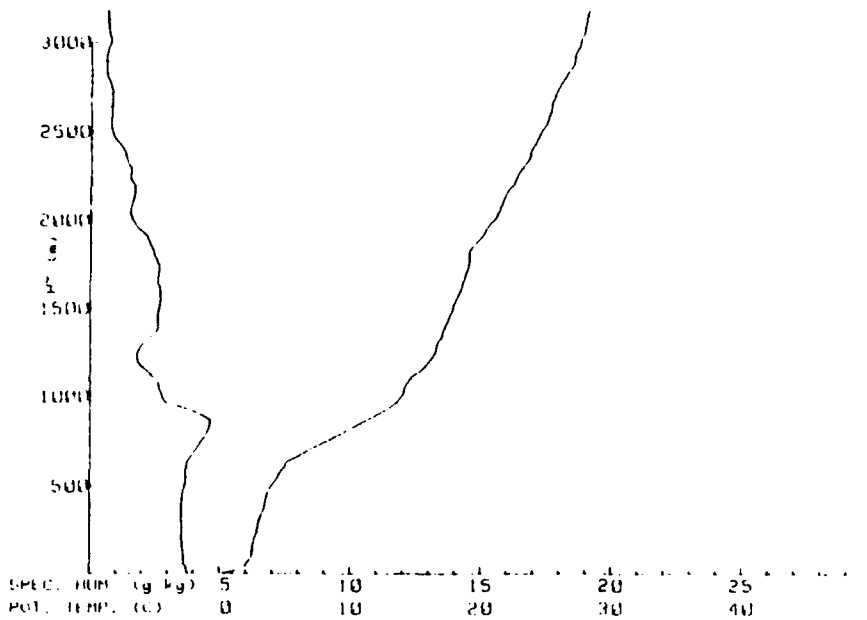


Figure 54. (a) Q and θ Plot for Spiral Sounding, 29 July 1983, 1309 GMT. (b) IREPS Output for 29 July 1983, 1309 GMT.



LOCATION: 77.19N -5.37E MIZEX83
 DATE/TIME: 7/29/83 1329Z

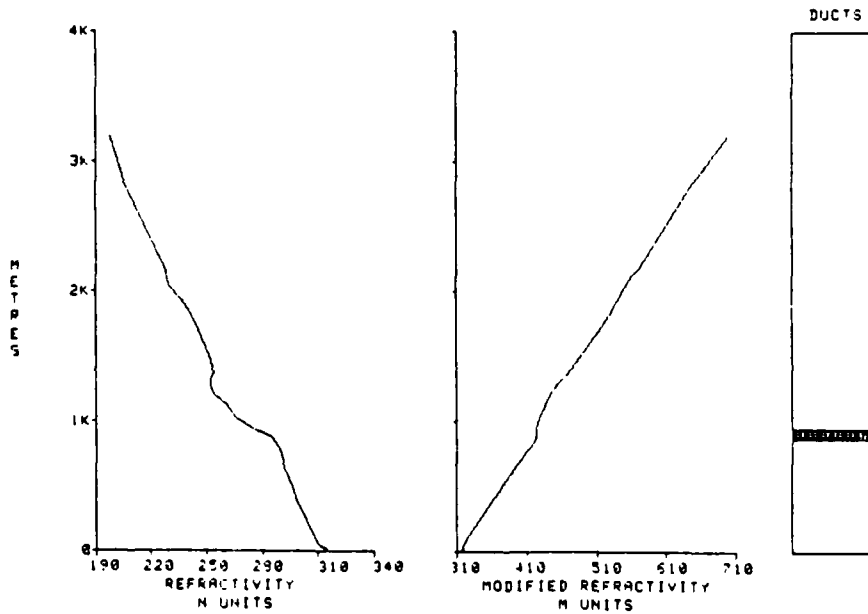


Figure 55. (a) Q and θ Plot for Radiosonde Soundings Made 29 July 1983, 1329 GMT. (b) IREPS Output for 29 July 1983, 1329 GMT.

IV. SUMMARIES OF CONDITIONS

A. SUMMARY OF SYNOPTIC FEATURES

Synoptic scale features include migratory high and low pressure systems of the lower troposphere with wavelengths of 1000 km to 2500 km. During MIZEX-83 synoptic scale cyclones formed south of the observation region, in the vicinity of Iceland, and traveled eastward with considerable regularity. Brown et al. (1984) indicate that the Greenland ice cap, at elevations of two to three kilometers, hinders these systems from moving into the MIZ. Although cyclonic vortexes did not enter the MIZEX-83 area, they affected airflow over the region. Surface airflow and moisture convergence to the south of the MIZ became dominant forcing mechanisms for regional airflow in such cases.

The influence of anticyclonic systems on the MIZ is quite direct. Weak high pressure systems probably became stationary over Greenland due to cooling of the lower atmosphere by the extensive icefield. Spatial extents of these systems are uncertain because the only surface observations within the 1500 km between the two landmasses during MIZEX-83 were made by the two research vessels.

A well-developed, large-scale anticyclone appeared over Norway as shown on the 26 July 1500 GMT (Fig. 56) surface analysis, and moved northward until it became nearly stationary over Spitsbergen from 27 July 0600 GMT until 28 July 0900

GNT. It then moved eastward and dissipated by 30 July. The anticyclone was significant because of its dominance over regional forcing mechanisms. The surface wind during the anticyclonic period was from the southeast which is consistent with POLARBJORN's position in the southwestern quadrant of the anticyclone.

A warm front to the southeast of the MIZ weakened the intensity of the subsidence over the region. Refraction conditions varied from super-refractive to weak trapping. This observation is consistent with conclusions made by Helvey and Rosenthal (1983) for a midlatitude case. Along the warm front clouds and precipitation (drizzle) were common. The differing air masses interacted southwest of the MIZ. These conditions led to the inversion base and refraction layers weakening and lifting in the MIZ.

B. SUMMARY OF MESOSCALE FEATURES

1. Baroclinity and Stability

From the cases studied in this thesis, a striking feature of the MIZ is the horizontal variability in atmospheric and oceanic properties as one travels from the dense pack ice to open water. Based on POLARBJORN's observations from 27 July to 29 July horizontal SST differences of 4°C between dense pack ice and open water were typical. On 28 July the 1550 GMT spiral sounding was located only 0.6° east (67 km) of POLARBJORN's position at 1500 GMT in the dense pack ice. Shipboard observations show a SST of 0.2°C, 5 m

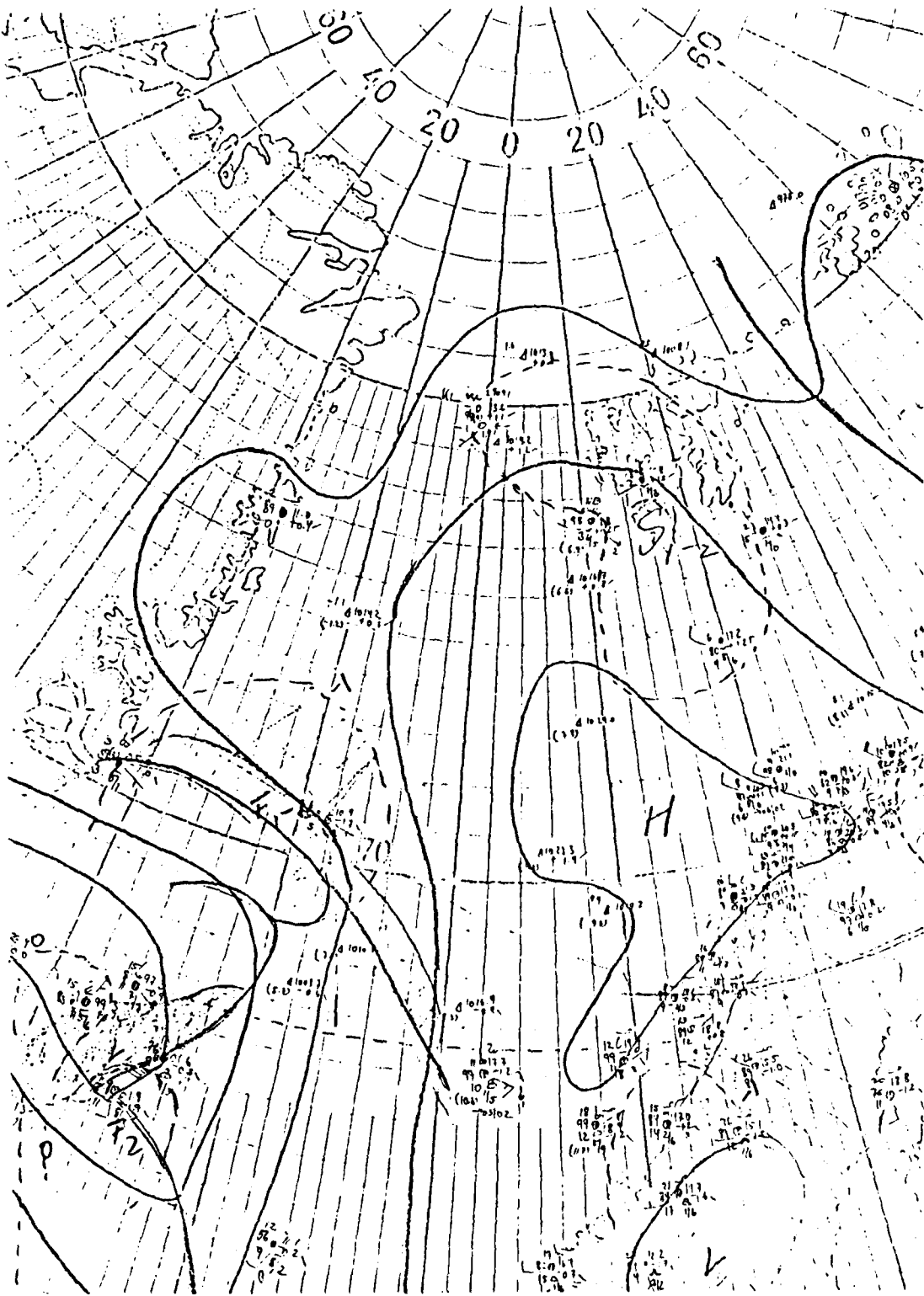


Figure 56. Surface Analysis for 26 July 1983, 1500 GMT

air temperature of 0.1°C , and wind from 100° at 5 m/s. The 1550 GMT air temperature at 36 m was 2.6°C . At 1456 GMT a spiral sounding 1.8° east (200 km) of the 1550 GMT sounding recorded the air temperature at 6 m over open water at 4.1°C . For measurements separated by only one hour the horizontal difference was 1.5°C over a distance of 200 km.

Horizontal sea-surface temperature gradients seem to be major contributors to mesoscale forcing due to cooling/heating of the atmospheric surface layer from below. The horizontal sea-ice surface temperature difference appears to cause significant baroclinic effects on the ABL over the MIZ. Despite this, however, the "land breeze" effect mentioned by Tucker (1984) does not seem to correlate with the southwesterly flow commonly observed during MIZEX-83. The significant horizontal temperature gradient may have caused a thermal wind, which is the vertical shear of the geostrophic components of the wind.

Considering some observed mesoscale features and the responsible thermodynamical processes it is seen that during POLARBJORN's drift phase from 27 June to 8 July surface wind directions were typically from the southwest. Relatively warm, moist maritime air was advected over the cold dense pack ice so that fog and stable surface layers tended to form. Turbulent mixing due to surface shear production of turbulent kinetic energy causes the surface layer to become less stably stratified.

The surface layer over the open water region of the MIZ was generally near-neutral when off-ice winds prevailed. Polar air flowing over the relatively warm water is heated from below and forced to rise due to convection. Above the surface layer the mixed layer is conditionally unstable. As the air rises in this case it cools and water vapor condenses to form clouds. Convective clouds during MIZEX-83 were confined to low and middle levels. Stratocumulus and altocumulus were most commonly observed. Above 700 mb conditions were generally stable as shown in Fig. 22 on 14 July 2022 GMT. There is no evidence in the satellite imagery of cumulus clouds with significant vertical development. Observed convective activity was limited to the mesoscale and was not coupled to synoptic scale cyclones as proposed by polar low CISK (conditional instability of the second kind) theory.

C. OCCURRENCE OF ELEVATED DUCTING

1. Factors Affecting the Inversion Base Height

a. Subsidence and Entrainment

Elevated ducts during MIZEX-83 varied in vertical extent because of the balancing effects of subsidence and entrainment. Subsidence of upper-tropospheric air appears to be an important mesoscale feature in the MIZ. Arctic air is cold and dry aloft but as it descends it warms due to adiabatic compression. Although subsidence alone has no effect on the mixed layer except to control its vertical extent, entrainment and cloud top cooling change the properties

of the mixed layer. Through interaction with the inversion layer by turbulence and radiative flux divergence the mixed layer becomes warmer and drier. Cloud-top cooling can decrease the warming effect of entrainment by cooling the layer. Stratus clouds form below the subsidence inversion when the moist air is cooled to its dew point temperature.

Entrainment of the inversion layer is dependent upon the surface layer and cloud-top-induced instability. Inversion wind shear and/or surface flux induced turbulence causes mixing of the warmer, drier inversion layer into the mixed layer below. Radiative flux divergence is typically strong at the top of the well-mixed layer. Cloud-top cooling leads to a decrease in the mixed layer mean temperature and an increase in the temperature jump at the inversion. As the top of the cloud cools it becomes more dense than the layer below and it overturns so that mixing in the cloud is enhanced. This mixing can contribute to mixing within the whole mixed layer.

b. Role of Atmospheric Boundary Layer Mixing
(Turbulence)

Previously, turbulence had been discussed in general terms because of the many uncertainties regarding the parameterization of surface roughness in the MIZ. Turbulence is the means of entrainment across the inversion base where trapping layers may form. A more detailed discussion of the topic is warranted. A general discussion will be followed by a more specific case study.

Bulk methods are possible with routine data for parameterizing surface layer stability. These methods are based on the Richardson number, R_i , defined as:

$$R_i = \frac{g}{\theta} \frac{\partial \bar{\theta} / \partial z}{(\partial \bar{u} / \partial z)^2}$$

Turbulence vanishes at the critical Richardson number, R_{cr} . For unstable conditions, R_i is nearly equal in magnitude to the layer height divided by the Monin-Obukhov length, Z/L ; defined as the height where the production of kinetic energy by wind shear instability balances the buoyant production of kinetic energy.

During MIZEX-83 wide ranges of stability conditions in the surface layer were observed. Using the following equation for the bulk Richardson number a comparison was made:

$$R_B = \frac{\frac{g}{\bar{T}_v} \left[\left(\frac{T_5 - T_{SST}}{5} \right) + 0.61 T_5 \left(\frac{Q_5 - Q_0}{5} \right) + .0098 \right]}{\left(\frac{U_5}{5} \right)^2}$$

where:

- θ is the potential temperature;
- \bar{T}_v is the mean layer virtual temperature, roughly equal to T_5 in degrees Kelvin;
- T_{SST} is the SST measured with a boom thermister in degrees C;
- T_5 is the 5 m air temperature in degrees C; and
- U_5 is the wind speed in m/s.

The observed variability in refraction conditions with time at relatively fixed locations would indicate that an equilibrium state was never reached. Because the MIZ is strongly baroclinic the IREPS prediction can not be extended horizontally. In some cases satellite imagery can be used to impose a certain degree of horizontal homogeneity but the vertical sounding should be made at the same time as the satellite picture. Therefore, the operational use of IREPS is very limited in the MIZ. The prediction is based on how the vertical temperature and moisture profiles were structured at the time of the sounding. By the time the IREPS output is available the atmospheric refraction conditions could be very different.

Recommended procedures for forecasting atmospheric refraction conditions in the MIZ are as follows:

- 1) Obtain vertical soundings up to 700 mb by radiosonde, dropsonde, or aircraft mounted instrumentation. The MIZEX-83 data indicates that the time interval between soundings should not exceed 12 hours. For increased accuracy a sounding should be made every six hours. Horizontal spacing between soundings should be small enough to account for SST variability and changes in the pack ice. Spacing should be at least 50 km in both meridional and zonal directions to detect major horizontal gradients. An aircraft could deploy radiosondes at each gridpoint within a relatively short period of time.

- 2) Determine the source and characteristics of the representative airflow. Satellite imagery can be used to locate

V. CONCLUSIONS AND RECOMMENDATIONS

The MIZ is a region of strong variability in all temporal and spatial scales. Although synoptic scale depressions did not directly affect the MIZEX-83 experimental area they did determine the airflow through the region. Subsidence affected the MIZ on both the mesoscale and the synoptic scale. When synoptic disturbances did not affect the MIZ the characteristic flow was southwesterly with relatively higher surface pressures due to subsidence.

The dominant mesoscale feature was the oceanic forcing of the surface layer. During cold air advection over the open water the surface layer was nearly neutral. Increased turbulence due to mechanical (wind mixing) and buoyant (shallow convection) turbulent kinetic energy generation would explain the observed normal refraction conditions. Over the dense pack ice during warm air advection the surface layer was cooled from below. Surface flux divergence was probably minimal in the stable surface layer so that elevated ducts were relatively persistent.

The ABL was rarely well defined because a well mixed boundary layer is dependent upon unstable conditions which were rarely observed during MIZEX-83. The surface layer stability can be defined by the shipboard measured SST and 5 m air temperature difference. The upper sub-layers of the ABL may have been in varying stages of transition from stable to neutral conditions or vice versa.

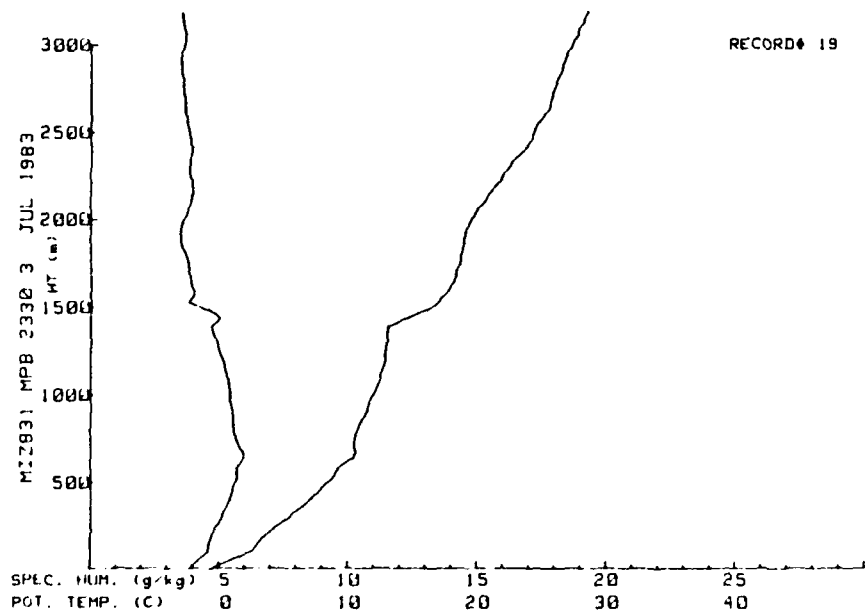
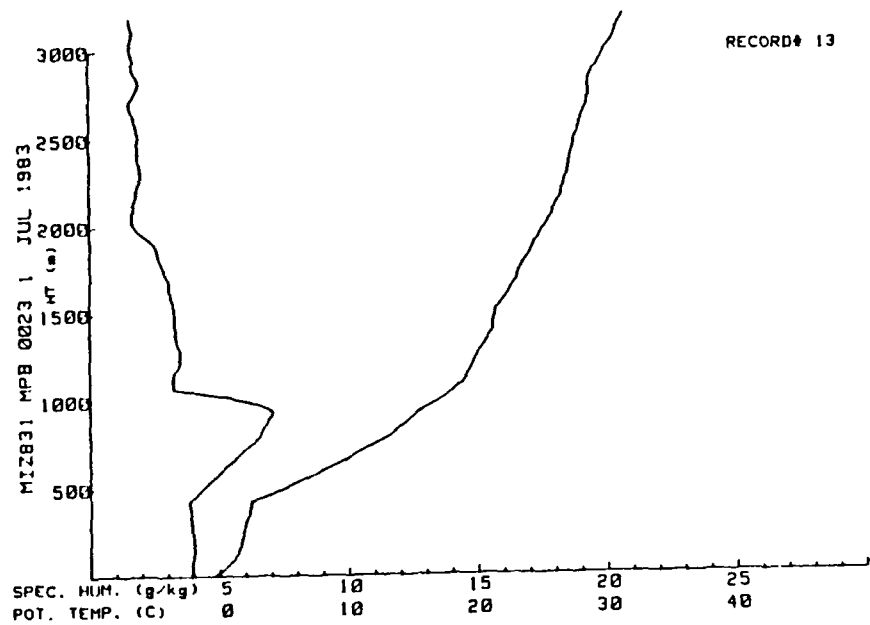


Figure 61. (a) T and T_d Plot from Radiosonde Sounding 1 July 1983, 0023 GMT. (b) T and T_d Plot from Radiosonde Sounding 3 July 1983, 2330 GMT.

sensors require time to dry out before accurate measurements can be made. Ice forming on the humidity element would remain on the element longer than water. Similar results were found by Hoehne (1984, unpublished manuscript) when a number of test soundings were made with both a VAISALA-RS80 and VIZ sonde attached to a single balloon. The variations of pressure and temperature measurements of the RS80 were comparable to those of the VIZ sonde. The dew-point depression variance, however, was 70% greater for the RS80 than that for VIZ. This was attributed to the inability of the RS80 sensor to recover after it passed through a saturated layer. This is evident in Fig. 61 where the level of the temperature inversion above the saturated mixed layer is different than that of the humidity jump. The physical explanation for such a warm, moist layer would be a maritime flow onto the ice above the boundary layer. On 3 July 2330 GMT the wind above 30 m is off-ice so the atmosphere should be relatively dry and cool at 300 m but the relative humidity remains at 100% while the temperature increases until 648 m. This inconsistency is likely due to humidity sensor wetting. The relative humidity decrease should start at the saturated layer top. Humidity sensor wetting, however, leads to the layer above the inversion being drier, in most cases, than indicated.

$$\ln \frac{e_s}{6.11} = \frac{M_v L_x}{R^*} \left(\frac{1}{273} - \frac{1}{T} \right)$$

where:

X = evaporation or sublimation.

The following latent heats of water substance may be assumed to be constant at 273°K (0°C).

$$L_{\text{evaporation}} = 597.3 \text{ cal/g}$$

$$L_{\text{sublimation}} = 677.0 \text{ cal/g}$$

$$L_{\text{melting}} = 79.7 \text{ cal/g}$$

The latent heat of the phase change, L_{12} , is defined as the quantity of heat that must be supplied to or taken from the substance even though the temperature remains constant (Hess, 1979).

Without moisture advection into the surface layer over the dense pack ice the specific humidity would be too low to allow for a humidity jump sufficient for ducting to occur. The large heat flux required to evaporate water or sublimate ice in the dense pack ice is significant when considering sources of moisture for the atmosphere.

E. RADIOSONDE HUMIDITY SENSOR WETTING

The reliability of standard American radiosonde humidity sensors has been addressed by Helvey (1982). He observed from dew-point temperature profiles that wetted humidity

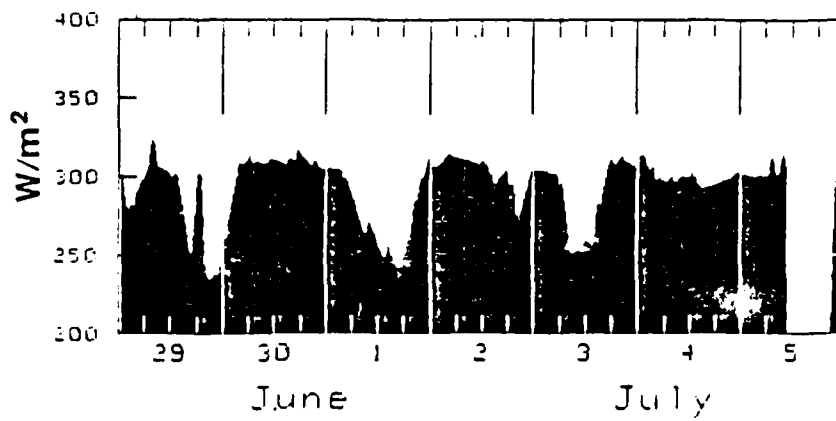
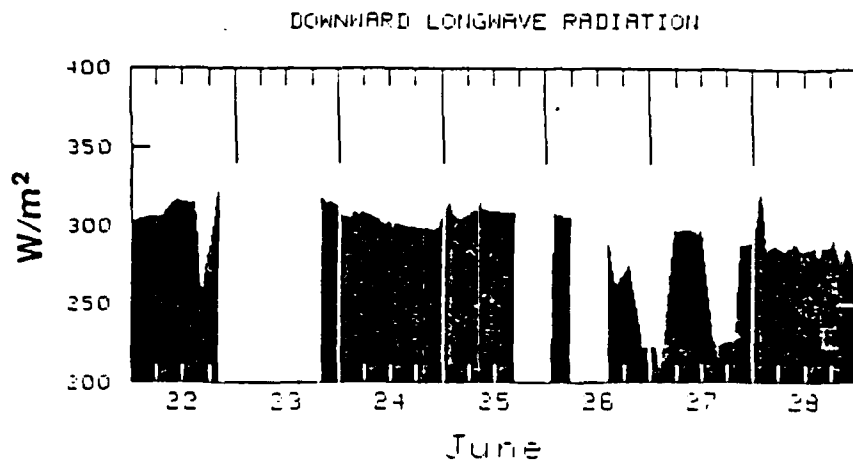


Figure 60. Downward Longwave Radiation Measured from R/V POLARBJORN During MIZEX-83

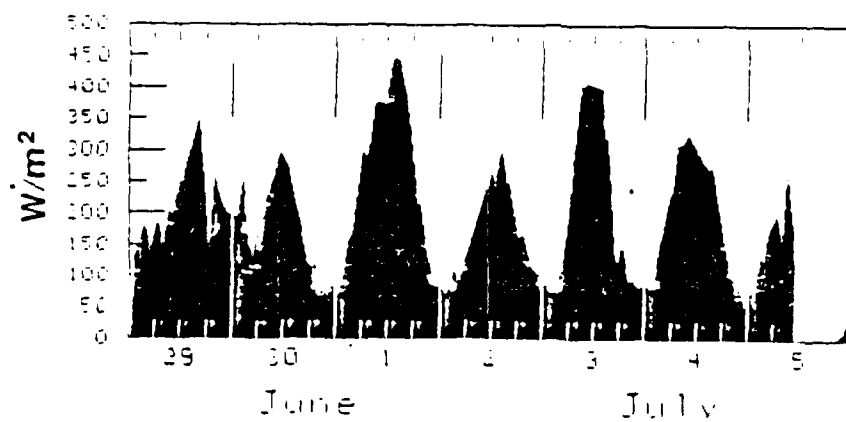
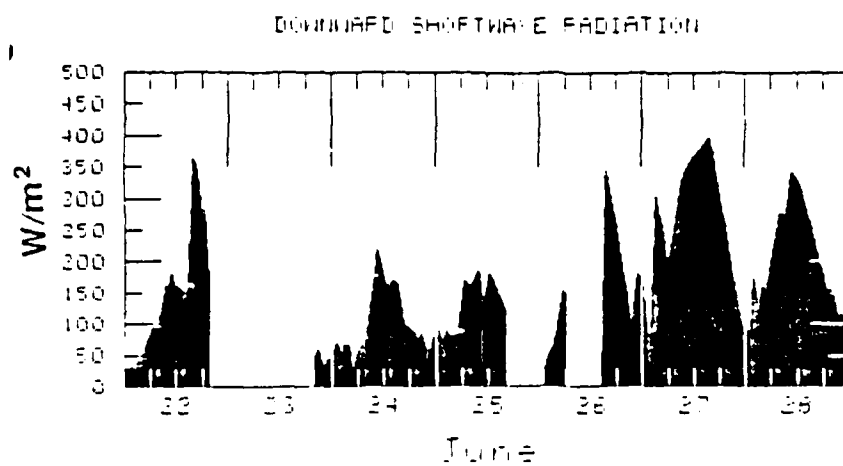


Figure 59. Downward Shortwave Radiation Measured from R/V POLARBJORN During MIZEX-83

Cumulus clouds result from convectively driven vertical motion. As demonstrated by Purves (1974) in the trade wind inversion case, cumuli penetrate the inversion layer. The inversion base is eroded and tends to elevate as the specific humidity and temperature humps decrease (ΔQ and ΔT).

D. MOISTURE CONTENT

A striking feature of the Arctic troposphere is the degree to which the atmospheric layer temperature determines the water vapor content of the layer. The importance of the surface temperature as a forcing mechanism has been stressed. Additionally, the importance of forcing from above due to subsidence and turbulent and radiative fluxes has been mentioned. Consideration of thermodynamic principles relative to observed mesoscale features in the MIZ is required.

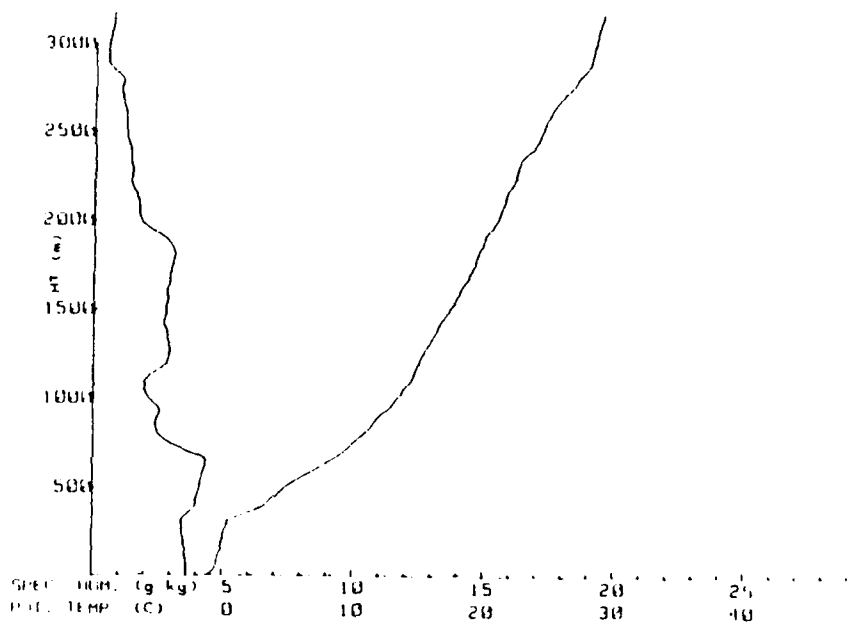
During the drift phase, observed positive vertical temperature gradients were relatively large compared to the vertical specific humidity gradients. The specific humidity of the MIZ atmosphere was typically about 4 g/kg at the surface and rarely exceeded 7 g/kg aloft. Surface (5 m) air temperature varied from -1°C to $+1^{\circ}\text{C}$ so that the cool surface layer did not hold much moisture.

For evaporation and sublimation the latent heats are assumed to be nearly constant (Hess, 1979) with $e_s = 6.11 \text{ mb}$ at $T = 273^{\circ}\text{K}$ we have:

bands allow discrimination between stratus and other cloud types. The horizontal extent of a uniform stratus deck indicates the spatial extent of the subsidence inversion.

Herman and Goody (1976) established that processes which destroy stratus clouds are generally limited to precipitation, absorption of solar radiation, evaporation by convective heating from the boundary layer, and synoptic activity. Because of minimal precipitation during MIZEX-83 and the absence of cyclones in the MIZ, primary stratus dissipation processes seem to have been absorption of solar radiation augmented by surface heating and evaporation by convective heating. Entrainment contributes to dissipation by increasing the temperature and decreasing the moisture within the mixed layer.

Stratus is most persistent over the dense pack ice where stable surface conditions prevail. The extent of radiation absorption by stratus clouds in the MIZ has not been determined. Measurements made during MIZEX-83 indicate that, although the sun never set, there were significant diurnal variations in solar radiation at the surface (Fig. 58). During clear periods, shortwave irradiance was as high as 485 W/m^2 at local noon and 120 W/m^2 at local midnight. Downward longwave irradiance at the surface was influenced by cloud cover. Longwave irradiance varied from approximately 50 W/m^2 on clear atmosphere days (Fig. 59) to a typical value of about 240 W/m^2 on cloudy days. Longwave irradiance was nearly constant during periods of fog at values averaging about 305 W/m^2 .



LOCATION: 79.02N 2.85E MIZEX83
 DATE TIME: 7 26 63 1937Z

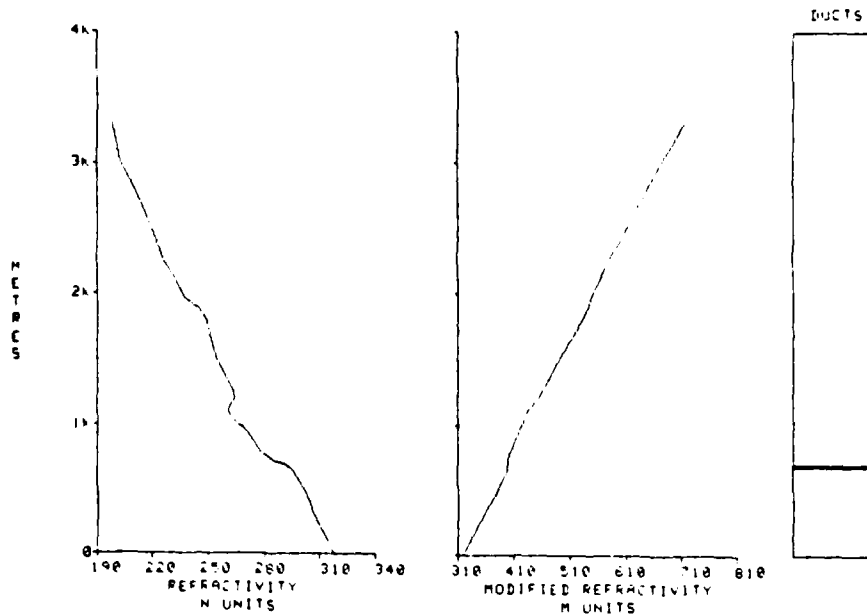
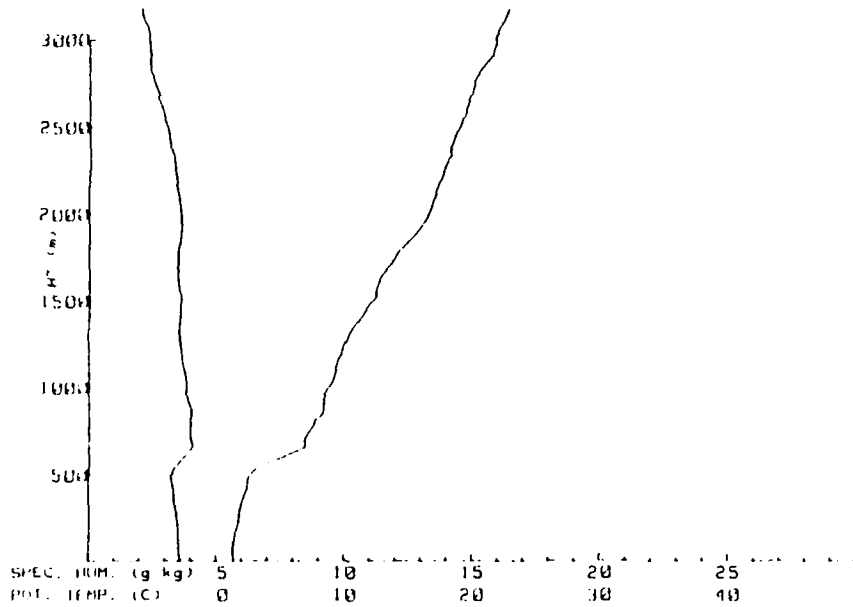


Figure 58. (a) Q and θ Plot for Radiosonde Sounding 26 July 1983, 1937 GMT. (b) IREPS Output for 26 July 1983, 1937 GMT.



LOCATION: 79.67N 2.98E
DATE TIME: 7 25 83 2332Z MIZE83

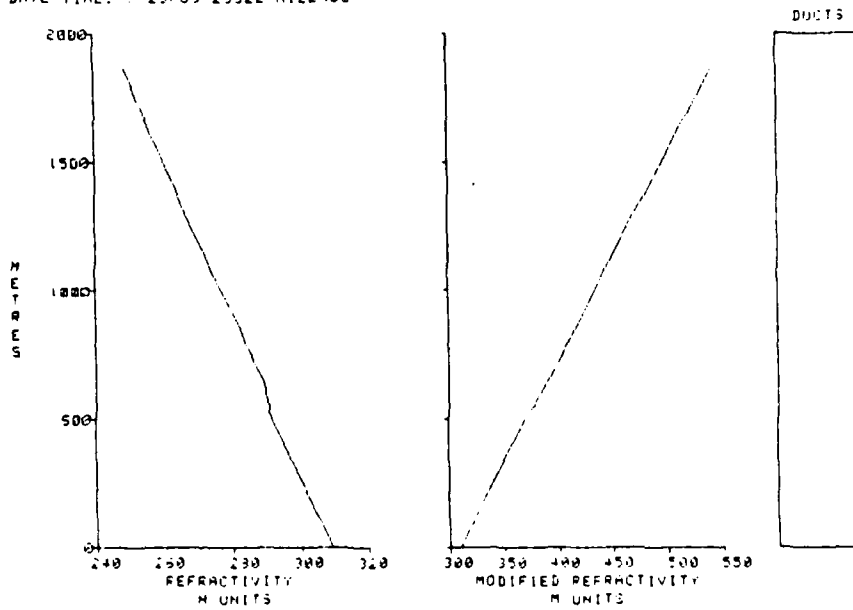


Figure 57. (a) Q and θ Plot for Radiosonde Sounding
25 July 1983, 2332 GMT. (b) IREPS Output
for 25 July 1983, 2332 GMT.

gradient which was large enough to overcome the slight specific humidity increase. A subrefractive layer was predicted from 1095 m to 1199 m where a moist layer existed; the specific humidity increased from 1.9 to 2.8 g/kg.

The multiple temperature inversions observed over the open pack ice regions of the MIZ could have been the result of turbulence. Cooling of the lower parts of the surface layer can be attributed to the lower temperatures of the open pack ice as compared to open water. The SST in the very open pack ice was 0.5°C as compared to 3.7°C in the open water. Cooling of the surface layer resulted in increased stability and an increase in the bulk Richardson number. The mesoscale variability in the MIZ is well represented by this example.

c. Importance of Cloud Types

During MIZEX-83 multiple layers of stratus were observed from POLARBJORN with the bottom layer identified as fog. Use of satellite imagery for the MIZ requires the interpretation of various cloud types and an understanding of the physical processes which produce and dissipate them. Interactive computer programs such as those used in SPADS (Satellite Prediction and Display System) allow inversion layer heights to be estimated from stratus cloud tops. Satellite visual and infrared imagery, when compared spatially and temporally, can be used to locate stratus clouds. Shadows cast by higher level clouds indicate relative cloud heights. Knowledge of the sensors' visual and infrared wavelength

due to a combination of wind shear instability and convection. Above the surface layer lapse rates were conditionally unstable or lightly stable.

One of the few examples of a well-mixed layer capped by a subsidence inversion is in a radiosonde sounding made on 25 July at 2332 GMT. POLARBJORN was in the open water at 79.67°N 2.98°E. The well-mixed layer extends up to 515 m where both the temperature and specific humidity increase (Fig. 57). Stratocumulus was observed and the surface wind was southwesterly at 6 m/s. In the surface layer the bulk Richardson number was .028. Refraction conditions were predicted to be normal up to 800 mb.

On 26 July at 1937 GMT the atmospheric boundary layer had become more neutral as shown in Fig. 58. The surface wind was southwesterly at 3 m/s. POLARBJORN's position was 79.02°N 2.65°E in the very open pack ice. The temperature and specific humidity jumps were significantly greater than the jumps observed in the previous sounding. The bulk Richardson number was -.009 in the surface layer. The lapse rate appears to have been nearly isothermal. Refraction conditions were predicted as super-refractive from 648 m to 773 m with the exception of a weak trapping layer ($\Delta M/\Delta z = -14.4 \text{ km}^{-1}$) from 689 m to 710 m. Although there was evidence of a warm moist layer above the stratus top at about 320 m the specific humidity probably did not decrease as fast as shown at 689 m. The entire layer from 648 m to 773 m was probably super-refractive because of the strong positive temperature

On 2 July at 1200 GMT when POLARBJORN was in the dense pack ice the bulk Richardson number was $+0.095$. The 2 July 1131 GMT sounding indicates a stable surface layer. The stable conditions exist up to the stratus top at about 2230 m. On 14 July at 2100 GMT the ship was in the open pack ice and the bulk Richardson number was -0.01 . The 2022 GMT sounding indicates that the surface layer was near-neutral and that convection above it was shallow. A stratocumulus layer occurred from about 570 m to 1430 m. Refraction conditions were predicted to be normal up to 700 mb. There was a detectable variability in the bulk Richardson number throughout the MIZ.

It is reasonable to conclude that for the case of a stable surface layer there was not enough surface flux induced mixing to cause significant entrainment aloft. The inversion bases which formed over the dense pack ice would have been dissipated primarily by radiative flux divergence and wind shear induced turbulence. Stratus dissipation and the importance of solar radiation diurnal variations will be stressed in subsection (C). Wind shear could have generated turbulence during 1-4 July when the surface wind speed varied from 1 to 5 m/s. However, it is difficult to substantiate this since additional research is required on mechanical turbulence induced entrainment.

Over the open pack ice the bulk Richardson number value indicated that the surface layer was near-neutral. The surface layer probably tended to become slightly unstable

synoptic-scale features and for cloud descriptions. Every effort should be made to correlate satellite passes with the vertical soundings. A climatology based on satellite pictures and IREPS output should be compiled so that a MIZ refraction effects model, similar to the Refraction Effects Guidebook (Helvey and Rosenthal, 1983), can be constructed.

3) Mesoscale variability in the MIZ is difficult to predict because of the many factors involved. In some areas turbulence may be stronger than the effect of subsidence so that inversion layers will weaken and lift. The strengths of the various processes which oppose atmospheric stability can be estimated by:

a. The air-sea temperature difference which is a rough estimate of the buoyant generation of TKE.

b. The surface roughness and local wind speed which are responsible for the mechanical generation of TKE.

c. The effect of solar and long wave radiation on stratiform clouds. The dissipation of stratus will weaken the ΔQ and ΔT at the inversion layer.

Further research is required in order to parameterize the mesoscale variability in the MIZ. The neutral drag coefficient C_{Dn} must be calculated for various surface characteristics. Accurate SST and air temperatures are a necessity. A better understanding of the radiative flux divergence at the top and bottom of various cloud types is required.

Until the regional forcing mechanisms are parameterized the atmospheric refraction conditions in the MIZ cannot be

accurately forecast. The operational implications are that the performance of many weapon and communications systems cannot be predicted accurately in the MIZ.

LIST OF REFERENCES

- Andreas, E.L., W.B. Tucker III and S.F. Ackley, 1984: Variation of the drag coefficient across the Antarctic marginal ice zone. MIZEX Bulletin, Part III, 63-71.
- Andreas, E.L., W.B. Tucker III and S.F. Ackley, 1984: Atmospheric boundary-layer modification, drag coefficient, and surface heat flux in the Antarctic marginal ice zone. J. of Geophys. Res., 89, 649-661.
- Arctic Pilot, 1975: prepared by the Hydrographer of the Navy, Volume 2, 7th edition, 48 pp.
- Belmont, A.D., 1958: Lower Tropospheric Inversions at Ice Island T-3, Polar Atmospheric Symposium, Pergamon Press, 215-284.
- Brown, R.A., 1981: Modeling the geostrophic drag coefficient for AIDJEX, J. of Geophys. Res., 86, 1989-1994.
- Brown, R.A. and W.T. Liu, 1982: An operational large scale marine PBL model, J. of Appl. Meteor., 21, 261-269.
- Brown, R.A., P. Taylor, S. Smith, K. Davidson, E. Andreas, G. Herman, K. Katsaras, and E. Augstein, 1984: Climate of the MIZEX region, MIZEX Meteorology 1984, unpublished manuscript, 40 pp.
- Helvey, R.A., 1982: Guidelines for correction of radiosonde-derived refractive profiles and climatologies. Pacific Missile Test Center Technical Publication TP000002, 8 pp.
- Helvey, R.A. and J.S. Rosenthal, 1983: Guide for inferring refractive conditions from synoptic parameters. Pacific Missile Test Center Technical Publication TP0000005, 36 pp.
- Herman, G. and R. Goody, 1976: Formation and persistence of summertime arctic stratus clouds. J. Atmos. Sci., 33, 1537-1553.
- Hess, S.L., 1979: Introduction to Theoretical Meteorology, Robert E. Krieger Publishing Company, 349 pp.
- Hoehne, W., 1984: Preliminary determination, operational comparability, VIZ/VAISALA. National Weather Service, paper presented at RCC/MG meeting, 3 pp.

- Johannessen, O.M., J.A. Johannessen, J. Morison, B.A. Farrelly, and E.A.S. Svendsen, 1983: Oceanographic conditions in the marginal ice zone north of Svalbard in early fall 1979 with an emphasis on mesoscale processes. J. of Geophys. Res., 88, 2755-2769.
- Kerr, D.E., 1951: Propagation of Short Radio Waves, McGraw-Hill Book Company, 728 pp.
- Macklin, S.A., 1983: Wind drag coefficient over first-year sea ice in the Bering Sea. J. of Geophys. Res., 88, 2845-2852.
- Mahrt, L. and S. Larsen, 1984: Oscillating nocturnal slope flow at a coastal valley in Greenland, submitted to Tellus, 14 pp.
- Overland, J.E., R.M. Reynolds and C.H. Pease, 1983: A model of the atmospheric boundary layer over the marginal ice zone. J. of Geophys. Res., 88, 2836-2840.
- Prik, Z.M., 1959: Mean position of surface pressure and temperature distribution in the Arctic. Tr. Arkticheskogo. Nauchn. - Issled. Inst. (in Russian), 266, 11-35.
- Pritchard, R.S., 1980: Sea ice processes and models: proceedings of the AIDJEX/ICSI symposium, 474 pp.
- Purves, C., 1974: Geophysical aspects of atmospheric refraction. Naval Research Laboratory Report 7725, 30 pp.
- Tsay, S. and K. Jayaweera, 1984: Physical characteristics of Arctic stratus clouds. J. Appl. Meteor., 23, 584-596.
- Tucker, W.B., III, 1984: Some simple concepts on wind forcing over the marginal ice zone, MIZEX Bulletin, Part III, 43-48.
- Vowinckel, E. and S. Orvig, 1970: The climate of the north polar basin. World Survey of Climatology, Vol. 14; Climates of the polar regions, S. Orvig. ed. Elsevier Publishing Co., Amsterdam, pp. 129-152.
- Wadhams, P. and V.A. Squire, 1983: An ice-water vortex at the edge of the East Greenland Current. J. of Geophys. Res., 88, 2770-2780.

INITIAL DISTRIBUTION LIST

	No. Copies
1. Defense Technical Information Center Cameron Station Alexandria, VA 22314	2
2. Library, Code 0142 Naval Postgraduate School Monterey, CA 93943	2
3. Professor Robert J. Renard, Code 63Rd Department of Meteorology Naval Postgraduate School Monterey, CA 93943	1
4. Professor Kenneth L. Davidson, Code 63Ds Department of Meteorology Naval Postgraduate School Monterey, CA 93943	5
5. Lieutenant James A. McNitt, USN Naval Oceanography Command Detachment Naval Air Station, Patuxent River MD 20670	3
6. Rear Admiral Robert W. McNitt, USN (Ret.) #90 Duke of Gloucester Street Annapolis, MD 21401	1
7. Captain Julian Wright, USN 2900 Cabin Creek Drive Burtonsville, MD 20866	1
8. Commander (Code 3253) Geophysics Branch: J. Rosenthal Pacific Missile Test Center Point Mugu, CA 93042	2
9. National Snow and Ice Data Center Attention: R. Armstrong CIRES/Campus Box 449 University of Colorado at Boulder Boulder, CO 80309	2
10. Commander Paul Gaffney, USN Naval Oceanography Command Facility P.O. Box 85 Naval Air Station Jacksonville, FL 32212	1

11. Mr. Robert M. Allan, Jr. 1
169 Del Mesa Carmel
Carmel, CA 93921
12. Dean Maynard M. Miller 1
College of Mines and Earth Resources
University of Idaho
Moscow, ID 83843
13. Dr. Barry Katz 1
Naval Surface Weapons Center
White Oak R42
MD 20910
14. Dr. C.W. Fairall 1
Department of Meteorology
Penn State University
University Park, PA 16802
15. Ronald W. Lindsay 1
Polar Science Center
4057 Roosevelt Way N.E.
Seattle, WA 98105
16. Professor Christopher N.K. Mooers, Code 68Mr 1
Naval Postgraduate School
Monterey, CA 93943
17. Commanding Officer 1
Naval Polar Oceanography Center
Navy Department
4301 Suitland Road
Washington, D.C. 20390
18. Dr. Will Shaw, Code 63Sr 1
Naval Postgraduate School
Monterey, CA 93943
19. Commander 1
Naval Oceanographic Office
NSTL Station
Bay St. Louis, MS 39522
20. Commanding Officer 1
Fleet Numerical Oceanography Center
Monterey, CA 93940
21. Commanding Officer 1
Naval Environmental Prediction
Research Facility
Monterey, CA 93940

22. Mr. Herb Hitney, Code 532 1
Naval Ocean Systems Center
San Diego, CA 92152
23. Commanding Officer 1
Naval Eastern Oceanography Center
McAdie Bldg (U-117)
Naval Air Station
Norfolk, VA 23511

END

FILMED

7-85

DTIC